



ScuDo
Scuola di Dottorato ~ Doctoral School
WHAT YOU ARE, TAKES YOU FAR

Doctoral Dissertation
Doctoral Program in Materials Science and Technology (XXX Cycle)

Designing for Additive Manufacturing

-

Product and Process Driven Design for Metals and Polymers

By

**Jukka Antero
Pakkanen**

Supervisor(s):

Prof. Paolo Fino
Prof. Matteo Pavese
Prof. Paolo Minetola
Dr. Diego Manfredi

Doctoral Examination Committee:

Prof. Matthew Gilbert, Referee, University of Sheffield, UK
Prof. Andrea Gatto, Referee, University of Modena and Emilia Romana, Italy

Politecnico di Torino
2018

Declaration

I hereby declare that, the contents and organization of this dissertation constitute my own original work and does not compromise in any way the rights of third parties, including those relating to the security of personal data.

Jukka Pakkanen

19.09.2018

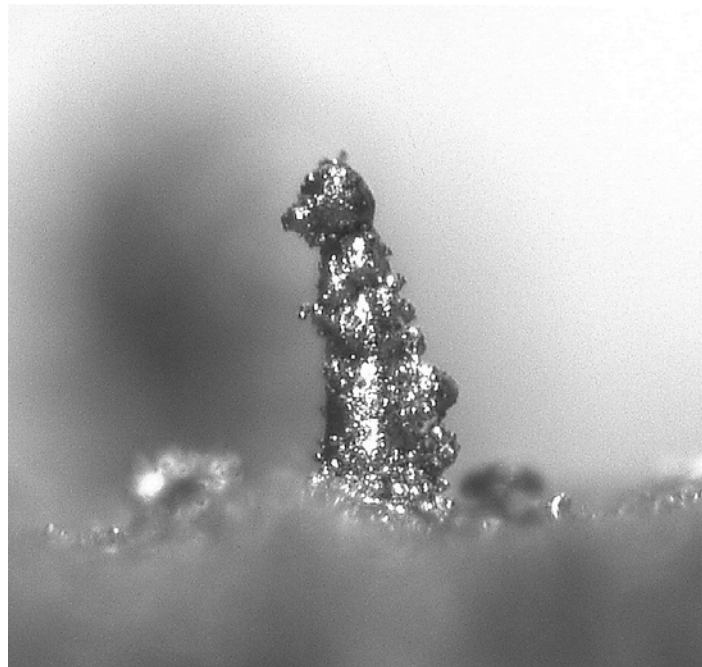
* This dissertation is presented in partial fulfillment of the requirements for **Ph.D. degree** in the Graduate School of Politecnico di Torino (ScuDo).

I would like to dedicate this thesis to the search for new and continuous technological advancements of humankind that will make lives better and safer for us and the future generations.

Acknowledgment

I would like to acknowledge all the people who have worked in collaboration with me for compiling the PhD thesis and the career leading to this point. Special thank you for the different universities that have hosted me and Politecnico di Torino for this ride. I would like to thank my team in Politecnico di Torino and the team leaders professor Paolo Fino, Dr. Diego Manfredi for guiding me in additive manufacturing. Also thanks to professors Luca Iuliano, Paolo Minetola and Matteo Pavese. Team members in AMMLab at Istituto Italiano di Tecnologia: Dr. Elisa Ambrosio, Dr. Flaviana Calignano, Dr. Massimo Lorusso, Dr. Riccardo Canali, Dr. Abdollah Saboori, Dr. Alberta Aversa, Francesco Trevisan, Giulio Marchese, Giulio Cattano, Simone Parizia and Aresh Mazdai. Additional thank you for the numerical simulation group in University of California San Diego with professor Alicia Hyunsun Kim. She and her group for providing a direction to topology optimization.

The last acknowledge is for my family and wife Dr. Anna Wołczyk, who shared the PhD ride with me until the end and helped me in the difficult times when the road is not so clear to make it until finish...



There are times when rough shapes take different forms in our imagination as this AlSi10Mg cylinder shows us. Thank you for everyone who was left unmentioned. You are the unknown heroes.

Abstract

Additive Manufacturing (AM) has broken through to common awareness and to wider industrial utilization in the past decade. The advance of this young technology is still rapid. In spoken language additive manufacturing is referred as 3D printing for plastic material and additive manufacturing is left as an umbrella term for other materials i.e. metallic materials and ceramics. As the utilization of AM becomes more widespread, the design for additive manufacturing becomes more crucial as well as its standardization.

Additive manufacturing provides new set of rules with different design freedom in comparison with subtractive manufacturing methods. This is thought to empower product driven designs. However, in the AM methods there are process driven variables that limit the designs functions to what could be manufactured. There are often extra steps after production to finalize the design. Topology optimization utilizes product driven design where material is only where it is needed to be. The design is computed without taking into account any manufacturing constraints and only the design in the final application stage is achieved. Topology optimization algorithm is explored in detail for two algorithms. Then these algorithms are compared in case study I to gain better understanding of the algorithms functions. Case study I consists of 2D and 3D algorithms where a 3D level set method algorithm was written for this purpose.

The concept of designing for additive manufacturing is examined for polymeric materials in case study II with a help of topology optimization design software tailored for additive manufacturing market. The parts are manufactured with different AM methods, examined and results are explained. The results show an interesting effect of anisotropy and the manufacture methods effect in the part mechanical properties.

On the other hand, process driven design and its concepts important as the manufacturing method dictates, what can and should be done economically. Metal AM process constraints are explored in case study III through accuracy studies in metal additive manufacturing at laser powder bed fusion (LPBF) technology. Accuracy and surface studies are concluded to gain a better understanding of the process and manufacturability of metal parts. The gain knowledge is explained and examples are shown how these are utilized to make metal parts with tailored properties and with minimal post processing needs.

Contents

Declaration.....	I
Acknowledgment.....	III
Abstract.....	IV
Contents	V
List of Publications	VII
List of Figures.....	VIII
List of Tables	XIV
List of Equations.....	XV
Abbreviations.....	XVI
1. Introduction	1
2. Literature Review	3
2.1. History of Additive Manufacturing	4
2.2. Standardization of Additive Manufacturing	5
2.2.1. Terminology	7
2.2.2. AM Methods.....	10
2.2.3. List of Published AM Standards.....	13
2.2.4. Outlook	14
2.3. Manufacturing Methods Used Experimentally.....	15
2.3.1. Material Extrusion	15
2.3.2. Selective Laser Sintering	20
2.3.3. Laser Powder Bed Fusion (LPBF)	22
2.3.4. Post Processing in AM	29
2.4. Product Driven Design.....	30
2.4.1. Topology Optimization	30
2.4.2. Solid Isotropic Material with Penalization (SIMP)	31
2.4.3. Level Set Method	37

2.4.4.	Other Topology Optimization Algorithms	40
2.4.5.	Commercial Software	40
2.4.6.	Using Topology Optimization	41
2.5.	Process Driven Design	43
2.5.1.	Polymeric Materials	43
2.5.2.	Metallic Materials	49
3.	Case Studies	53
3.1.	Case Study I: Product driven design	53
3.1.1.	2D Comparison: SIMP and LSM Algorithms	53
3.1.2.	3D Comparison: SIMP and LSM Algorithms	55
3.1.3.	Summary	59
3.2.	Case Study II: Application of Product Design	60
3.2.1.	Topology optimization and design	60
3.2.2.	Manufacture and Testing	64
3.2.3.	Selective Laser Sintered Material	66
3.2.4.	Material Extrusion Material	74
3.2.5.	Summary	80
3.3.	Case Study III: Metal Application of Process Design	81
3.3.1.	Manufacture Equipment	81
3.3.2.	Design of holes	83
3.3.3.	Design of tubes	91
3.3.4.	Design of Hydraulic Components	99
3.3.5.	Summary	105
4.	Conclusions	107
5.	Recommendations for Future Work	110
	References	112
	Appendix I – Finite Element Analysis	123
	Appendix II – LSM 3D Code	127

List of Publications

2015

C. Semini, J. Goldsmith, D. Manfredi, F. Calignano, E.P. Ambrosio, **J. Pakkanen**, D.G. Caldwell. “*Additive manufacturing for agile legged robots with hydraulic actuation*”, Advanced Robotics (ICAR), (2015)

2016

J. Pakkanen, R. Vallant, M. Kičin. “*Experimental investigation and numerical simulation of resistance spot welding for residual stress evaluation of DP1000 steel*”, Welding in the World, Vol. 60, Iss. 3, pp 393-402, (2016)

J. Pakkanen, F. Calignano, F. Trevisan, M. Lorusso, E.P. Ambrosio, D. Manfredi, P. Fino. “*Study of Internal Channel Surface Roughness Manufactured by Selective Laser Melting in Aluminum and Titanium Alloys*”, Metallurgical and Materials Transactions A, Vol 47, Iss. 8, pp. 3837–3844 , (2016)

2017

F. Calignano, M. Lorusso, **J. Pakkanen**, F. Trevisan, E. P. Ambrosio, D. Manfredi, P. Fino. “*Investigation of accuracy and dimensional limits of part produced in aluminum alloy by selective laser melting*”, The International Journal of Advanced Manufacturing Technology, Vol 88, Num 1 – 4, pp. 451–458, (2017)

F. Trevisan, F. Calignano, M. Lorusso, **J. Pakkanen**, A. Aversa, E.P. Ambrosio, M. Lombardi, P. Fino, D. Manfredi. “*On the Selective Laser Melting (SLM) of the AlSi10Mg Alloy: Process, Microstructure, and Mechanical Properties*”, Materials, 10, 76, (2017)

J. Pakkanen, D. Manfredi, P. Minetola, L. Iuliano. “*About the Use of Recycled or Biodegradable Filaments for Sustainability of 3D Printing. State of the Art and Research Opportunities*”, Smart Innovation, Systems and Technologies, Vol. 68, pp. 776 – 785, (2017)

List of Figures

Figure 1. Structure of AM Standards [8].....	6
Figure 2. Binder jetting	10
Figure 3. Direct energy depositing process in wire or powder base method. .	11
Figure 4. Material jetting process.....	11
Figure 5. Sheet lamination process.	12
Figure 6. Vat photopolymerization process.	12
Figure 7. Roadmap for Standardization. SASAM [8].....	15
Figure 8. Schematic of material extrusion.	16
Figure 9. Porosity between extrusion layers [20].....	17
Figure 10. Tensile strength and elongation of fabricated parts with material extrusion.....	18
Figure 11. Laser sintering process. [38].....	21
Figure 12. Laser Powder Bed Fusion [39]	22
Figure 13. Gas atomized powder [42].....	24
Figure 14. Water atomized powder [42]	24
Figure 15. Spheroidized powder [42].....	25
Figure 16. Direction of the scan.	25
Figure 17. Scanning strategies: a) and b) linear and parallel, c) perpendicular and d) alternative scanning	26
Figure 18. Stripe pattern.....	26
Figure 19. Checkerboard pattern.....	27
Figure 20. Island pattern in scanning strategy.....	27
Figure 21. Scanning strategy shift of 67-degrees in EOS M AM-machines depending on the layer.	28
Figure 22. Different angles what laser has with on 67-degree angle rotation before the pattern repeats.	28
Figure 23. Topology optimization algorithm.	31
Figure 24. Generalized shape design problem in two-dimensional space for finding optimal material distribution.	32

Figure 25. Compliance problem in SIMP interpolation.....	35
Figure 26. Checkerboard problem visualized, a) the design space, b) checkerboard [44]	37
Figure 27. Effect of mesh refinement into design [44]	37
Figure 28. Representation of a level set curve.	38
Figure 29. Topology optimized and milled Brembo GP4 RX brake caliper. [59].....	42
Figure 30. Brake disk of a bicycle. Left Shimano commercial disk and right simulated result from Altair OptiStruct [60].....	42
Figure 31. 3D model simplified into layered structure.	46
Figure 32. Layers effect by staircases on surface roughness [71].....	52
Figure 33. Cantilever, a constrained beam from one side and a weight on the other side.....	54
Figure 34. 150x50 mesh cantilever optimized: left Matlab SIMP [78] algorithm, right Matlab LSM [79] algorithm.....	55
Figure 35. Cantilever in 3D model.....	56
Figure 36. 15x15x15 mesh cantilever optimized with Matlab: left 3D SIMP and right 3D LSM.	56
Figure 37. CAD model printed out from small 3D cantilever simulation: left 3D SIMP and right 3D LSM.....	57
Figure 38. SIMP 3D convergence of 60x30x30 mesh	57
Figure 39. CAD model printed out from large 3D cantilever simulation: left 3D SIMP and right 3D LSM.....	58
Figure 40. 3D printed model of 3D LSM output.....	58
Figure 41. Altair Hyperworks Inspire simulation with the large cantilever 60x30x30 problem. Different design constrictions: free, symmetry, extrusion. ...	59
Figure 42. Flexural three-point bend specimen design: a) schematic of the design, b) design in Inspire 2016. Red: design space, silver: non-design space to equally distribute the load, round cylinders: support and force cylinder.....	62
Figure 43. Topology optimized result EOS PEEK.	62
Figure 44. Topology optimization result with ABS Plus P430 at strength of 52 MPa (Model 01) and 32 MPa (Model 02). The a parameter set has pressure load of 5MPa with 1.2 factor of safety and b parameter set has pressure load of 4 MPa with 1.5 factor of safety.	63
Figure 45. Stratasys Dimension Elite material extrusion machine.	64

Figure 46. EOS P800 laser sintering machine.....	64
Figure 47. Manufacturing directions for EOS peek (left) and ABS (right)	65
Figure 48. Three-point bending test machine.....	66
Figure 49. Left: Safety factor. Right: tension (orange) and compression (green) areas in the model EOS PEEK.	66
Figure 50. Pressure test results for PEEK sample X-, Y- and Z-direction. Design force 1000 N, break point 1200 N.	67
Figure 51. Pressure test results for PEEK sample X-direction. Design force 1000 N, break point 1200 N.....	68
Figure 52. Pressure test results for PEEK sample Y-direction. Design force 1000 N, break point 1200 N.....	68
Figure 53. Pressure test results for PEEK sample Z-direction. Design force 1000 N, break point 1200 N.....	68
Figure 54. Broken specimen build in showing break pattern.....	69
Figure 55. Material sample from pressure test specimen.....	69
Figure 56. One phase breaking pattern when the whole structure fails at same time: a) specimen without load, b) specimen at max load, c) specimen failure. ...	69
Figure 57. Two-phase breaking pattern. Bend test of EOS PEEK sample manufactured in Z-direction (E_Z_1): a) Specimen without pressure, b) specimen under load, c) specimen cracked under load on top left corner, d) crack propagation under load and new crack under the pressing tool, e,f) failure of the specimen	70
Figure 58. Material slice according to build direction.	71
Figure 59. Material in direction 1, top X-direction, middle Y-direction, bottom Z-direction.	72
Figure 60. Material in direction 2, top X-direction, middle Y-direction, bottom Z-direction.	72
Figure 61. Fracture surface along Z-direction PEEK specimen.....	73
Figure 62. Vickers micro hardness (HV0.1) of the PEEK slices with 100g weight.....	74
Figure 63. Average hardness measurement with Berkovich nano hardness tip.	74
Figure 64. Hardness profile of X-direction alongside of Z-axis with hardness measurement with Berkovich nano hardness tip.	74

Figure 65. Safety factor between high stressed model 01 and low stressed model 02.	75
Figure 66. Tension and compression maps between high stressed model 01 and low stressed model 02.	76
Figure 67. Model 01b, 3 point pressure test with x-, y- and z-directions. Design force 1000 N, breakpoint 1200 N.	76
Figure 68. ABS Y-direction breaking: a) before pressing, b) ultimate pressing force, c) yield of the strut pointed by the arrow and the cutting of the strut, d) failure of the strut made the piece fail also on the lower side corner.	77
Figure 69. ABS X-direction breaking: a) before pressing, b) strut on the left side and behind gives away, c) second left struts gives away.	78
Figure 70. ABS Z-direction breaking: a) before pressing, b) breakpoint, a crack has formed below of the presser firstly and then to the left bottom of a strut.	78
Figure 71. ABS Plus P430 X-direction bend test.	79
Figure 72. ABS Plus P430, Y-direction bend test.	79
Figure 73. ABS Plus P430, Z-direction bend test.	79
Figure 74. Cross section of failed ABS parts: a) x-direction, b) z-direction...80	
Figure 75. AM-machine: EOS EOSINT M270.	82
Figure 76. British hexagonal 50 pence coin with a constant radius.	84
Figure 77. STL-approximation of a round object.	86
Figure 78. Circles mentioned in [96] standard. a) Minimum zone reference circle, b) least squares reference circle, c) minimum circumscribed reference circle and d) maximum inscribed reference circle. Figure from [98]	87
Figure 79. Accuracy hole sample a) vertical and b) horizontal	87
Figure 80. Comparison of LOM and stereo microscope in making a mask of the hole. 1a) LOM 5x image of 1mm diameter hole and 1b) its hole mask. 2a) stereomicroscope 8x image of the same hole and 2b) its mask.	88
Figure 81. Hole roundness values in comparison to the hole diameter values. Black: horizontal hole and grey: vertical hole.	89
Figure 82. 1 mm diameter hole from horizontal build (left) and vertical build (right)	90
Figure 83. 4 mm diameter hole from horizontal build (left) and vertical build (right)	90

Figure 84. A hollow cylinder fabricated with different building angles to test the change in internal surface roughness.	91
Figure 85. Manufactured hydraulic component shapes from AlSi10Mg and Ti6Al4V.	91
Figure 86. Manufactured hydraulic component shapes from AlSi10Mg and Ti6Al4V at 0-angle.	91
Figure 87. Tubes manufactured from AlSi10Mg in different angles.	92
Figure 88. Unsupported bend in dimension reduction part of a piece leading to sagging effect on the piece.	93
Figure 89. FESEM image of the internal surfaces of the cylindrical shapes produced by SLM with different angles: a) 0 angle top, b) 0 angle bottom, c) 45 angle top, d) 45 angle bottom, e) 60 angle top and d) 60 angle bottom surface.	95
Figure 90. Dark stylus tracks representing the surface roughness tester indentation on internal surfaces: a) 0° angle bottom and b) 45° angle bottom surface with not optimal stylus path.	96
Figure 91. Roughness measurements on AlSi10Mg and Ti6Al4V internal surfaces	97
Figure 92. Difference in cross-section roughness between a) bright field and b) dark field images. Dark field shows the surface structure below the cross section.	98
Figure 93. Comparison of measured Rmax and cross-section peak to bottom measurements.	98
Figure 94. The two S-shaped aluminum manifolds made by Direct Metal Laser Sintering (DMLS): just after shot-peening (on the left), and after testing with pressurized oil (on the right).	100
Figure 95. Internal channel of the manifold (left: as build, right: tested with oil) and the stereomicroscopically examined spots: 1. Fixing cavity, 2. Inside channel and 3. Curve.	101
Figure 96. Inside cavity reachable with shot peening and machined with threads.	101
Figure 97. Inside channel of the manifolds: after shot peening (on the left) and tested with oil (on the right).	102
Figure 98. Corner of the manifolds: after shot peening (on the left) and tested with oil (on the right).	102
Figure 99. CAD model of HyQ2Max with close-up views of the highly-integrated hydraulic manifolds of the two hind legs. [100]	103

Figure 100. CAD models of hydraulic manifolds for the legs of the HyQ2Max robot. Left: traditionally manufactured manifold (green parts). Right: highly integrated AM manifold. [100].....	103
Figure 101. Orientation of hydraulic block a) 45-degree slope, b) 5-degree tilt for recoating blade angle, c) hydraulic block with support structures in Magics 18 and d) the final part.	104
Figure 102. The hydraulic manifold a) after shot peened and b) during pressure testing.	105
Figure 103. Stiffness matrix element	123
Figure 104. Two stiffness elements.....	124

List of Tables

Table 1. Common material extrusion materials	17
Table 2. LS Materials available.....	22
Table 3. Process variables during LPBF manufacturing.....	23
Table 4. Design rules for polymeric 3D printing materials [63].....	47
Table 5. Material properties used in simulation.....	63
Table 6. Material composition EOS AlSi10Mg Wt. % [92]	82
Table 7. Material composition EOS Ti64 Wt. % [93]	82
Table 8. EOSINT M270 fabrication parameters.	83
Table 9. Shape describing quantities and descriptions listed by Rodriguez et al. in [97].....	85
Table 10. Roughness measurements from samples (μm).....	96

List of Equations

Equation 1. Internal virtual work of an elastic body at equilibrium u for virtual displacement v .	32
Equation 2. Minimum compliance for global stiffness problem.	33
Equation 3. FE approximation of the optimization problem.	33
Equation 4. Optimization problem in global form	33
Equation 5. Stiffness tensor with distributed material.	34
Equation 6. SIMP function.	34
Equation 7. Penalization factor equations.	34
Equation 8. Lagrangian equation from the SIMP compliance problem.	35
Equation 9. Stiffness and density design update equations.	36
Equation 10. strain energy for intermediate densities at iteration K .	36
Equation 11. Level set function equation.	38
Equation 12. The mean curvature of the LSF interface.	39
Equation 13. Signed distance function.	39
Equation 14. General LSM optimization problem statement.	39
Equation 15. Level set method optimization problem.	40
Equation 16. Elemental stiffness matrix force equilibrium equations.	123
Equation 17. Elemental stiffness matrix force equilibrium equations in matrix form.	123
Equation 18. Global stiffness matrix force equilibrium equations.	124
Equation 19. Elemental stiffness matrix force equilibrium equations in matrix form.	124
Equation 20. Elemental stiffness matrix force equilibrium equations showing the conjunction of the matrixes.	124

Abbreviations

AM	Additive Manufacturing
ASTM	American Society for Testing and Materials
ISO	International Organization for Standardization
SASAM	Support Action for Standardization in Additive Manufacturing
SLA	Stereolithography Apparatus
SLS	Selective Laser Sintering
DMLS	Direct Metal Laser Sintering
SLM	Selective Laser Melting
LPBF	Laser Powder Bed Fusion
CMB	Controlled Metal Build-up
DMD	Direct Metal Depositing
CNC	Computer Numerically Controlled
FFF	Fused Filament Fabrication
EBM	Electron Beam Melting
EBPBF	Electron Beam Powder Bed Fusion
LEAP-engine	Leading Edge Aviation Propulsion Engine
RP	Rapid Prototyping
OEM	Original Equipment Manufacturer
FE	Finite Element

FEM	Finite Element Method
FEA	Finite Element Analysis
DOF	Degree of Freedom
LSM	Level Set Method
LSF	Level Set Function
FESEM	Field-Emission Scanning Electron Microscope
SEM	Scanning Electron Microscope
AFNOR	French committee for Standardization
UNM 920	French technical body for AM standardization
VDI	German committee for Standardization
GPL	Committee on Production and logistics from Germany
AENOR	Spanish committee for Standardization
AEN/CTN 116	Spanish technical body for AM standardization
SIS	Swedish committee for Standardization
SIS/TK 563	Swedish technical body for AM standardization
BSI	British committee for Standardization
AMT/8	British technical body for AM standardization
CEN	European Committee for Standardization
CENELEC	European Committee for Electrotechnical Standardization
ESO	Evolutionary Structural Optimization
BESO	Bi-directional Evolutionary Structural Optimization
ECP	Electrochemical Polishing
ISS	International Space Station

MZCI	Minimum Zone Reference Circle
LSCI	Least Squares Reference Circle
MCCI	Minimum Circumscribed Reference Circle
MICI	Maximum Inscribed Reference Circle
LOM	Light Optical Microscope
ABS	Acrylonitrile Butadiene Styrene
PEEK	Polyether Ether Ketone
SIMP	Solid Isotropy Material with Penalization
IM	Injection Moulding
HAZ	Heat Affected Zone

Chapter 1

1. Introduction

A computer aided design (CAD) is manufactured by a machine into an object. It is called Additive Manufacturing (AM). Why is it called additive manufacturing and not 3D printing? Additive manufacturing is old name for the process that has been used in the industrial applications since the dawn of the technology. A layer on another layer is added “additively” and then it is repeated countless of times. This was also referred as rapid prototyping (RP) as it was the first successful application of AM. To simplify the process for consumers and users the process has been called many names as solid photography in the 1970’s and lately 3D printing. It is easier to imagine developing a film in 3D or printing a 3D object than additive manufacturing. Therefore 3D printing has stuck to the public. It is defined in ASTM standard to be polymeric layer manufacturing when additive manufacturing is defined for other materials printing, like metals and ceramics, and for industrial applications.

This is a PhD thesis consists of topics in additive manufacturing (AM) and design topics related to designing for the additive manufacturing. Additive manufacturing is manufacture method where instead of subtracting material, the material is added to create the shape. The scope of the thesis is to give overview about the latest developments in AM and insights into product and process driven design. This is done by dividing the thesis into five section.

Firstly the relevant literature to understand the process and design methods is provided in Chapter 2: Literature Review. AM methods are described from technical and historical point of view. Additionally an insight to the future trends of the technology and standardization is presented. Design point of view is provided through deep dive into topology optimization (topopt) and its possibilities for AM. Additionally AM process constraints are provided in

polymeric and metallic materials, what are utilized in designing for AM. Therefore, giving the product and process driven design overviews for AM.

Followed by is Chapter 3: Case Studies, where the main findings throughout the PhD career is gathered. In Product driven design the case study includes comparison of two different topology optimization codes through 2D and 3D topology optimization codes. Simple topt codes are important as these provide overview of the optimization process into more complex cases. Powerful commercial software is then used to optimize and simulate parts for correct material properties before manufacturing with polymer AM processes. Case studies second half consists from metal AM and provides solutions for challenges in metal manufacturing with laser powder bed fusion (LPBF) equipment. Study of AM manufacture from simple holes providing accuracy for the process is extended to tubes and the knowledge is used in practical application of AM hydraulic manifold.

The Chapter 4: Conclusions will summarize the overall findings and the last Chapter 5: Recommendations for Future Work will provide future outlook for research directions.

Chapter 2

2. Literature Review

Design is an important part of manufacture. Design has been thought through functionality as well as the aesthetic aspects of the final product. In mechanical pieces the functionality is the most important when in a high-end item like jewelry the beauty outweighs other functions. Therefore, it is necessary to look the design from multiple angles.

It is possible to consider *what can be designed* without considering manufacturing constraints. This is product driven design and it is often seen in high end luxury products where the amount of resources is not spared when achieving the goal. On the other hand, economic constraints often forces the designers to choose the best manufacturing method for a product by the scale of *what can be manufactured*. When manufacturing constraints are taken into account the design becomes a process driven and designed to the specific manufacturing process. For example, an I-beam can be manufactured with different manufacturing methods (i.e. forging, extrusion, welding, machining) and the same shape is gain. However, the road to the shape is not the same and the resources spend are not equal.

Additive manufacturing has been called a revolution in design because it offers a new way of thinking the fabrication of a part. Instead of subtracting material, it is possible to add material. When building a difficult shape is time consuming to machine from a large volume, AM offers the possibility of just building the shapes and nothing more leading to material saving as there is less metal scrap from subtracting the material. The customer is not paying premium for the extra removed material that ends in recycling, but just for the used material. Another economical aspect in additive manufacturing is that adding

material takes time as well as subtracting material. Hence, adding less material or making more difficult shapes that reduce the final build volume saves build time and material needed leading to cheaper costs. This is usually referred with marketing slogan “in additive manufacturing complexity is for free.”

2.1. History of Additive Manufacturing

The inventions of additive manufacturing have been a long process. First key components for AM, photo resins, were invented in 1950's by DuPont. Laser technology came along with first experiments of curing photo resin in 1960's by Battelle Memorial Institute. In 1970's Dynell Electronics Corporation called their technology as solid photography. A name that helped the public to visualize the process in a similar way as 3D printing is used currently. [1]

Stereo lithography can be claimed to have emerged in 1980 when Japanese Hideo Kodama in Nagoya Municipal Research Institute researched and published his work in paper “*Automatic method for fabricating a three-dimensional plastic model with photo-hardening polymer*” [2]. He published three papers in the field of additive by 1982. However, he didn't have financial means to continue and patent his research. In the same period researchers in USA and Europe were working in the same field achieving their first publications in 1984. [1]

A commercial success was achieved in 1987 with stereo lithography apparatus (SLA) that was commercialized SLA-1 by 3D Systems. Other technologies followed as selective laser sintering (SLS) in 1992 by DTM company (now part of 3D systems). In 1994 Electro Optical Systems (EOS) developed direct metal laser sintering (DMLS) platform called EOSINT. [1]

A photo curable resin was the first material to be used in additive manufacturing and more followed in 1980's and 1990's. In 1999, Fraunhofer collaborated separately with Fockele and Schwarze to make steel powder based selective laser melting (SLM) with steel powders and with Röders in controlled metal build up (CMB) technology. Also in 1999, the first colour plastic 3D printer was revealed. [1]

In the year 2000, direct metal deposition (DMD) as blown powder method was invented. It took an advance of diode laser technology and the fact that diode laser wavelength can be bend into an optical fibre and the power of laser transferred more precisely than with conventional CO₂ lasers. Diode lasers replaced the CO₂ lasers at a fast pace in new machines. In 2001 Concept Laser released hybrid additive manufacturing machine with SLS and computer numerically controlled (CNC) cutting in one. [1]

In 2005, an open source RepRap-project (replicating rapid prototyper) was started in University of Bath by Dr Adrian Bowyer. He created an open source project to have self-replicating and evolving machine for everybody learn and copy from. In addition to that software solutions were developed in open source to

accommodate RepRap hardware. The technology uses a tubular filament that is heated by extrusion nozzle and it was called Fused Filament Fabrication (FFF). Thereafter a name 3D printing was created. The project was soon copied and utilized in maker communities due to its open nature. It brought additive manufacturing technology to the customers with cheap and affordable equipment. [3]

Electron beam melting (EBM) became available to public in 2006 when Arcam released the first commercial machine with electron beam as energy source. However the history of the method is longer as the first patent regarding to 3D models made by electric current came in 1993 [4] from Sweden. This eventually lead the initial research evolving into a company Arcam. Arcams industrial pilot phase was in 2002 when its first clients received their first machines. [5]

In 2008, Shapeways brought an additive manufacturing printing service platform to the public. One can upload one's own design to service and order it to be printed or can buy ready-made design products. In 2009, ASTM International created committee F42 to address issues of expanding the market and lack of standards in the additive manufacturing field. Soon they released standards to unify naming, a standard for new file format '*.AMF' for the future to replace old '*.STL' file format. In elsewhere, Microsoft, HP, Dassault systems and some minor companies went with '3MF' file format to replace 'STL' files. A joint collaboration across the countries was made for AM-standardization as America and Europe didn't want to have different standards. ASTM works with ISO and European standardization bodies to unify and not make competing standards. [1]

Latest developments are the AM moving to cloud-based services, where it's possible to make CAD model; prepare and slice it for printing; send it to a printer. The standardization has brought dental products and aerospace products to the printers. GE has created leading edge aviation propulsion (LEAP) engine that has 19 AM nozzle parts made from Inconel. The nozzle is designed to replace a twenty-part assembly and give weight savings. AM parts are moving from non-structural class in aviation to structural class with the development of process and quality verification. Fabrication laboratories for home makers have got popular with fabrication cafes where one can have a coffee and can fabricate one's own design while waiting. The limits of additive come closer to the people, since the key patents are expiring.

2.2. Standardization of Additive Manufacturing

For wider adaptation of AM and 3D printing in the economy, standardization is a key component that has to be fulfilled. The standardization efforts were started in the USA by American Society for Testing and Materials (ASTM) with ASTM's

F42 committee on additive manufacturing in 2009 [6]. A few years afterward in 2011, in Switzerland the International Organization for Standardization (ISO) founded committee ISO/TC 261 on additive manufacturing [7]. In fear of two different global standards the community created collaboration between Europe and USA with the European Union funded project. The funding came through international collaboration and from EU's framework project 7 (FP7). Therefore from September 2012 a joint project on Standardization of Additive Manufacturing roadmap SASAM [8] was born. The joint collaboration aimed to create uniform standards between ISO and ASTM avoiding confusion and extra work, hence, benefitting all parties.

Standardization of AM has gone forward from 2012 under the same umbrella. Up to date in July 2017, ISO has released 6 standards in general principles and 10 more standards are under development. Whereas ASTM has released 15 standards in: design, materials and processes, terminology and test methods, and is developing more. A full List of Published AM Standards published up to July 2017 is included in this chapter. Standardization roadmap of Figure 1 from 2013 gives away the direction where the standardization efforts are going.

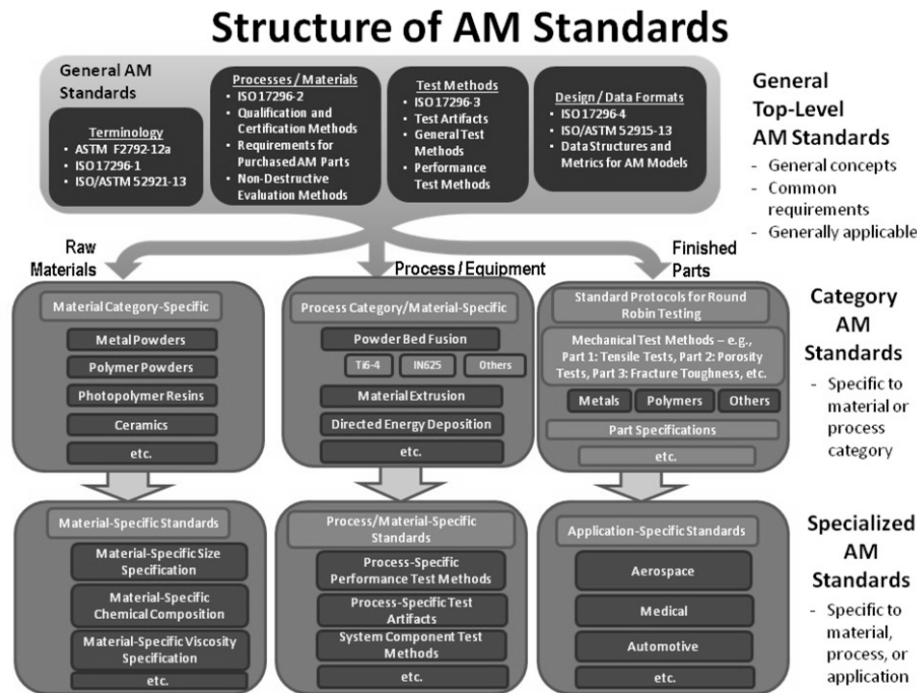


Figure 1. Structure of AM Standards [8]

The European Committee for Standardization CEN CENELEC with the technical body of TC438 is continuing on the work after the SASAM roadmap for the standardization in AM. CEN CENELEC is promoting joint standards inside Europe with their European Norms commonly known as EN standards. Currently they are preparing EN-ISO standards from all of the ISO standards published [9].

In Europe, further national standardization bodies work on AM in parallel to produce national standards: AFNOR in France with its committee UNM 920 Fabrication additive; VDI in Germany with the GPL Committee on Production and logistics; AENOR in Spain with the committee AEN/CTN 116 including AM, SIS in Sweden with the committee SIS/TK 563; and BSI in UK with the committee AMT/8 [10].

2.2.1. Terminology

The terminology for AM was firstly defined in ASTM F2792 [11] standard, where tradenames were categorized into larger groups. In there it was also established that 3D printing would refer to consumer, commercial method for manufacturing plastics as Additive Manufacturing would refer more industrial usage and other materials. The F2792 was later replaced with the current naming standard: ISO/ASTM 52900: Additive Manufacturing – General Principles and terminology [12]. In this thesis, standardized naming defined in ISO/ASTM 52900 is used and pre-standard naming of a process might be referred to in historical context, but it will be defined by the new standardization naming.

Terminology defined in standard ISO/ASTM 52900 [12]:

- **3D printer**, is a machine used for 3D printing.
- **Additive manufacturing (AM)**, is a process of joining materials to make parts from 3D model data, usually layer upon layer, as opposed to subtractive manufacturing and formative manufacturing methodologies.

Terminology for AM methods in ISO/ASTM 52900 [12]:

- **Binder jetting**, is an additive manufacturing process in which a liquid binding agent is selectively deposited to join powder materials.
- **Directed energy deposition (DED)**, is an additive manufacturing process in which focused thermal energy is used to fuse materials by melting as they are being deposited.
- **Material extrusion** is an additive manufacturing process in which material is selectively dispensed through a nozzle or orifice.
- **Material jetting**, is an additive manufacturing process in which droplets of build material are selectively deposited.
- **Powder bed fusion**, is an additive manufacturing process in which thermal energy selectively fuses regions of a powder bed.
- **Laser sintering (LS)**, is powder bed fusion process used to produce objects from powdered materials using one or more lasers to selectively fuse or melt the particles at the surface, layer upon layer, in an enclosed chamber.
- **Sheet lamination**, is an additive manufacturing process in which sheets of material are bonded to form a part.

- **Vat photopolymerization**, is an additive manufacturing process in which liquid photopolymer in a vat is selectively cured by light-activated polymerization.
- **3D printing**, is the fabrication of objects through the deposition of a material using a print head, nozzle, or another printer technology.

Terminology for AM process in ISO/ASTM 52900 [12]:

- **Build chamber**, is enclosed location within the additive manufacturing system where the parts are fabricated.
- **Build cycle**, is single process cycle in which one or more components are built up in layers in the process chamber of the additive manufacturing system.
- **Build envelope**, is the largest bounding area of maximum dimensions of the x-, y-, and z-axes within the building space where parts can be fabricated.
- **Build platform**, of a machine, base which provides a surface upon which the building of the part/s is started and supported throughout the build process.
- **Build space**, is the location where it is possible for parts to be fabricated, typically within the build chamber or on a build platform.
- **Build surface**, is an area where the material is added, normally on the last deposited layer which becomes the foundation upon which the next layer is formed.
- **Build volume**, is the total usable volume available in the machine for building parts.
- **Feed region**, in powder bed fusion, location/s in the machine where feedstock is stored and from which a portion of the feedstock is repeatedly conveyed to the powder bed during the build cycle.
- **Layer**, of matter material laid out, or spread, to create a surface.
- **Machine coordinate system**, is three-dimensional coordinate system as defined by a fixed point on the build platform with the three principal axes labelled x-, y-, and z-, with rotary axis about each of these axes labelled A, B, and C, respectively, where the angles between x-, y- and z- can be Cartesian or defined by the machine manufacturer.
- **Manufacturing lot**, is set of manufactured parts having commonality between feedstock, production run, additive manufacturing system, and post-processing steps (if required) as recorded on a single manufacturing work order.
- **Origin**, is zero point, (0, 0, 0), when using x-, y-, and z-coordinates, designated universal reference point at which the three primary axes in a coordinate system intersect.

- **Overflow region**, is in powder bed fusion systems, location/s in the machine where the excess powder is stored during a build cycle.
- **Part location**, is the location of the part within the build volume.
- **Process parameters**, is the set of operating parameters and system settings used during a single build cycle.
- **Production run**, consists of all parts produced in one build cycle or sequential series of build cycles using the same feedstock batch and process conditions.
- **System set-up**, is the configuration of the additive manufacturing system for a build.
- **Build orientation**, of a part is the orientation of the part as it is placed in the build volume.
- **STL**, is the file format for model data describing the surface geometry of an object as a tessellation of triangles used to communicate 3D geometries to machines in order to build physical parts.
- **Additive Manufacturing File Format (AMF)**, is the file format for communicating additive manufacturing model data including a description of the 3D surface geometry with native support for colour, materials, lattices, textures, constellations and metadata.
- **Part cake**, is the lightly bound powder surrounding the fabricated parts at the end of a build cycle in a powder bed fusion process that uses a heated build chamber.
- **Post-processing**, is one or more process steps, what are taken after the completion of an additive manufacturing build cycle in order to achieve the desired properties in the final product.
- **Powder batch**, is the powder used as feedstock which could be used powder, virgin powder or a blend of the two.
- **Powder bed**, is the build area in an additive manufacturing system in which feedstock is deposited and selectively fused by means of a heat source or bonded by means of an adhesive to build up parts.
- **Powder blend**, is the quantity of powder made by thoroughly intermingling powders originating from one or several powder batches of the same nominal composition.
- **Powder lot**, is the quantity of powder produced under traceable, controlled conditions, from a single powder manufacturing process cycle.
- **Used powder**, is the powder that has been supplied as feedstock to an AM machine during at least one previous build cycle.
- **Virgin powder**, is unused powder from a single powder lot.

Terminology for AM parts in ISO/ASTM 52900 [12]:

- **Part**, is the joined material forming a functional element that could constitute all or a section of an intended product.

- **Accuracy**, is the closeness of agreement between an individual result and an accepted reference value.
- **As built**, refers to the state of parts made by an additive process before any post processing, besides, if necessary, the removal from a build platform as well as the removal of support and/or unprocessed feedstock.
- **Fully dense**, is the state in which the material of the fabricated part is without significant content of voids.
- **Porosity**, is the property referring to the presence of small voids in a part making it less than fully dense.
- **Repeatability**, is the degree of alignment of two or more measurements of the same property using the same equipment and in the same environment.

2.2.2. AM Methods

Binder jetting, is an additive manufacturing process, where a liquid bonding agent is selectively deposited to join powder materials (Figure 2). The binder can have different properties allowing tailored material properties (i.e. conductivity, flexibility, stiffness). Binder jetting manufacturers are for example: ExOne, 3D Systems, HP and Voxeljet.

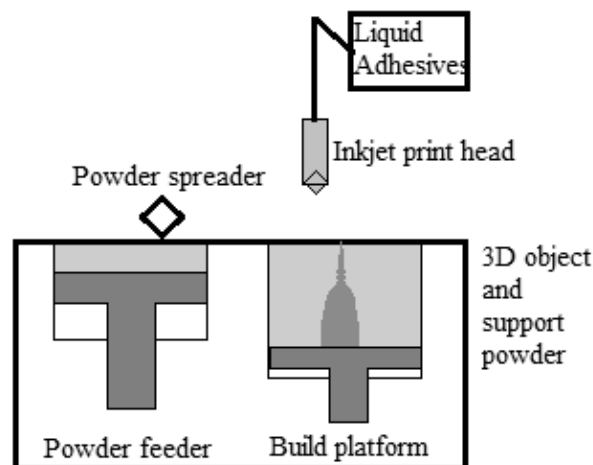


Figure 2. Binder jetting

Directed energy deposition (DED), is an additive manufacturing process in which focused thermal energy is used to fuse materials by melting as they are being deposited (Figure 3). DED is defined in ASTM F3187 Standard guide for Directed Energy Deposition of Metals [13]. Feedstock for material can be in powder or wire form. The energy source is a laser or electron beam or energy arc. Energy arc originates from corresponding welding methods using metal inert / active gas (MIG/MAG) and tungsten inert / -active gas (TIG/TAG).

DED allows multi axis manufacturing and it is forecasted to become more important in recent future. This is backed development in aviation e.g. Boing and Norsk Titanium using plasma depositing DED method for Boing 787 titanium structural parts and it is estimated that by using DED it would possible to save 2 – 3 million USD per plane [14] in material costs.

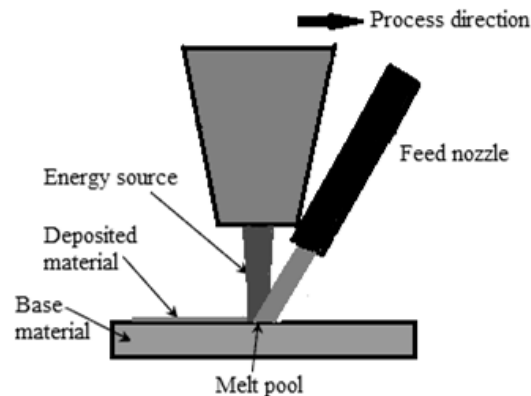


Figure 3. Direct energy depositing process in wire or powder base method.

Material extrusion, is an additive manufacturing process in which material is selectively dispensed through a nozzle or orifice. Also known as 3D printing. Please refer to Material Extrusion subchapter on page 15.

Material jetting, is an additive manufacturing process in which droplets of build material are selectively deposited and solidified droplets create 3D part (Figure 4).

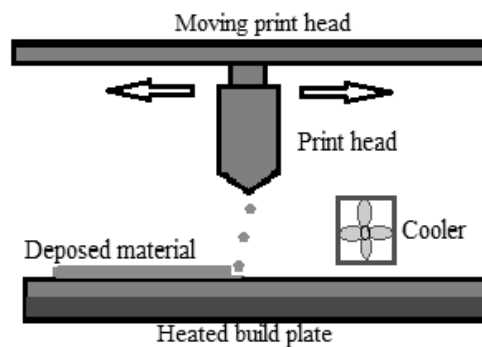


Figure 4. Material jetting process

Powder bed fusion, is an additive manufacturing process in which thermal energy selectively fuses regions of a powder bed. Please refer to the subchapter of Laser Powder Bed Fusion (LPBF) on page 22.

Sheet lamination, is an additive manufacturing process in which sheets of material are bonded to form a part (Figure 5). Sheets can be paper sheets that are cut and bonded into 3D shape or metal sheets that are cut and bonded e.g. ultrasonically.

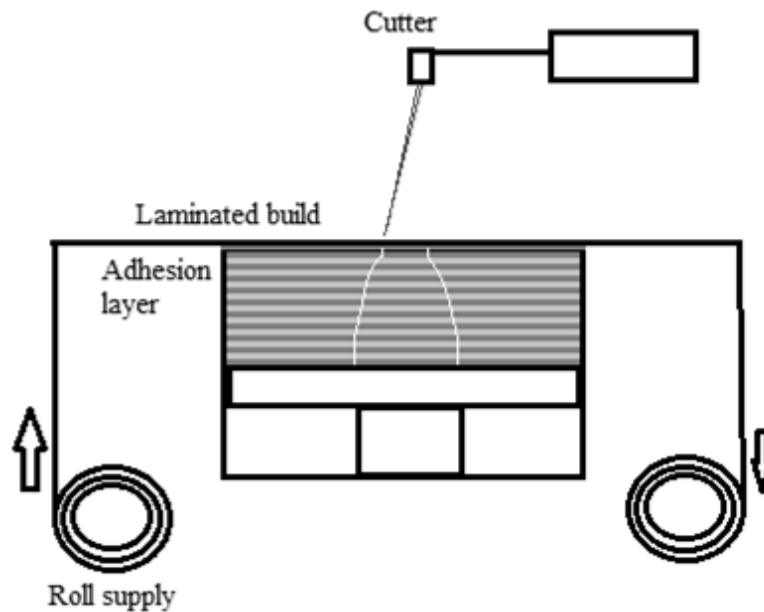


Figure 5. Sheet lamination process.

Vat photopolymerization, is an additive manufacturing process in which liquid photopolymer in a vat is selectively cured by light-activated polymerization (Figure 6). Photopolymers are polymeric resins that light sensitive. The first SLA printers use this technology. Curing of resin leaves good surface quality with accuracy. The vat photopolymerization uses thermoset resins and due to the way of polymerization from monomers into polymers via light, the anisotropy has less impact than in other 3D printing methods.

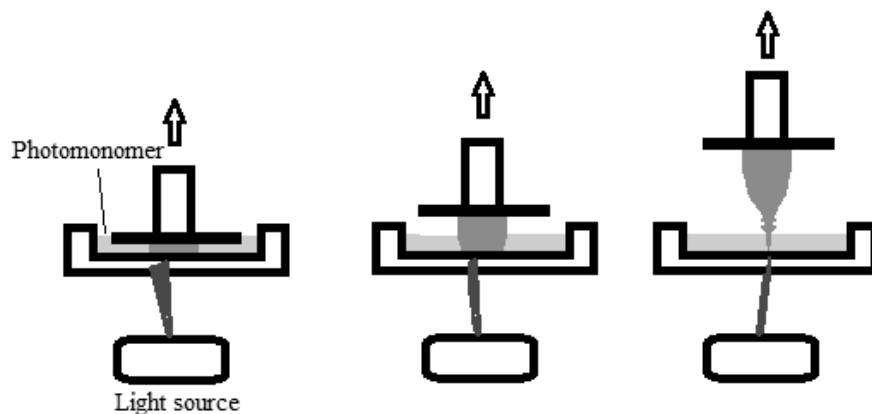


Figure 6. Vat photopolymerization process.

2.2.3. List of Published AM Standards

Design

ISO / ASTM52915 - 16	Standard Specification for Additive Manufacturing File Format (AMF) Version 1.2
ISO / ASTM52910 - 17	Standard Guidelines for Design for Additive Manufacturing
ISO 17296 - 4 : 2014	Additive manufacturing -- General principles -- Part 4: Overview of data processing

Materials and Processes

F2924 - 14	Standard Specification for Additive Manufacturing Titanium-6 Aluminum-4 Vanadium with Powder Bed Fusion
F3001 - 14	Standard Specification for Additive Manufacturing Titanium-6 Aluminum-4 Vanadium ELI (Extra Low Interstitial) with Powder Bed Fusion
F3049 - 14	Standard Guide for Characterizing Properties of Metal Powders Used for Additive Manufacturing Processes
F3055 - 14a	Standard Specification for Additive Manufacturing Nickel Alloy (UNS N07718) with Powder Bed Fusion
F3056 - 14e1	Standard Specification for Additive Manufacturing Nickel Alloy (UNS N06625) with Powder Bed Fusion
F3091 / F3091M - 14	Standard Specification for Powder Bed Fusion of Plastic Materials
F3184 - 16	Standard Specification for Additive Manufacturing Stainless Steel Alloy (UNS S31603) with Powder Bed Fusion
F3187 - 16	Standard Guide for Directed Energy Deposition of Metals
ISO / ASTM52901 - 16	Standard Guide for Additive Manufacturing – General Principles – Requirements for Purchased AM Parts
ISO 17296 - 2 : 2015	Additive manufacturing -- General principles -- Part 2: Overview of process categories and feedstock

Terminology

ISO / ASTM52900 - 15	Standard Terminology for Additive Manufacturing – General Principles – Terminology
----------------------	--

Test Methods

F2971 - 13	Standard Practice for Reporting Data for Test Specimens Prepared by Additive Manufacturing
F3122 - 14	Standard Guide for Evaluating Mechanical Properties of Metal Materials Made via Additive Manufacturing Processes
ISO / ASTM52921 - 13	Standard Terminology for Additive Manufacturing-Coordinate Systems and Test Methodologies
ISO 17296 - 3 : 2014	Additive manufacturing -- General principles -- Part 3: Main characteristics and corresponding test methods

2.2.4. Outlook

SASAM's roadmap for standardization from 2014 (Figure 7) indicates the direction where the AM society is targeting the standardization efforts. By 2017, standards have come to include powder bed fusion methods for metals and polymers and in addition the DED method for metals. For powder bed fusion the most high of high value metal materials are available. Also buying guides for industry have been compiled. Therefore, AM has a good start with standardization for manufacturing industry's needs. In 2016 and 2017 the maturation process has made it possible to notice more interest in metal additive manufacturing based on these facts alone.

Technological maturation also will allow eventually additively manufactured parts to be able to use in aviation. This can be concluded for example from REGULATION (EC) No 216/2008 [15] that gives the basic rules for civil aviation production organizations in the area of European Union. In the regulation is stated (EC 216/2008: article 5, 6b) that the certification process of parts for aviation has to take into account aircraft experiences in service, and scientific and technical progress. This will eventually mean that designing for AM in aviation parts, original equipment manufacturers (OEM) certifications for airplanes and standardization will certainly drive further adaption of AM as more proof of the technology and experiences are gain.

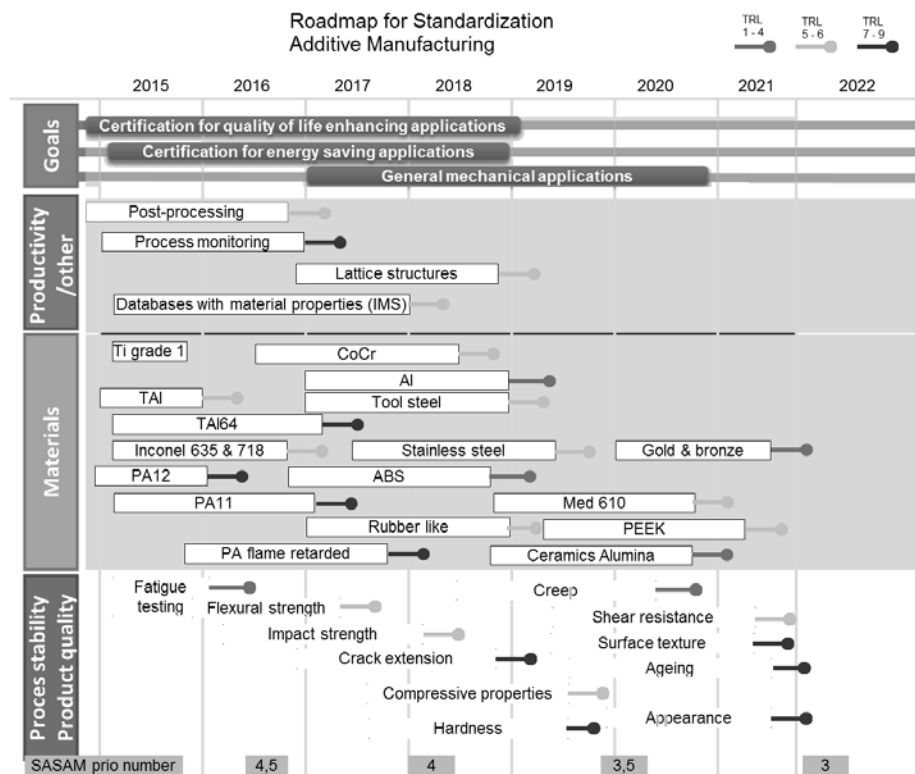


Figure 7. Roadmap for Standardization. SASAM [8]

2.3. Manufacturing Methods Used Experimentally

As already stated before, additive manufacturing is regularly called 3D printing in the common language of the people. It has become a synonym for layer based manufacturing. In the industrial context 3D printing refers to polymeric based manufacturing methods. These methods have 80 % of the whole materials market in additive manufacturing according to Wohlers report 2015 [1] and that makes polymers important. In the thesis two fabrication methods for polymeric materials are used, material extrusion what is also known as 3D printing (3DP) and Selective Laser Sintering (SLS). These methods are described in detail in the following subsections 2.3.1 and 2.3.2. The major part of the AM methods are introduced briefly in previous chapter 2.2.2. AM Methods. Whereas, metal additive manufacturing method used in experiments is based on the powder bed fusion technology.

2.3.1. Material Extrusion

Material extrusion 3D printing (3DP) is also known as Fused Deposition Modelling (FDM) and is a manufacturing process where the material is heated over the glass transfer temperature and extruded through a nozzle on two-dimensional layers. It was patented by Stratasys corporation in 1989 [16].

Material extrusion is based on a heated syringe where the thermoplastic is pushed from a spool or pellets. A nozzle in the syringe heats the thermoplastic into a glass transfer temperature and the polymeric filament is extruded out from the nozzle. The nozzle is controlled precisely by a microprocessor in Cartesian coordinates. The thermoplastic is extruded on a building platform according to sliced 2D instructions representing a slice of the 3D model. This extrusion process continues from the base until the end creating a part of plastic.

The simple design of a material extrusion printer (Figure 8) consists of one nozzle, unheated bed, motors controlling the axis and a control microprocessor. The 3D printing hype started after 2005 with open source RepRap project [17] providing information for makers to produce their own 3D printer. In more complex design additional nozzles can be added to extrude other materials i.e. solvable support material.

3D model is sliced into slices of deposit layer. This is done with slicer software (e.g. Slic3r [18], Magics) that also decides the tool paths for the nozzle to take and filling of the model. The open source slicers create a gcode string that is a common language with computer numerical cutting (CNC) machines. A look inside of a slicer is given by open source Slic3r program and its manual [18]. A gcode includes among other things: extrusion temperature, -speed, infill patterns, -density, -optimization, support material information and layer height.

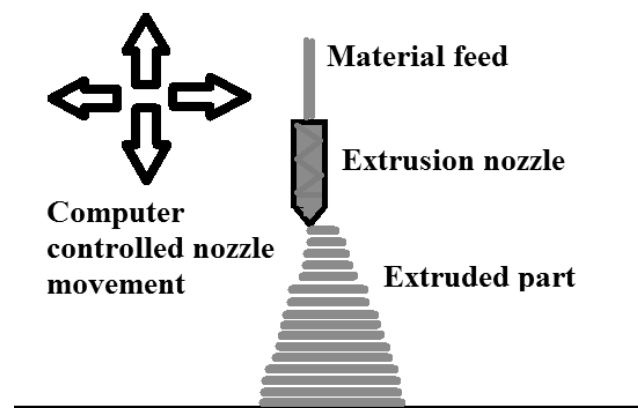


Figure 8. Schematic of material extrusion.

For a model to be printed, infill is important for its mechanical properties. Cavities, printing direction and lack of fusion have a high effect on mechanical strength. However, in research [19] about infill patterns found out that the infill pattern is not as crucial to mechanical properties as infill density. The tool path affects the density of extrusion printed parts as Figure 9 presents. When the slicer crates a tool path it needs to be continuous and the extrusion nozzle is not able to

project sharp corners and holes always accurately creating materials lack of continuity. This is even more problematic than in discrete layer boundaries. A collection of material extrusion mechanical properties is Figure 10 from different materials and filler blends. The filament e.g. for PLA can handle 65 MPa stress along the filament and the fibers but it might handle only 30 MPa stress perpendicular to that. Therefore, the building direction is important and the mechanical properties of 3DP are wide.

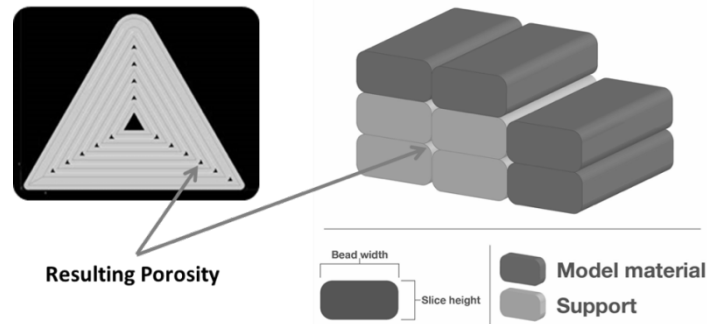


Figure 9. Porosity between extrusion layers [20]

Plastic materials are suited for extrusion well and used in 3D printing are listed in the Table 1. These polymers do not include variants or blends of polymers. There are various materials from the most general ABS and PLA to more specific materials for usage as acid resistant PVDF.

Table 1. Common material extrusion materials

ABS	Acrylonitrile Butadiene Styrene
PC	Polycarbonate
ASA	Acrylonitrile Styrene Acrylate
PEEK	Polyether Ether Ketone
PET	Polyethylene Terephthalate
PLA	Poly Lactid Amide
PA	Poly Amide
PPSF/PPSU	Polyphenylsulfone
HDPE	High Density Poly Ethylene

PVDF	Polyvinylidene fluoride
PHA	Polyhydroxy-alkanoates
PVA	Polyvinyl alcohol
PVC	Polyvinyl chloride

Material extrusion has many applications and the most interesting one is made by MADE IN SPACE INC, what provided a 3d printer to the International Space Station (ISS) in 2015. The first material extruded by “the made in space” printer in space was ABS and it has been extended in 2017 to PEEK manufactured by Stratasys [21]. Similarly to extrusion printing, a wire-based metal AM method has been tested in zero-g flights and it is waiting to be developed further ISS application.

Powerful tool with thermoplastics is to recycle plastic the waste by transforming it into new filament. Thermoplastics are perfect for recycling as those can be remolten without property losses, unlike with thermosets. When considering plastic recycling, the plastics used are thermoplastics and those have been recycled throughout decades [22] [23] [24].

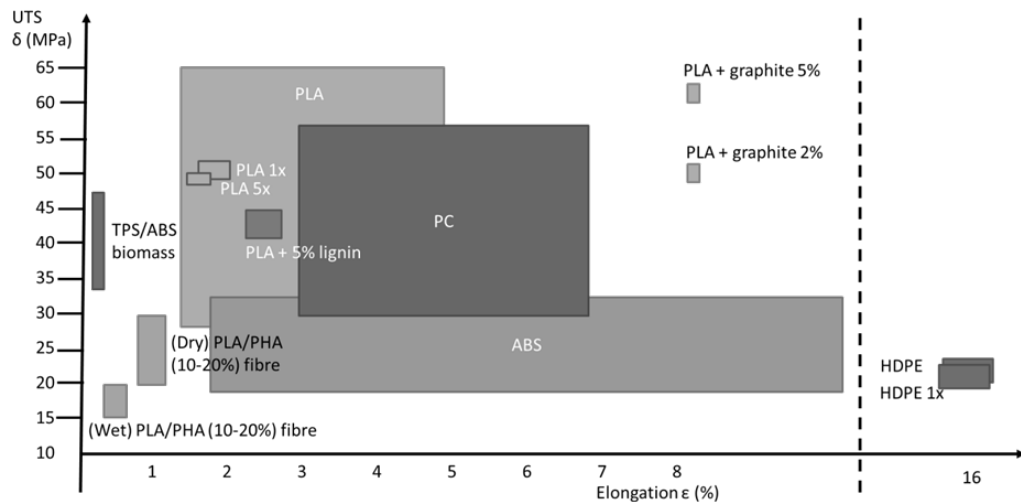


Figure 10. Tensile strength and elongation of fabricated parts with material extrusion.

When recycled the material is transformed by mechanical shredding into pellets and this cutting phase leads to some degree of degradation of the polymer chains. Degradation is an irreversible process leading to a significant change in the structure of the filament material resulting in loss of properties. Cruz et al. [25] recycled PLA filaments 5 times and noticed degradation of the filament during those recycling. A trend caused by mechanical shredding of the filament

many times shortened the polymer length as in recycling of normal plastics have been noticed [26] [27]. A decrease of the polymer molecular weight of about 47% after 5 recycling cycles was reported an increase in crystallinity of the polymer. The loss in molecular weight caused lowered tensile strength and elongation from 1.88% to 1.68%, but did not affect the yield stress. Material flow ability increased as viscosity reduction of 80% after 5 recycling cycles.

Thermoplastic recycling to new filaments is not a new idea and it has been demonstrated by Kreiger [28] and Baecher [29], who created their own filament extruder. Also, commercial extruders can be used as Hamod [30] showed. Whoever owns a shredder and an extruder can directly turn cleaned and homogenous waste plastics (e.g. PET, HDPE) into low-cost filament. However in a wider study about the economics of recycled HDPE filament production. Kreiger et al. [28] states that individual collection might not be as efficient as centralized collection and filament production. An estimate of the price difference and the economic opportunity is given by Baechler et al. [29], who calculated that the cost of producing recycled HDPE filament was between 2 and 3 USD per kilogram with a homemade extruder, while the commercial filament is sold at an average price of 38 USD per kilogram. The opportunity of recycled filament manufacturing has been claimed partially by companies similar to Fila-Cycle [32] in the UK. It is marketing and selling filaments: rPLA from yogurt pots and commercial left overs, rABS and rHIPS from automotive waste.

The mechanical properties reported [37, 38] for recycled HDPE prints were lower than those of the same pieces made of virgin material. However, this is not supported by Hamod [30] who achieved similar mechanical properties for both virgin HDPE and recycled HDPE. For a more accurate description of recycled filaments and material properties, more information about the source plastic material should be needed. For example what is the polymer condition and how much of it is already recycled plastic. Reclaimed plastics like HDPE milk jugs and washing liquid jugs, might have recycled material in them and therefore one can ask how much impurities have been introduced in the material before reuse. The filament decay by cycles was well described by Cruz et al. [25] for PLA and Torres et al. for injection moulding [31].

For everyone dealing with 3DP, it is a common problem of sorting different plastics after printing. It is not easy to detect different plastic varieties in pieces and wastes. Plastic waste is often collected into a bin. To help identifying the thermoplastics after 3D printing, recycling material dependent coding is proposed and investigated by Hunt et al. [32]. Plastic identifiers should be standardized and made as easy as possible for the user to apply and decide where to place the markings as required aesthetics and mechanical properties should not be compromised by the marking.

2.3.2. Selective Laser Sintering

Selective laser sintering (SLS) or Laser Sintering (LS) is additive manufacturing powder bed fusion method (PBF) for polymeric materials. The process bears similarities to metal PBF consisting (Figure 11) of a powder bed, where a layer of plastic powder is spread, a powder feeder and a laser heat source. The laser melts the plastic powder layers according to the 2D slice data. Unlike in metal application, the LS does not need support structures.

During the build cycle the powder bed is heated few degrees below of the melt temperature of the material to optimize the energy input by the laser and remove possible distortions in the part. Polymers absorb laser energy in far infrared (wavelength 9 – 12 μm) and ultraviolet regimes (wavelength 125 – 350 nm), therefore, CO₂- (9.4 – 10.6 μm) and excimer lasers are used for polymer processing and in comparison Nd:YAG lasers used in metal LPBF a use wavelength between 950 – 1400 nm. CO₂-lasers are the prime choice for polymer processing. The processing happens in shielding nitrogen atmosphere and after the build has completed the chamber is cooled down below temperatures where any glass transition or oxidation could happen. [33]

Laser sintering parameters include:

- Part bed temperature
- Feed bed temperature
- Layer thickness
- Laser power
- Scan spacing
- Heating and cooling rates

High build bed temperature could result in undesired powder bonding to part and fusion in unused powder. Low build temperature could induce warping of the parts and unmolten particles. Bed temperature is kept 3 – 4°C below the melt temperature of the polymer. Inconsistent heating can cause porosity, particle coring and thermal degradation of the powder. [33]

Mechanical properties gained with LS are not as good as achieved with injection moulding (IM). [34] Ajoku et al. found in their research in case of PA-12 (Nylon 12) the modulus during compression was 10% lower in LS part than in IM part. This lower result can be explained by residual porosity inside of the LS parts. In addition a brittle behavior and increased strength are experienced with LS parts when IM parts behave tough. The porosity of LS structure comes from inconsistent powder spreading and filling, unmolten particles and powder layer interface. It is also measured that in LS the z-direction yield and tensile strength is 10 % different than x- and y-axis [33] [35].

LS does not need support structures as in case of metal LPBF. This is due to the different way plastics and metals behave. Metal's molten viscosity is low and

it doesn't change dramatically after heating or depending on the shear speed [36] meaning that metals are Newtonian fluids in the liquid state. For polymers, the rheological behaviour varies differently by temperature, composition and chain length. The thermoplastics behave as at first as Non-Newtonian fluids in the molten state and then plastic flow highly depends on the shear speed [37]. With higher shear speeds plastics encounter shear thinning that reduces the viscosity of the material. Temperature decreases the viscosity of polymers and too high power input might create low enough viscosity for the polymer to sink into powder bed creating a sinkhole [33].

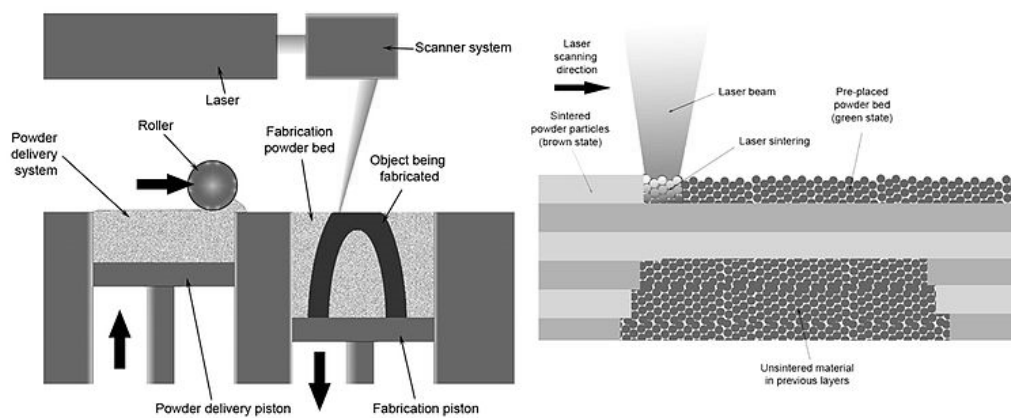


Figure 11. Laser sintering process. [38]

Extraction of commercial LS materials is mentioned in Table 2. The table considers materials available from EOS, Stratasys and 3D Systems. There are only a few main polymers in the list as Polyamide (PA) with its variations (PA 11 and 12) dominates the materials market for LS. Polystyrene that is used for lossless casting molds and PEEK for medical applications. Limitations for the material selection of the polymers come additionally from design choices of the machinery. As the LS machines were primarily designed for PA materials in mind, the temperature range achieved does not allow other materials with higher melting point (i.e. PEEK) to be used in the machines. Redesigns with higher temperatures and powerful lasers have been done to achieve PEEK manufacturing for the LS [33].

Table 2. LS Materials available

PA	Poly Amide
PS	Poly Styrene
PEEK	Polyether Ether Ketone
TPE	Thermoplastic Elastomers

2.3.3. Laser Powder Bed Fusion (LPBF)

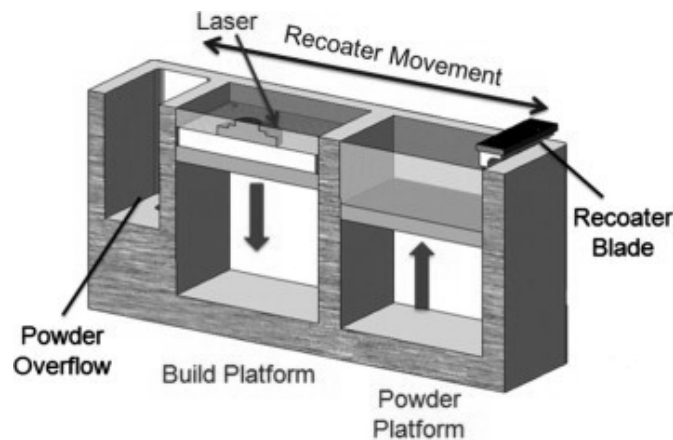


Figure 12. Laser Powder Bed Fusion [39]

Powder bed fusion fabrication is one of the most popular layer wise manufacturing method. It has gained momentum as it is accurate [40] and parts manufactured with the process have been able to be certified for flying. In the powder bed fusion process a layer of powder is spread on a building platform and the layer is molten with a heat source. Depending on the heat source the methods divide into laser and electron beam fabrication. After fusing the powder together a new powder layer is deposited on top of the previous layer and the process starts again. The molten layer has to be built on solid material or support structures, what can handle the heat expansion and stresses from the solidification of the molten layer.

Laser powder bed fusion (LPBF) is a method of AM where a layer of metal is selectively molten with a laser heat source. The method is often also referred as trademarked names of Direct Metal Laser Sintering (DMLS) by EOS, Selective Laser Melting (SLM) by SLM Solutions and Laser Cusing by Concept Laser.

Table 3. Process variables during LPBF manufacturing.

Process Parameters		Material Properties
Laser power	Laser beam radius	Chemical composition
Scanning speed	Scanning strategy	Particle shape
Hatching distance	Layer thickness	Particle size and distribution
Shielding atmosphere	Gas flow	Thermal conductivity
Building orientation	Build bed temperature	Melting temperature
Laser type	-	Reflectivity

LPBF is a complex process with many process parameters affecting the quality of the process. A summary of important parameters is compiled in Table 3. The parameters are divided into two main categories: process parameters and material parameters. **Process parameters** are machine dependent and change with the AM-machine. Changing one of these preconditions also influences the results gain. For example, shielding gas [41] can take impurities from the atmosphere and raise the number of elements present in the manufactured part. Therefore, it is necessary to validate the method and possible changes before manufacture. The machine parameters are laser type, power, shape and gas flow characteristics. Laser source depends on the method and the materials used in creating the beam. Not all lasers are equal in the wavelength or absorption of specific materials. In addition to machine parameters it is possible by the operator to change build strategies used by the machine: hatching distance, scanning speed and scanning strategy. More general in build process parameters, but important, are layer thickness, build orientation, build bed temperature and shielding gas type.

Material and powder properties are the material specific uncertainty in the AM-process. Chemical composition plays an important role in the material as the original microstructure with the alloying elements affects the material. Heat source like laser or electron beam can vaporize particles and some of the light weight alloying elements and hence change the chemical composition of the AM-part. Unmolten high temperature resistant particles can also be left in a new alloy due to low heat input. Powder shape, size and distribution affect the flow characterization of the powder and the spreading on the build plate. Good powder distribution with large and small particles creates high dabbing density alongside with spherical particles: these provide homogenous spreadability on the building platform. The thermal conductivity of the powder affects to heat dissipation from the melt pool to surrounding areas enlarging the heat affected zone (HAZ) and sintering powder particles on the surface. The reflectivity of metal as molten and as powder form is less than the reflectivity as bulk. A deposited surface can become a mirror for the laser below a new powder layer. Melting temperature

affects the densification of the powder. Power input should be high enough to fully melt the powder and fuse it to below as a new layer on the part.

Powder for LPBF should be spherical and fully dense as Figure 13 shows the gas atomized powders to be. Three standard alloys (List of Published AM Standards) have already been published for powder bed fusion in titanium alloy, nickel based alloys and steel. These standards aim to clarify the quality issues between different powder manufactures. The spherical shape gives the powder excellent flowability and spreadability during the process. Gas atomized powders have fewer pores and impurities inside of the powders and therefore gas atomized powders are preferred in the LPBF manufacturing. There are other powders, e.g. water atomized powders, which have two disadvantages such as irregular shape (Figure 14) and impurities. Powder needs to be dense as well as spherical, therefore, spheroidized powders (Figure 15) with large porosity is not suitable for LPBF manufacturing.

Powder has a mean size ranging from 10 μm to 50 μm , and it is generally assumed that the largest powders determine the layer thickness. The smaller the powder is, the smaller can be the layer thickness and the finer can be the details achieved in theory. At some point when the particle sizes are small, the fineness will not have an effect on the feature size but on the effective laser spot size takes over this.

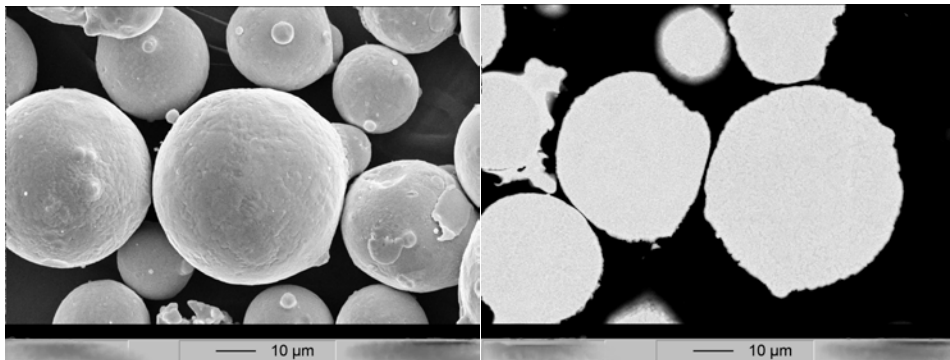


Figure 13. Gas atomized powder [42]

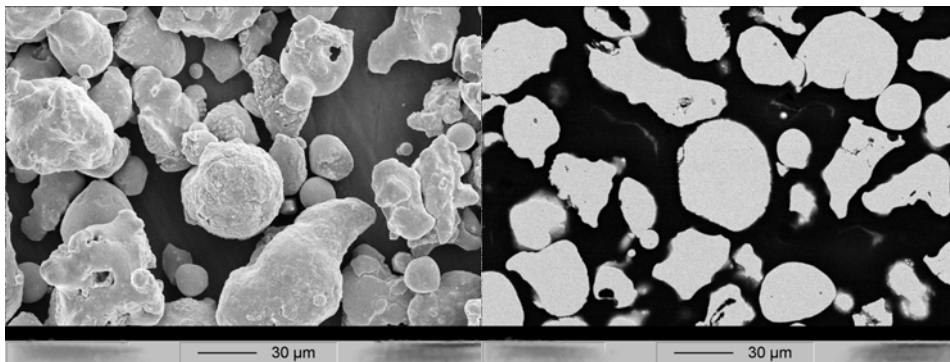


Figure 14. Water atomized powder [42]

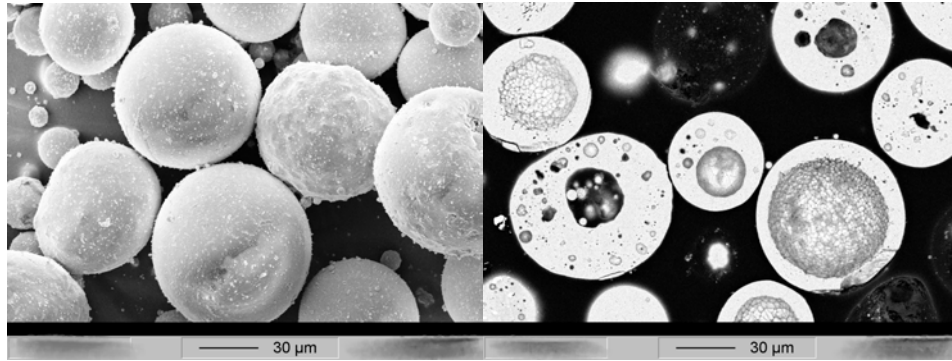


Figure 15. Spheroidized powder [42]

Scanning strategy is a path how the heat is deposited on the surface of the AM-piece. The melting from laser scanning strategies affect in porosity, surface roughness, microstructure, heating and residual stresses of the finished piece. The AM-machine assigns scanning strategy for the 2D layer by itself depending on the regions around it. There are 4 different regions: Contour, where there is nothing next to the skin. Core, where all sides have material around. Down skin, where there is nothing below of the build. Up skin, where is nothing on top of the build. These different build strategies have individual parameters assigned and the use of those are destined to create the best build quality by assigning different parameters to the most crucial points. For example, a thin walled section needs more precision than a bulk section of the material, which can be fused with more power and speed.

Scanning patterns can be divided into three main strategies: stripe, checkerboard and island strategy. Every scan can be either unidirectional or bidirectional (Figure 16). The scanning lines can be made once or in a patterned way (Figure 17) and altering the pattern will mix the microstructure. In stripe scanning strategy (Figure 18) the surface is manufactured with stripes in the same direction. The stripes are the width of the effective laser spot size and have spacing of a hatching distance. The lines keep the direction between the scan areas and these areas overlap each other.

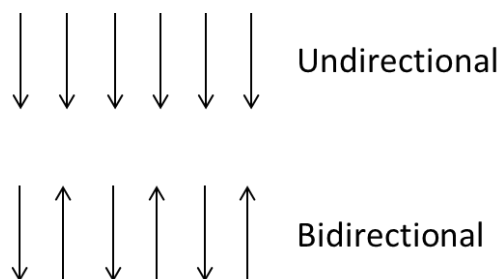


Figure 16. Direction of the scan.

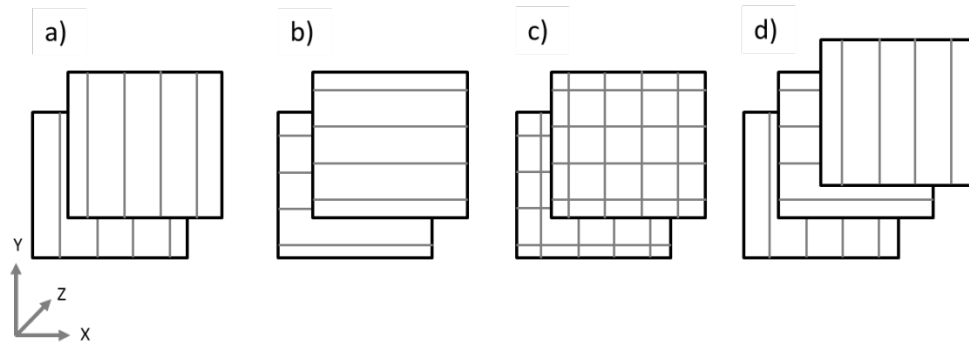


Figure 17. Scanning strategies: a) and b) linear and parallel, c) perpendicular and d) alternative scanning

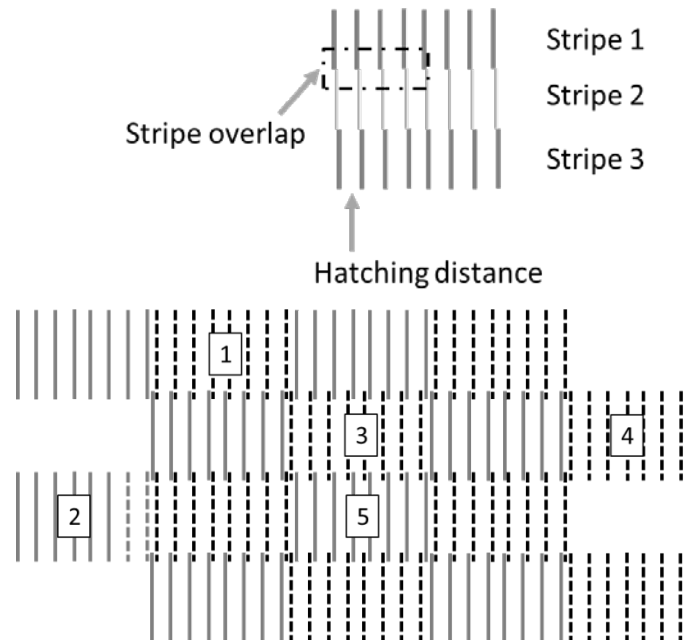


Figure 18. Stripe pattern

Checkerboard pattern is defined with squares that are like in a checkerboard. When in line pattern the regions had the same direction (Figure 18) in checkerboard pattern these regions are perpendicular (Figure 19). The areas overlap by hatching distance.

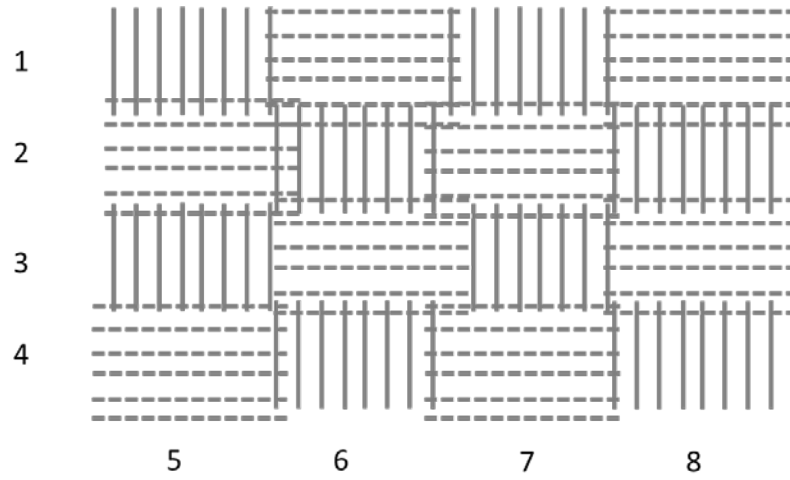


Figure 19. Checkerboard pattern

Islands pattern is a randomized version of checkerboard pattern where the same pattern is not reproduced layer by layer but the direction and fusing order changes randomly (Figure 20).

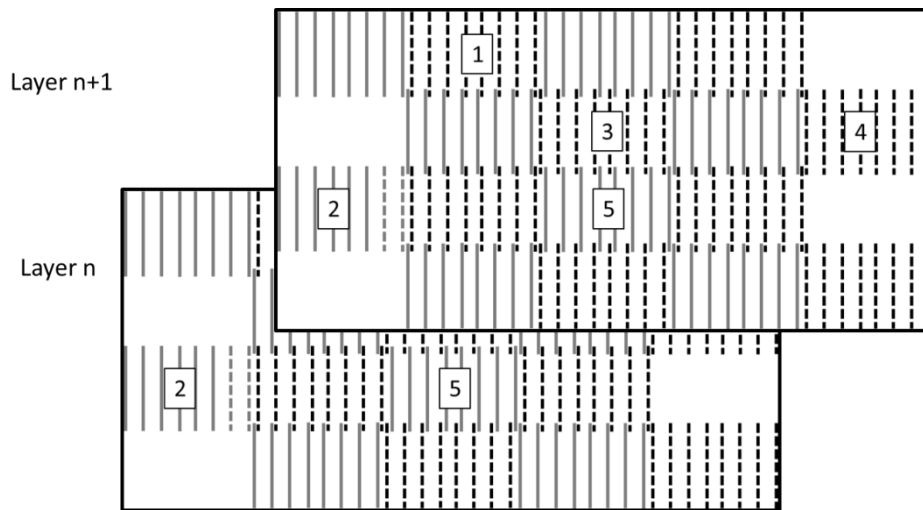


Figure 20. Island pattern in scanning strategy.

The differences in scanning strategies affect microstructure by changing different melt pool orientations and mixing these melt pools. The varying place of the checkerboards and the change of orientation of the laser as in EOS M LPBF AM-machines (Figure 21) has 67-degree varying angle between every layer. As 67 is an odd prime number also called as an irregular prime and 360 is not an exact multiple of it, this allows the beam direction to be practically randomized and creating heterogeneous microstructure effects by it. Even with the usage of the off prime number the scanning directions are periodical. This can be proven by writing a short program that counts all the scanning directions and how many layers it takes in order that layer 'n' is the same direction as layer 'n+c', where c

is a constant. It takes 360 layers ($c = 360$) before the scan line of the laser has the same direction as the first scan and the cycle is visualized in Figure 22. During the 360 layers the laser goes through all the directions in discrete 67° steps. The round symmetry makes the 6th layer to be 21-degree rotation from the first one.

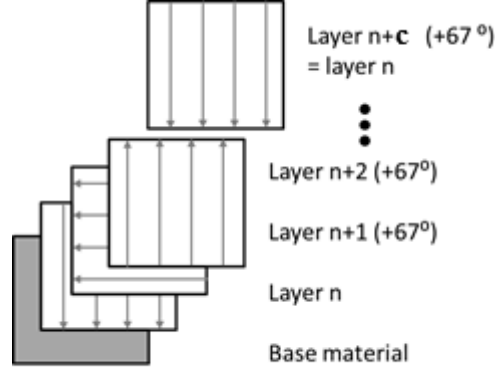


Figure 21. Scanning strategy shift of 67-degrees in EOS M AM-machines depending on the layer.

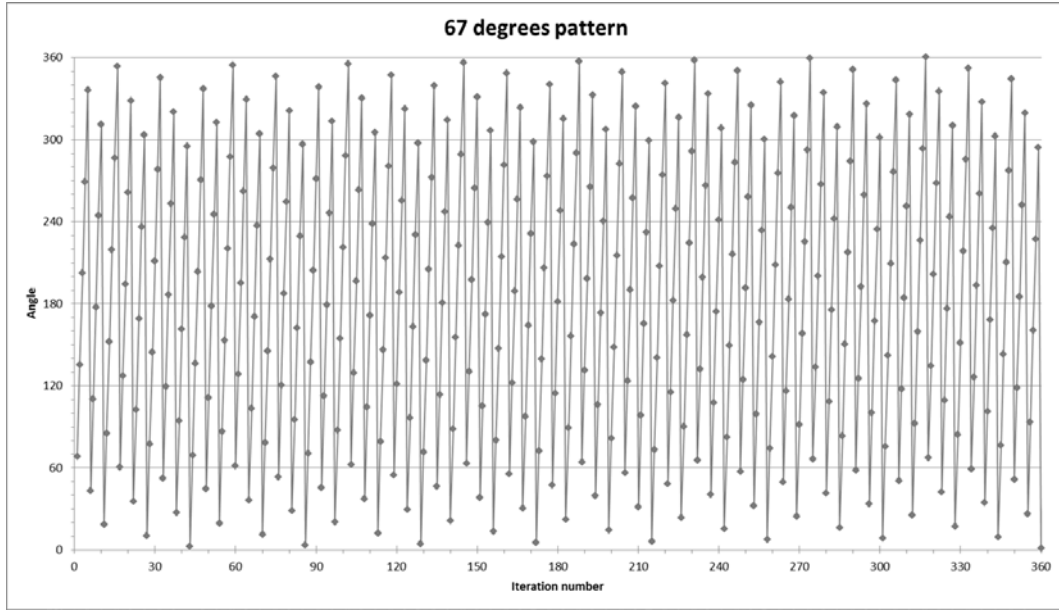


Figure 22. Different angles what laser has with on 67-degree angle rotation before the pattern repeats.

2.3.4. Post Processing in AM

Polymer post processing and post processing for 3DP is an important step as parts are greatly used in aesthetic applications where a customized surface is highly sought after. **Support structure removal** is done mechanically removing the structure. This leaves lower surface quality on the spot where a support structure was present. Therefore, another alternative for support structures is to build those from a different material that is weaker than the original. For example, PS can be used to as a support structure for ABS because it is soluble into limonene and ABS is not. The same way degradable plastics (PVA) can be used as support structure and dissolved in hot water what is harmless for the chosen material.

The surface treatments can be divided into two categories: mechanical and chemical. In mechanical surface treatment **sanding** and **polishing** takes part and smoothen the surface by removing material abrasively from the surface. The piece can be also smoothened with chemicals. In **vapor smoothing** a thermoplastic (e.g. ABS) is subjected to a solvent (e.g. acetylene), what melts a surface layer and lets the surface tension to smoothen the layer gaps. **Painting** can also directly smoothen out the small gaps. If it is not enough **epoxy coating** is an option by dipping or parts of the piece to prepare the surface. Coated surface can handle e.g. different chemical states as the matrix material.

Thermoplastics can be joined together by heating the connection and creating a weld between materials. Alternatively, a joint can be created with another resin (e.g. glue).

Metallic materials post-processing is necessary for all AM-pieces. The design of the components restricts the parts to be anchored onto a building platform with support materials. The support material bears the residual stresses becoming from the solidification of the liquid after melting. Without any support, the liquid would curl into a ball on the powder bed. The support structure will also dissipate heat away from the melt pool and the part. The heat dissipation is important in thick sections. Well-designed support structures keep the part in shape and residual stresses in control before annealing of the stresses in stress relieving. The support structures need to be removed from the piece after stress relieving. This is often done manually by the operator. The places where support structures cannot be removed it is good to design the shape as self-supporting or integrate the supports into the part.

Micro shot-peening is a similar process to sand blasting, where spheres are used to compact and smoothen a surface. High energy spheres are shot on the surface and the surface experiences shower of particles compacting the surface and removing loose material from the surface similarly as reported for AlSi10Mg in [43]. Micro shot-peening provides improved surface quality that is a base for other treatments and by itself is sufficient for LPBF parts but not for EBPBF parts.

Machining is a powerful post processing method for any part. Usually with AM -parts the machining is not wanted as the fabrication is near net shape. The final removing of layers is preferred to be carried out in other ways i.e. shot peening. Sometimes it is not possible to overlook machining as viable option e.g. in case of titanium parts. Instead of removing large quantities of material from forged titanium bulk, small layers can be removed from a near-net-shape AM - part. This provides highly beneficial cost savings in material.

Filing, grinding and polishing are conventional finishing methods for parts and components. These methods are suitable for creating specialized surfaces i.e. draft angles and moulding surfaces with high requirements. Moving into larger production and higher yield of small parts an **abrasive tumbling and vibratory finishing** are automated methods of finishing and rounding up sharp corners from AM-pieces.

Electro chemical polishing (ECM) is possible for all PBF materials and generates smooth surfaces that can be used e.g. in medical applications. In **laser polishing** surfaces are remolten with a laser to give particle free surface.

2.4. Product Driven Design

2.4.1. Topology Optimization

Optimization is long field of study where an optimum solution is searched with computational methods. A solution satisfying design constraints are considered to be optimum. Topology Optimisation (topopt) is in the field of optimization where material is distributed into design volume and the solution is calculated without violating constraints. These constraints are e.g. loads and border conditions that are needed to be defined in order to be able to calculate the optimization problem.

Topology optimization is a powerful computational tool for calculating shapes in Finite Element Method (FEM). For example an existing part is possible to calculate a computer derived shape with topology optimization and check the design with finite element analysis (FEA). What intrigues in topopt that something what have taken from experienced designer years to master and several hours to execute could be produced with computational methods.

However, the computational shapes are not always possible to manufacture with conventional manufacturing. AM is one solution to this manufacturing problem. Where previously an additional constraint for manufacture needed to be used while using topology optimization, AM promises to utilize the full potential of topology optimization.

The general algorithm for the topology optimization (Figure 23) consists of initial starting assumption where design space, constraints and loads are defined. Topology optimization problem is often complex where not all loads can be

defined accurately and constraints need to be reduced as much as possible without losing the accuracy. Optimizer creates a finite element approximation and with matrix calculations proceeding to solve the problem set up by the user.

A design step consists of checking sensitivity in the design. A high sensitivity derives from great element dislocations meaning e.g. that there is not enough material to bear the load and more material needs to be added in this area. The design is updated with help of the sensitivity value and finite element analysis is run for convergence. The convergence is checked in order to have compliance with initial design constraints. If the check fails to complete the design constraints, a new iteration is needed and it is initialized along with the new iteration cycle. The process continues until initial constraints are met and the final design is achieved.

In a case of cantilever, the design is updated as long as the struts are able to hold the mechanical load with the volume fraction given. The structure moves into the flow of stresses maximizing stiffness and minimizing mass. In a simple example it is easy to comprehend but in complex situation experience and the power of mathematics come into play in greated scale.

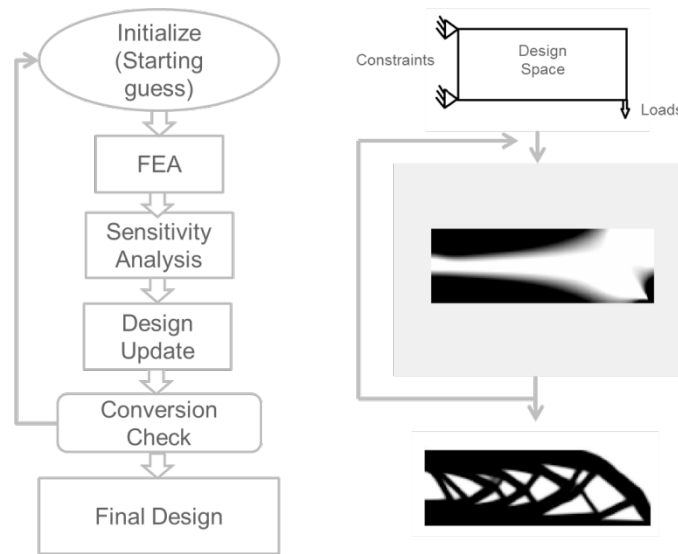


Figure 23. Topology optimization algorithm.

2.4.2. Solid Isotropic Material with Penalization (SIMP)

Solid Isotropic Material with Penalization (SIMP) is a topology optimization (topopt) method is derivated from original works by Bendsoe and Kikuchi in 1988 [44]. The work underpinned SIMP but lacked penalization method. SIMP's purpose is to find an optimal structure by distributing material to satisfy constrictions. Applied loads, support conditions and design volume constrictions are the only known quantities in the problem, the rest can be calculated. In the

topopt problem the connectivity of the structure is unknown before optimization process. [44]

The topopt problem is not represented by standard parametric functions describing topology, shape and size of the structure, but instead by a set of distributed functions defined on a fixed design space Ω . These functions are a parametrization of stiffness tensor in the material. The functions create a continuum that is used to calculate design formulation for the topopt problem similar as represented in Figure 24. The formulation and calculation of these functions are well known but a large number of variables and number of functions creates a computational problem. The simpler the calculation, the faster it is in comparison with detailed calculations. The simplest design problem consists of constraints, designing for minimum compliance (invert of stiffness) under basic constraints. [44]

In Solid Isotropic Material with Penalization method consider a mechanical element as a body occupying in domain Ω_{mat} , that is part of a larger reference domain Ω in R^2 or R^3 . The reference domain allows the definition of the applied loads and boundary conditions in order to find optimal stiffness tensor $E_{ijkl}(x)$ from internal virtual work Equation 1.

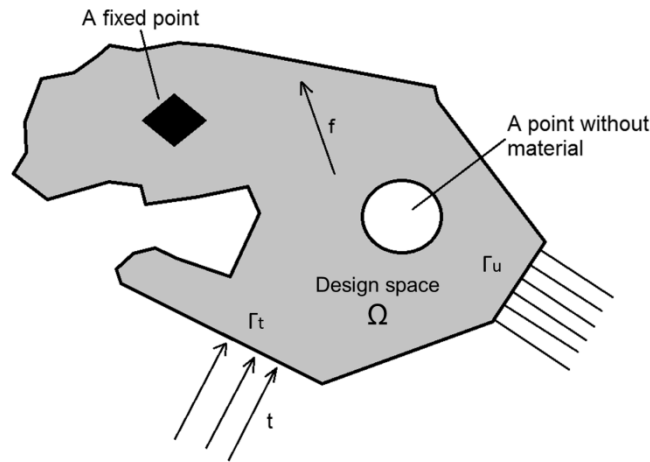


Figure 24. Generalized shape design problem in two-dimensional space for finding optimal material distribution.

$$a(u, v) = \int_{\Omega} E_{ijkl}(x) \varepsilon_{ij}(u) \varepsilon_{kl}(v) d\Omega$$

Equation 1. Internal virtual work of an elastic body at equilibrium u for virtual displacement v .

Where ε is linearized strain to direction u and v over the whole design space Ω . Strain has a form $\varepsilon_{ij}(u) = \frac{1}{2} \left(\frac{\partial u_i}{\partial x_j} + \frac{\partial u_j}{\partial x_i} \right)$, load in linear form $l(u) = \int_{\Omega} f u \, d\Omega + \int_{\Gamma_T} t u \, ds$ and the minimum compliance (maximum global stiffness) problem takes the form:

$$\begin{aligned} & \min l(u), \quad u \in U, E \text{ and} \\ & \text{s.t.: } a_E(u, v) = l(v), \text{ for all } v \in U, E \in E_{ad} \end{aligned}$$

Equation 2. Minimum compliance for global stiffness problem

This is a weak form of equilibrium with U representing displacement fields, f are body forces and t is boundary transactions $\Gamma_T \subset \Gamma \equiv \partial\Omega$ of the boundary. E_{ad} is the group of stiffness sensors in the design problem. This E_{ad} can for example hold all the stiffness sensors having material values in Ω_{mat} and zero values elsewhere, where limiting factor is represented with $\int_{\Omega_{mat}} 1 \, d\Omega \leq V$.

Typically solving the Equation 2 is done by finite elements approach. The problem is discretized by using finite elements (FE) into single rigid FE mesh. Then from Equation 2 the displacement u and the stiffness E become [44]:

$$\begin{aligned} & \min f^T u \parallel u, E_e \\ & \text{s.t.: } K(E_e)u = f, E \in E_{ad} \end{aligned}$$

Equation 3. FE approximation of the optimization problem.

$$KU = F$$

Equation 4. Optimization problem in global form

The optimization problem (Equation 3) can be simplified into global form (Equation 4) by summing up $K = \sum_{e=1}^N K_e(E_e)$ all the single elements. Equation is the same type as a typical FE problem [45] ($AU = F$). Global form of optimization problem states that stiffness (K) multiplied with displacement (U) equals forces (F). The problem in discretised matrix form with FE approximations is solvable by computation methods. An example about how the FE calculation for simple thrust element is done can be read from Appendix I – Finite Element Analysis (FEA).

Computers can undertake matrix operations efficiently. However, the matrix quantity becomes quickly a factor and the computation time increases. It has been one of the limiting factories in FEA and topology optimization. In a simple 2D 10x10 node mesh with 3 degree of freedom (DOF) there is a 300x300 stiffness matrix. When scaling the problem into 100 x 100 mesh, the stiffness matrix size becomes 30000x30000. A 3D problem 10x10x10 mesh with 6 DOF has a stiffness matrix size of 6000x6000x6000. The matrix size is cut slightly by applying

boundary forces, but overall the scale of the problem stays. In 2017, 1 million computer hours was used by Aage et al. [46] to calculate a half wing of boeing 777 consisting from 1.1 billion voxels with voxel size corresponding to 0.8 cm feature size showing that with more power it is possible to calculate smaller structures in larger scale.

The FE approximation gives resolution that can be thought as 2D pixels or 3D voxels, for the optimization. Material is distributed into design space Ω with volume constraint V . Then the stiffness tensor comes into form [44]:

$$E_{ijkl} = 1_{\Omega^{mat}} E_{ijkl}^0, 1_{\Omega^{mat}} = \begin{cases} 1 & \text{if } x \in \Omega^{mat} \\ 0 & \text{if } x \in \Omega \setminus \Omega^{mat} \end{cases}$$

$$\int_{\Omega} 1_{\Omega^{mat}} d\Omega = Vol(\Omega^{mat}) \leq V$$

Equation 5. Stiffness tensor with distributed material.

Solid isotropic material is spread out the design space. In this material the stiffness matrix becomes a variable where it depends on the density of the deposited material. A penalization factor is applied for homogeneous density to guide the design 1/0 or black and white. [44]

$$E_{ijkl}(x) = \rho(x)^p E_{ijkl}^0, p > 1$$

$$\int_{\Omega} \rho(x) d\Omega \leq V; 0 \leq \rho \leq 1, x \in \Omega$$

Equation 6. SIMP function

Density $\rho(x)$ is a design function that varies between 1 and 0. Material properties are given in stiffness tensor E_{ijkl} to the isotropic material. A penalization factor p guides the intermediate densities to gain 0/1 design. The higher the penalization factor p is, the higher the penalization. Penalization factor is calculated by Equation 7 from material values. Poisons ratio (ν^0) of 1/3 that corresponds to most of the metals is gained with penalization factor $p = 3$. [44]

$$p \geq \max \left\{ \frac{2}{1 - \nu^0}, \frac{4}{1 + \nu^0} \right\} (2D)$$

$$p \geq \max \left\{ 15 \frac{1 - \nu^0}{7 - 5\nu^0}, \frac{3}{2} \frac{1 - \nu^0}{1 - 2\nu^0} \right\} (3D)$$

Equation 7. Penalization factor equations.

The continuity in the material from Equation 2 and the SIMP problem from Equation 6 are written open with lower boundary condition ρ_{\min} . A lower boundary condition is applied to the hole material, because calculation singularity

will occur from pure zero values in matrix calculations. The density ρ_{\min} for void has a value of 10^{-3} or smaller.

$$\begin{aligned} & \min l(u), \quad u \in U, \rho \\ & \text{s.t.: } a_E(u, v) = l(v), \text{ for all } v \in U, \\ & E_{ijkl}(x) = \rho(x)^p E_{ijkl}^0 \\ & \int_{\Omega} \rho(x) d\Omega \leq V; 0 \leq \rho_{\min} \leq 1 \end{aligned}$$

Figure 25. Compliance problem in SIMP interpolation.

Sensitivity analysis starts when the compliance problem is joined with the method of Lagrange multipliers $[\Lambda, \lambda^+(x), \lambda^-(x)]$. A method that Giuseppe Luigi Lagrange, a mathematician born in Turin and Università degli Studi di Torino graduate, formulated. Lagrange method is a strategy to find local maxima and minima to a function with equality constraints.

$$\begin{aligned} \mathcal{L} = & l(u) - \{a_E(u, \bar{u}) - l(\bar{u})\} + \Lambda \left(\int_{\Omega} \rho(x) d\Omega - V \right) + \\ & \int_{\Omega} \lambda^+(x) (\rho(x) - 1) d\Omega + \int_{\Omega} \lambda^-(x) (\rho_{\min} - \rho(x)) d\Omega \end{aligned}$$

Equation 8. Lagrangian equation from the SIMP compliance problem.

Lagrange multiplier for displacement field \bar{u} is the change happening in the displacement fields. When the displacement fields are unique the variation in displacement field gives $\bar{u} = u$. Then the density condition becomes:

$$\frac{\partial E_{ijkl}}{\partial \rho} \varepsilon_{ij}(u) \varepsilon_{ijkl}(u) = \Lambda + \lambda^+ - \lambda^-$$

with boundary conditions for adding and removing material

$$\begin{cases} \lambda^- \geq 0 \\ \lambda^+ \geq 0 \\ \lambda^-(\rho_{\min} - \rho(x)) = 0 \\ \lambda^+(\rho(x) - 1) = 0 \end{cases}$$

And boundary conditions for intermediate densities ($\rho_{\min} < \rho < 1$).

$$p\rho(x)^{p-1} E_{ijkl}^0 \varepsilon_{ij}(u) \varepsilon_{kl}(u) = \Lambda$$

Design update takes information from strain energies. Strain energy is constant during the intermediate densities and the scheme is similar to fully stressed design condition. Where stress is high, there is too low stiffness E and density. An update policy is applied after iteration K when knowing the stress:

$$\rho_{K+1} = \begin{cases} \max\{(1 - \zeta)\rho_K, \rho_{min}\}, & \text{if } \rho_K B_K^\eta \leq \max\{(1 - \zeta)\rho_K, \rho_{min}\} \\ \min\{(1 + \zeta)\rho_K, 1\}, & \text{if } \rho_K B_K^\eta \geq \min\{(1 + \zeta)\rho_K, 1\} \\ \rho_K B_K^\eta, & \text{otherwise} \end{cases}$$

Equation 9. Stiffness and density design update equations.

ρ_K is the density value at iteration number K and B_K is the strain energy for intermediate densities at iteration K .

$$B_K = \Lambda_K^{-1} p \rho(x)^{p-1} E_{ijkl}^0 \varepsilon_{ij}(u_K) \varepsilon_{kl}(u_K)$$

Equation 10. strain energy for intermediate densities at iteration K .

Equation 9 gives out design update for stiffness. At the point where specific strain energy ($B_K > 1$) is larger than Λ , the optimizer adds material into the design. When specific strain energy ($B_K < 1$) is smaller than Λ , the material is removed from the area. A local optimum is reached if $B_K = 1$. These three cases are monitored for all the points with Λ and checked if the boundary conditions are fulfilled. Both η and ζ are parameters of move limit in iteration step. Volume is decreasing and increasing in FE discretized intervals that allows the calculation of individual Lagrange multiplier Λ values for nodal points. [44]

After the sensitivity analysis and design update, the new design is sent back to the start for new sensitivity analysis and new design update until the model has converged. If the model has problems of converging in the beginning, the design update might not help. A robust start guess for optimization followed by design update will provide good design after every iteration and will lead to model converging. A bad design update will eventually lead the model failing.

Problems in SIMP are checkerboard, greyscale, size of mesh. Checkerboard problem is based on the direct implication of material distribution method from the placement in finite element method. It is created in the FE as the material is distributed along the finite elements in a periodic fashion creating checkerboard pattern where the material is varying between solid and void Figure 26. Checkerboard. This problem is a feature of the finite element approximation and numerical modelling, where stiffness is over estimated in the void-solid pattern. [44]

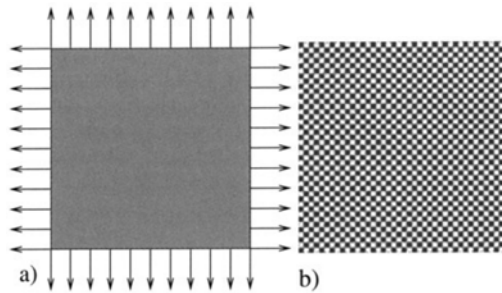


Figure 26. Checkerboard problem visualized, a) the design space, b) checkerboard [44]

In topology optimization 1/0 black and white design is wanted. However, the material distribution has all values between 0 and 1. These middle values are penalized into black and white values, but it is not always possible and some greyscale is retained. The problem of intermediate densities is in the problem of manufacturing these and in the modelling these densities affect in calculations.

The mesh size allows the creation of different design as larger mesh allows the introduction of more holes or smaller support elements without changing the structural volume. This is illustrated in Figure 27. Effect of mesh refinement into design [44] Figure 27 where refining of mesh has created more refined microstructure.

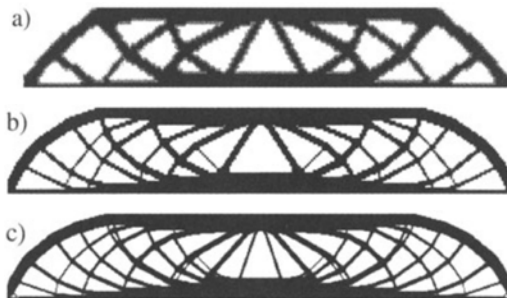


Figure 27. Effect of mesh refinement into design [44]

2.4.3. Level Set Method

Level Set Method (LSM) is an alternative topology optimization method where the boundary of the design space is defined by an equation [47]. Whereas the boundary condition for SIMP is consists of density between 0 and 1, the LSM has a clear 0/1 boundary given by trackable equation called the level set function (LSF). The LSF is a form of a Heaviside function (Equation 11). The level set function is negative inside of the design space Ω , zero at the boundary and positive outside of the design space. From the value and sign of the LSF it is possible to determinate exactly where is the design boundary. This is beneficial for the method as there are no grey intermediate densities as in SIMP method. Figure 28 gives graphical representations of LSF for circle stated in Equation 11. [47]

$$LSF \varphi(x) = \begin{cases} \Omega^-, & \text{if } \varphi(x) < 0 \\ \partial\Omega, & \text{if } \varphi(x) = 0 \\ \Omega^+, & \text{if } \varphi(x) > 0 \end{cases}$$

Equation 11. Level set function equation.

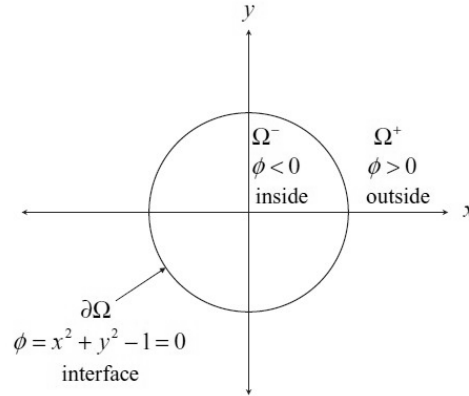


Figure 28. Representation of a level set curve.

The LSF is giving the boundary to the design. These boundaries are tracked in know nodal spots what are then translated into implicit functions. The known values of the LSF depends on the coordinate system and grid discretization. Higher meshing creates well defined boundary as between the nodes, the value of LSF is approximated by implicit functions. The finer the mesh is, the better are the details on a surface. Grid discretization is based on Cartesian coordinate system and similarly, as in the case of SIMP, the discretization is made with the same mesh that is given by FE-discretization. [47]

The LSF values of nodal points can be calculated in the whole grid. However, this method takes time and resources. The nodal values near LSF boundary and the existing boundary points are important. The rest of the values are not necessary to know as the values are either -1 or 1 depending on the normal direction from the level set surface. A band around the known LSF values are monitored for changes and regularly updated. This removes the necessary of counting all the nodal point values every time when doing a new iteration. The band is checked regularly for the surface evolution every few iterations depending on the sensitivity values moving the boundary. The FE mesh defines the smallest details and changes in the values. [47]

The curvature of the surface is defined as the divergence of the surface normal (Equation 12). So that for $\kappa > 0$ the surface is convex and for $\kappa < 0$ the surface is concave, whereas $\kappa = 0$ is a plane.

$$\kappa = \nabla * \bar{N} = \frac{\partial n_1}{\partial x} + \frac{\partial n_2}{\partial y} + \frac{\partial n_3}{\partial z}$$

Equation 12. The mean curvature of the LSF interface.

For complex shapes modelled with LSF an implicit function called a signed distance function (Equation 13) is defined. This function defines the closest distance of the interface to a spot. Defining signed distance function with Equation 13 will lead in some cases to a kink, where 2 points can have same values. Mathematically this is a problem but the Cartesian coordinate approximation smears out the continuity of the function and the kink will be rounded out. [47]

$$d(\bar{x}) = \min(|\bar{x} - \bar{x}_1|), \text{ for all } \bar{x}_1 \in \Omega$$

Equation 13. Signed distance function.

Optimizing problem for structural application can be started in the same way as in SIMP via linearly elastic structure and virtual work. The optimization problem takes the form of objective function $J(u)$:

$$\begin{aligned} \min J(u) &= \int_{\Omega} F(u) d\Omega \\ \text{Subject to } \int_{\Omega} E_{ijkl} \varepsilon_{ij}(u) \varepsilon_{kl}(v) d\Omega &= \int_{\Omega} p v d\Omega + \int_{\partial D_t} \tau v dS \\ u|_{\partial D_u} &= u_0, \forall v, u \in U, \\ \int_D d\Omega &\leq V_{max} \end{aligned}$$

Equation 14. General LSM optimization problem statement.

Where u, v are the displacement fields in space U , E_{ijkl} is the elastic tensor, ε_{ij} and ε_{kl} are strain tensors, p the body forces, τ the boundary tractions applied on the part ∂D_t of the boundary ∂D and u_0 predefined displacement in the body. The optimization is applied to the physical or geometric area defined by function F .

To solve the optimization problem level set function, that is the shape of Heaviside function, showing the directions of the shape is added. Adding the LSF (Equation 11) for the Equation 14, the level set model can be formulated [48]:

$$\begin{aligned} \min J(u, \phi) &= \int_D F(u) H(\phi) d\Omega \\ \text{Subject to} \\ \int_D E_{ijkl} \varepsilon_{ij}(u) \varepsilon_{kl}(v) H(\phi) d\Omega &= \int_D p v H(\phi) d\Omega + \int_D \tau v \delta(\phi) |\nabla \phi| d\Omega \end{aligned}$$

$$u|_{\partial D_u} = u_0, \forall v, u \in U,$$

$$\int_D H(\phi) d\Omega \leq V_{max}$$

Equation 15. Level set method optimization problem.

$\delta(\phi)$ is a dirac delta function.

The difference between SIMP (Equation 6) and LSM (Equation 15) is that SIMP has a continuous density of the material as LSM lies on Heaviside function to define the border.

2.4.4. Other Topology Optimization Algorithms

The most common variations for topology optimization are Evolutionary Structural Optimization (ESO) and a derivate of it called Bi-directional Evolutionary Structural Optimization (BESO). The methods are based on a concept where the inactive material is systematically removed from the structure and the residual shape evolves toward an optimum. This is a hard kill of element by determining if the stress is low enough for the element to be removed. The original ESO could only remove elements and it did not always create optimum as it couldn't reverse the optimization process by adding elements later. Bi-directional ESO was created to remove and add elements improving the original ESO. Adding elements allows the algorithm to pass local optimums to travel towards more global optimum. [49]

Fully stressed design topology optimization method is based on the design being fully stressed at least in one of the load condition at all of the time. Extra mass is removed until the stressed condition is reached. [50]

2.4.5. Commercial Software

Topology optimization is more and more offered in commercial software. The optimization is added into finite element solver packet as an extra plugin as was the case with Abaqus in 2015. In 2017, there are software from what are designed for toptopt and AM in mind as we can see in case of Netfabb. FEA manufacturers protect their software and the add-on is usually as it is or a black box. Detailed information of algorithm implications is difficult to find out. However, results show when doing more investigation that the algorithm is often SIMP based or a derivate of SIMP as is the case with Altairs Inspire what is based on Optistructs optimization codes [51].

Topology optimization algorithms are possible to be run with commercial software without a packet. This was shown by Zuo et al. [52] [29] with BESO topology optimization script written in python code for use in Abaqus. The python script is read by Abaqus and then loads and constraints are given as inputs. With

script infusion method it is possible to utilize commercial solver (e.g. Abaqus) instead of writing own visual environment and finite element analysis script.

The latest developments have brought different software packages in the market that are directed towards additive manufacturing. These are more design driven software in order to give access to and only a few AM constraints are taken into account. The software packages include Netfabb Ultimate Simulation [53] by Autodesk, Virfac Additive Manufacturing [54] by GeonX, Amphyon [55] by Additive Works, Simufact Additive [56] by MSC, Simulia [57] by Dassault Systems.

These software's provide a new approach for metal additive manufacturing by offering topology optimization and process based considerations into the design phase. It is not uncommon to be able to count the heat effect when building layer by layer and have an estimate of stresses from the model. The less stressed areas can be converted for lattice structures or removed from the model by topology optimization. The drawback is that these software have been developed from casting and welding simulations that makes these less suitable for plastics use. Another approach is needed for anisotropic materials and composites.

2.4.6. Using Topology Optimization

Topology optimization algorithms are useful for many applications where computer-aided design can be used. However, topt algorithms are computer programs that will do whatever those are asked to do. Any design choice or question not specified by the user will lead to interesting results. What does this mean in real life? Designs have multiple minimums and the achieved minimum is not always the global minimum, however, it is not possible to know if the minimum is a local one or global one. Depending on the algorithm and the previous iterations the design can go differently in other direction as wanted. For example, a zero solution is a local minimum as well but not the wanted one. A good practise is to compare the simulation results into original design and how it compares. From the comparison it is possible to tune the parameters into safer direction.

There is always some variation between simulation runs and the robustness of the algorithm is an indication that it can produce similar results between every simulation. In simulation, faults from a previous iteration are carried into succeeding design space leading to more faults or the design to branch out from a single solution. Therefore, when the simulation fails it is usually the reason for the wrong design update and the following iterations building on top of a weak foundation. This weak foundation is unfortunately true also in the AM manufacture. Robustness of the algorithm is in the ability to have results and iterations in the topt simulation that will produce feasible results. All results are good to be tested and verified in FEA after the initial design. Any design changes can be made to make the design more accurately resemble the wanted properties

by the designer. In every result, the designer has the final decision to make: what is feasible design and what is not.

The toptop algorithms go rigorous testing before those are used in real applications. The benchmark tests are familiar to all of us: cantilever, MBB beam, bridge. This reasoning comes from conventional thinking of engineers where the method has to be proven to give reliable solutions to a known problem. These benchmark tests have been proven analytically earlier and agreed on of the global optimality, since it is not possible to know if the point is a global optimum as it is not possible to count all the points to compare. The benchmark tests are important also because not all the optimization algorithms work in all the problems.

Topology optimization often produces structures that are not being able to manufacture. Therefore, specific compromises have to be made, depending on the manufacture technique. These compromises are for example sizing constraints, casting directions, symmetry and patterns. Realizing topology optimized design is time-consuming with conventional methods. For example, Brembo has developed brake calipers for Moto GP and Motorsports [58]. A Moto GP brake caliber (Figure 29) is topology optimized and then milled from a single block of metal. Single component allows high mechanical properties, but the time of machining will limit the complexity of the part.

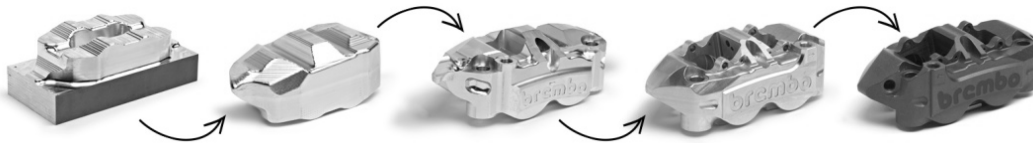


Figure 29. Topology optimized and milled Brembo GP4 RX brake caliper. [59]

In simple shapes as brake disks, topology optimization has been used more often. A study with Altair Optistuct in UCSD [60] revealed that Shimano's bicycle brake disk is similar to simulation results with Altair's SIMP topology optimization [51]. The disk is a simple 2D shape that can be easily machined or stamped and it shows to us that topology optimization is around.

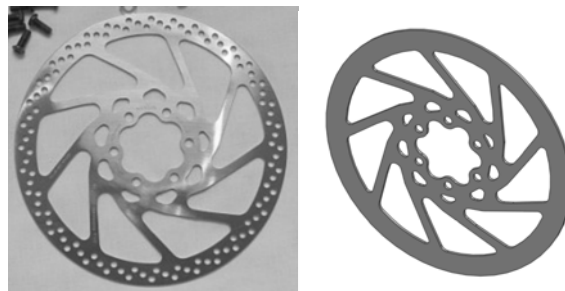


Figure 30. Brake disk of a bicycle. Left Shimano commercial disk and right simulated result from Altair OptiStruct [60].

Casting has large design freedom and it can be compared with additive manufacturing. In casting, the pieces have to be able to remove from a die. Depending on the casting method the die can be broken (sand- and investment casting) or it cannot (permanent mold casting). In any case, a topology optimization can be used in cast items to redesign the existing component with CAD/CAE by removing extra material. Aircrafts are high value products with long usage life. Topology optimization can be implemented in many areas of an airplane like in design for airframe, layout of stiffeners, multi-component design and multi-fastener design [61]. New potential usages that are forecasted are in dynamic response design, shape preserving, smart structures and structural design. [61]

2.5. Process Driven Design

AM is as revolutionary for manufacture as the computer numerical controlled (CNC) machining was for machining. The design is manufactured layer by layer from a digital file. Instructions are translated by a computer rather than a human to create the final product, thus creating better automation and removing human error factor from the equation.

The layer-based, additive nature means that shapes can be manufactured without hard tooling that can be molds, dies, or fixtures. Geometries are built individually allowing customization per part. Fine patterns are possible to be manufactured and this allows to join multiple conventional parts into one single component. The time made to join these parts can save money via time and manufacturing costs. The new solid shapes can be more durable than the existing assemblies.

AM is not a single manufacturing method but a series of methods specifically tailored from an existing method for the computer environment. That is why it is possible to notice conventional manufacturing methods rebranded as additive manufacturing. For example, thermal spray has become direct energy depositing, welding has become as wire additive manufacturing and with polymers extrusion has gone from mold into freeform. Every AM and 3D printing method have its own manufacturing constraints which nominate the possible structures and design guidelines. Where it is claimed that all is possible with AM, the reality is that there are different build constraints.

2.5.1. Polymeric Materials

Polymers in 3D printing are either thermoplastics or thermosets. Thermosets are resins like in vat photopolymerization, where polymerization is activated with a light source. Various light sources can be used to cure the resin i.e. a laser, screen or light diffused through a lattice. The light cures monomers and makes them polymerize on the illuminated spot. This creates homogenous structure without

distinguished layering. The disadvantage is that thermosets need UV-curing after the build.

Thermoplastics are used more commonly in 3D printing as the polymers can be remolten without a penalty in degradation of the polymer properties. The common method that the 3D printing has become to symbolize is material extrusion where a thermoplastic wire is heated near the molten temperature of the thermoplastic and extruded from a nozzle. The polymeric mass solidifies when it is out from the nozzle. The plastic layers need to be solid enough to support the weight of the new layer and provide a bonding surface for the new layer. Otherwise, the new layer will sag and thermal shrinkage can be an issue. Both of these will affect the dimensions of the part.

Support structures for plastics are necessary during the build, when the previous layer cannot bear the load or it is built on overhang. The overhang creates a bridge that can lead to sagging material on the bottom layer. The support can be neglected in some cases like laser sintering, where the powder provides the reasonable support for the melt. Whereas dissolvable materials can be used as in material extrusion to remove extra material without harming the final part. A support structure can prevent curling but can also leave marks on the final part making it rough. In material extrusion one extrusion nozzle can be used specifically to extrude material that it is dissolvable for something that does not affect the base material. An example of this is ABS print with HIPS support structure that is then dissolved in limonene acid. Build with or without support structures that can be removed chemically is beneficial when creating structures where a worker or tool cannot easily reach.

Due to the minimizing usage of the material, the plastic parts are made hollow or made with an infill structure. The infill structure is a support structure inside of the part for material extrusion creating semi-hollow space that allows the outer shell looking as wanted. Because the parts are often visual and not meant for mechanical loading this can be done. The performance of the part depend on this infill [19] more than on the filled structure. For laser sintering where powder is used, this infill is made hollow with a cap to allow the excess unused powder to be removed from the cavity.

Feature size and accuracy depends on the material and printing method used. Features are walls, holes, embossing, engraving, text and tolerances. This depends on the build direction and process parameters used. As layers are stacked on top of each other the layer boundary becomes important. The layer boundary acts as partly molten and fused part where the mechanical properties are lower. As the layer thickness is fixed at the start of the build, it is not possible to build smaller details than the layer thickness in Z-axis. There also will be a staircase effect due to the layer wise structure. In xy-plane the dimensions are restricted by the accuracy of machine movements by a heat source or an extrusion head. It is important to know that one layer wall might not be able to carry the weight of

itself and therefore needs to be thicker. From this ideas the design rule of aspect ratio comes into play: don't build more taller than 8:1 ratio.

A solution for building parts that are symmetrical or have difficult sections is to divide those into sections and manufacture the sections separately. The accuracy of dimensions in the build is affected by the 3D printer build quality and the slicing software in use. Features like holes should be designed a little bit smaller than intended so drilling or boring a thread can be done to achieve the accuracy. [62]

The depositing path is important as it defines how the material is divided into the layer. The printing nozzle in 3DP is circular and this feature gives edges and corners a radius of the nozzle diameter into the build. Features that are small will be more rounded than the features that are large. This is the core reason alongside contracting material, while solidification for elephants foot for 3DP's first layers, where the straight portion curls up from the build platform. Small support structure with heated bed is usually used to remove this problem.

Build direction is crucial in plastic 3DP applications. There are many studies stating the difference of the mechanical properties in different directions. The scale of xy-plane vs z-axis direction is large and it can be over 50% of the yield strength. This and other properties are considered in Case study I about product design where topology optimization is used for designing the part. Process parameters through material properties are inserted to the optimizer to give an estimate of the breaking point of the part. In both SLS and material extrusion there was a difference between the directions. In SLS the difference was between 10 – 15 %, whereas with material extrusion the difference was larger. All directions (X, Y, Z) were different. Where X and Y directions varied in slight Z had its own constraints through the mechanical properties. More from this study is presented in the next chapter.

Creating layered structure from curved surfaces, the anisotropy of the part in layer-by-layer manufacturing is bound to reduce accuracy. The reduction happens when the slicer makes assumptions from the 3D shape into 2D slices. The machine accuracy affects through the thickness of the slice all the way to the feature size possible. Figure 31 shows this for arch structures in two different orientations. When the model is sliced into x-direction, the middle of the part becomes affected by the layers. In the other hand, slicing for the z-direction the dimensional distortion happens on the sides of the model. A larger feature will not be affected by this as much as a fine and small feature.

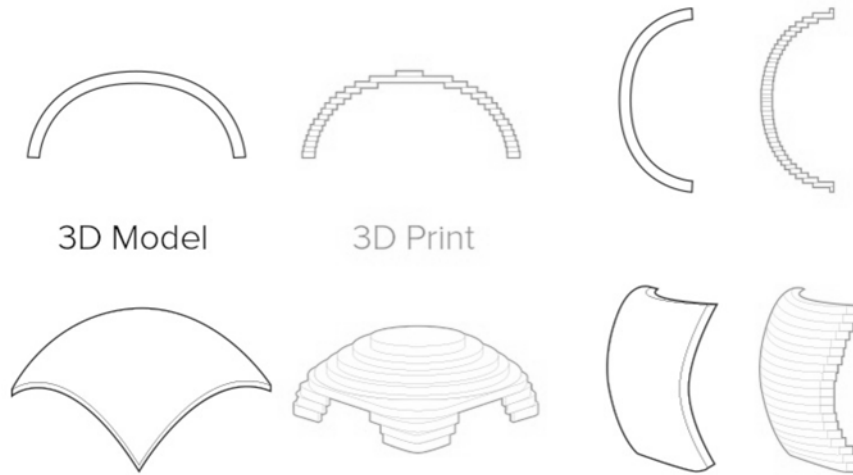
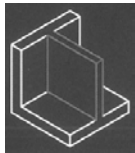
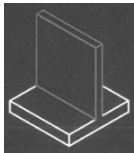
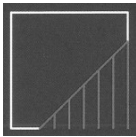
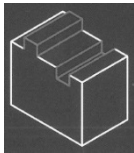
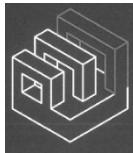
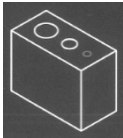
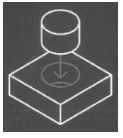
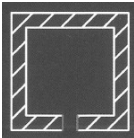
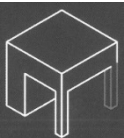
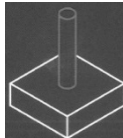
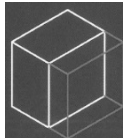


Figure 31. 3D model simplified into layered structure.

Design rules for different geometrical features are compiled by 3D Hubs [63] with their knowledge base and distributed in October 2017 TCT magazine. These design guidelines with dimensions are condensed into Table 4.

Table 4. Design rules for polymeric 3D printing materials [63]

	Supported walls	Unsupported walls	Support & overhang	Embossed & engraved details	Horizontal bridges
	Walls that are connected to the rest of the print on at least two sides	Unsupported walls are connected to the rest of the print on less than two sides	The Maximum angle a wall can be printed at without requiring support	Features on the model that are raised or recessed below the model surface	The span a technology can print without the need for support
					
Material extrusion	0.8 mm	0.8 mm	45 degree	0.6 mm wide & 2 mm high	10 mm
Vat photopolymerization	0.5 mm	1 mm	Support always	0.4 mm wide & high	NA
Laser sintering	0.7 mm	NA	NA	1 mm wide & high	NA
Material jetting	1 mm	1 mm	Support always	0.5 mm wide & high	NA
Binder jetting	2 mm	3 mm	NA	0.5 mm wide & high	Na
LPBF	0.4 mm	0.5 mm	Support always	0.1 mm wide & high	2 mm

	Holes	Connecting / moving parts	Escape holes	Minimum features	Pin diameter	Tolerance
	The minimum diameter a technology can successfully print a hole	The recommended clearance between two moving or connecting parts	The minimum diameter of escape holes to allow the removal of build material	The recommended minimum size of a feature to ensure it will not fail to print	The minimum diameter a pin can be printed	The expected tolerance of specific technology
						
Material extrusion	ϕ 2 mm	0.5 mm	NA	2 mm	3mm	\pm 0.5 mm
Vat photopolymerization	ϕ 0.5 mm	0.5 mm	4 mm	0.2 mm	0.5 mm	\pm 0.15 mm
Laser sintering	ϕ 1.5 mm	0.3 mm for moving parts & 0.1 mm for connecting parts	5 mm	0.8 mm	0.8 mm	\pm 0.3 mm
Material jetting	ϕ 0.5 mm	0.2 mm	NA	0.5 mm	0.5 mm	\pm 0.1 mm
Binder jetting	ϕ 1.5 mm	NA	5 mm	2 mm	2 mm	\pm 0.2 mm metal & \pm 0.3 mm sand
LPBF	ϕ 1.5 mm	NA	5 mm	0.6 mm	1 mm	\pm 0.1 mm

2.5.2. Metallic Materials

Metallic materials behave differently than plastics when manufactured with AM, as expected. This is due to the properties of metals i.e. high melting temperatures. There is no definite melting temperature of ABS and the glass transition temperature is 108°C while pure aluminium has a clear melting temperature of 660 °C and a glass transition temperature is not considered.

In metal AM, a molten layer is deposited on another layer that partly melts the previous layer joining these together. It is important to support the new layer structure when the melt solidifies. Molten metal occupies larger space in liquid form than in solid. The physics of the liquid to solid transition is material and composition dependent. Search for the correct model for individual materials is in the metallurgy's core as known from different material compositions and cooling rates. The solidifying metal will create residual stresses in the structure. The melt cannot be supported by the powder or thin air as the liquid has low viscosity and it flows well. The continuous re-melting and re-heating of the material create rapid solidification and usually a very fine microstructure [64]. There are exceptions to this is e.g. Ti6Al4V where one solidification direction is dominant and it creates a columnar structure in EBPBF [65] method.

Material cooling is problematic with metals since a part can be already several hundred degrees lower than the top that is still being formed. The support structures will dissipate the heat to the environment more efficiently than surrounding materials preventing the part to be burned. The support material keeps the part anchored into its form before the residual stresses inside of the part can be released with annealing when building with low temperatures (LPBF), but offers less of a threat in high temperatures (EBPBF). Anchoring the part is important as residual stresses are formed inside of the material. This residual stress formation is reduced by building platform and chamber heating. However, it is possible that a weak support structure will crack under pressure and bounce out the part from the powder bed spreading material over the chamber creating a hole and lack of powder on the part efficiently increasing heat input on the next layers. This overheated position is called a hot spot in process monitoring and it indicates a possible failure point. The flown excess material can create clumps of powder on elsewhere in the powder bed decreasing heat input on the spot where heat source needs to fuse it. This low heat input position is called a cold spot and can mean e.g. porosity via lack of fusion. Heat dissipation comes to play when large overhangs and unsupported parts are being built. The material on the spot where heat cannot escape has large heat input causes the material to burn and curl. Excess heat input and curling might stop the build process as well as leading undesired effects on the surface and increased porosity near the overheated surface.

Design guidelines have been investigated by Thomas [66], Atzeni et al. [67], Calignano [68] among many others. In 2017 design guideline standard by ASTM

[69] was published. In these articles, the importance of the support structures and self-supporting structures are considered. When a structure becomes from supported to self-supporting is material dependent as seen from Calignano's [68] work with titanium and aluminium alloys. The threshold with aluminium is lower than with titanium. This is due to higher dross formation in aluminum alloy, allowing builds up to 30-degrees to be self-supporting in sacrifice of the dimensional accuracy. The AM industry has agreed to call slopes with 45-degree angle or more a self-supporting structure. J. Kranz et al. [70] have collected larger pool of design suggestions for different shapes with Ti6Al4V material for LPBF manufacturing. Further, these guidelines have been collected in an LPBF [71] book about the process, design, and applications.

The self-supporting structures have a disadvantage for overhangs as this need to be designed after the build direction of the part has been chosen. A round tube manufactured on less than 45-degree angle needs to be redesigned as elliptic or with a cone to reduce overhang by slowly joining the surfaces together. This can be achieved by making the cross section to resemble a teardrop or elliptical shape. Internal cavities are the second area of concern where a process driven design is needed in order to make the part with correct arching and opening from where the extra powder can be removed. Needs of the cavities and shapes lead to selecting a build direction, that corresponds to the fundamental needs. The build direction of the part will lead anisotropy in the microstructure and if no homogenizing heat treatments are done for the structure, there will be a z-direction with lower mechanical properties. The anisotropy is due to orienting the microstructure by the solidifying front. The build direction also is used to minimize the overhangs before the redesign for manufacture. During recoating some contact is bound to happen between a recoating blade spreading a new powder layer on top of the build as melt pool will not solidify in a flat manner. The possible contact area is good to be minimized by tilting the shape perpendicular to the recoating direction. Recoating also has an effect on parts in different positions of the building platform. In an unlucky case platform area further from a powder dispenser might not get enough powder spread on top for a new layer. Laser spot gets distorted a bit when deflected from the lens and the shape in middle and corner are not the same. As the build volume is small, there is only minor effect on this.

Minor shapes that are possible to manufacture are explored in this thesis in case study II through the design of holes. Holes are important as they show the accuracy of features. In small holes, it was noticed that the scan direction was visible with the direction of a melt pool as well as the larger heat input in the hole area added higher roughness for the hole. This gives an oversight of an effect from layers influence into surface roughness. When enlarging the holes, the dimensional accuracy became more accurate. This might also be affected by the pixelification of the hole into square blocks as shown in Figure 32. The larger the hole, the smaller is the effect of these square blocks.

Part orientation also has an effect on the surface roughness of the part and it was investigated in the Case study II with tubes for internal structures. Different angles and materials were fabricated and tested to get a corresponding understanding of the physics behind the effect. The machine divides manufacturing parameters into four different section that it changes depending on need. For overhang and down facing structures down skin is used. It is to control the heat input and only melt the correct amount of material as there will be no support from below. On parts where there is nothing on the top upskin parameters are used. Sides where there is no material outside, contour parameters are used. In the bulk material processing core parameters are used. The machine divides these accordingly to the 2D slice data for every part as shown in Figure 32. The parameters will affect surface roughness. In the case study, the difference of build angle in tubes was characterized and 3 different zones were found. This derives from build angle relation with powder size and layer thickness. As the build angle increases there becomes less space for the powder particle to be able to attach the surface permanently. At 45 degrees, staircase effect is visible but still top and bottom surfaces are different. However, going to 60 degrees build both top and bottom surfaces are similar and no more increase in surface roughness was found after that between the top and bottom surfaces. Orienting part with a small angle and the minimum contact surface as possible will also increase surface quality.

Surface quality is a key factor as it is visible to the inspector. When part height in the z-axis is equal to multiple of layer thickness, the best match of tolerances is gain. Adding extra energy to the surface creates better surface finishing. This can be done with second exposure time. However, extra heat input will increase the porosity on the surface. Creating holes that are a bit smaller than near net shape is good as layer structure will deform the hole depending on the layer size in comparison to the hole as seen in Figure 32. Smaller hole diameter allows the hole to be drilled afterward to gain the dimensional accuracy.

Large simultaneous melt pools create large heated area that solidify quickly being able to pull out a part from the support structure. When joining two areas together these will create also forces to each other leading to small gaps on the surface. Whenever it is possible to lower the melt pool area by orientation or design, it should be done in order to avoid lines by moving of parts.

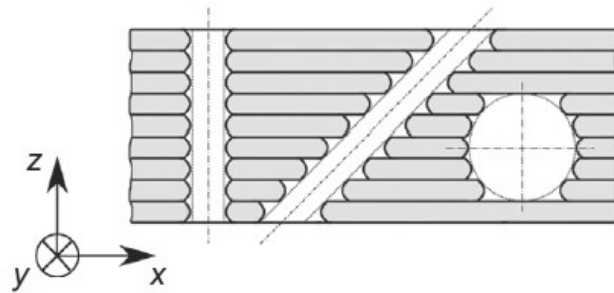


Figure 32. Layers effect by staircases on surface roughness [71]

Minimum part feature size is dependent on the method used to melt the part. The heat source e.g. laser spot will limit the wall thickness as well as the walls capacity to support itself. A good estimation from the literature is that the minimum wall thickness is 3x the laser spot size. This cannot be the case in always as melt pool, the height of the wall and the recoating directions influence the build. Tall and thin sections might need extra support so as not to fail under the weight of itself. Sharp and small corners are also good to round up as the heat source doesn't have direct access to sharp corners. These will be overheated as the heat input in small hatches is higher than in long ones. [71]

Raw part for manufacture is good to manufacture from original net shape part to adapt the needs of metal AM. In the raw part, additional material is added to be machined away after the build to reach the desired tolerances. A raw part can be machined to net shape on build plate when there is enough space near it.

Including AM constraints in topology optimization is a popular research topic. The latest research in topology optimization has been involving considering adding the overhang constraints into topology optimization algorithms [72] [73] [74] to make the topology optimized part to be buildable with minimum support structures. In these algorithms, a 45-degree rule is made and given for topology optimization algorithm for the new layers. The rule works by limiting the optimizer to build always on a solid support and try to minimize overhangs. Similarly to grey material penalization into 0/1 optimum, the optimizer is asked to penalize angles smaller than 45 degrees. This new design constraint has the downside of modifying the topology optimized structure into another optimum. The original part driven optimum might be closer to the functional optimum, whereas the new optimum the process driven optimum. It has to be decided by the operator: What is better: to optimize for manufacturing or for part functionality?

Chapter 3

3. Case Studies

The chapter consists of different studies in field of design and manufacture. The first case study is a dive into a product driven design where only part related information is considered. Whatever the shape will be or how difficult it would be to manufacture these constraints are not considered. A classic example of cantilever is used as an example for topology optimization algorithm.

The second case study is applying the topology optimization knowledge into a flexural test specimen and test the simulated structure in manufactured state with three point bend equipment. This works as a bridge between the simulated reality and manufactured reality.

The third and the last case study considers different process constraints and how these constraints can be utilized in wider scope and final parts in metal additive manufacturing. Shape and designs are manufactured and characterized to gain further knowledge to fabricate industrial parts.

3.1. Case Study I: Product driven design

3.1.1. 2D Comparison: SIMP and LSM Algorithms

Simulation tools in use are Matlab 2016 and Inspire 2016. Matlab (Matrix Laboratory) is a numerical computing environment developed at first in the 1970's to teach calculations with a computer without having to learn Fortran-programming language by means of which the codes were written. Since the commercialization of Matlab, it has been developed further by MathWorks and evolved into multi-paradigm numerical computing environment what can be used scripts from other computer languages e.g. Fortran, C and Python. A topology optimization code was studied under Matlab environment for this case study.

The cantilever problem (Figure 33) is a well-known test problem in topology optimization. The simple shape allows to test and compare different algorithms on the same problem, because large and complex problems are difficult to compare.

Standard cantilever has been solved mathematically in statics and it is taught to students. All forces in the structure cancel out and the stresses inside of the material can be calculated when support structure is written open. This was the case in rigid cantilever optimization as Venkayya [75] explains for struts and optimization by for different metallic materials. An alternative solution for the optimization can be thought with Michell structures described by Chan [76]. In Michell structures there is an equilibrium of virtual forces and by finding these points of equilibrium it is possible to create more accurate stress concentration cantilevers as in rigid model. The Michell models cantilevers has been applied into aerospace design for long as Hemp et al. [77] describes in their aeronautics paper from 1965.

Both algorithms are simulated with similar parameters consisting of mesh 150x50 ($x=150$, $y=50$). Optimization restrictions are volume fraction 60 % and compliance (invert of stiffness).

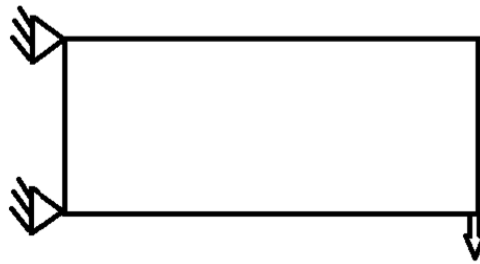


Figure 33. Cantilever, a constrained beam from one side and a weight on the other side.

SIMP model of cantilever starts with a constant volume of 60%. The algorithm distributes the density to the whole design space. From that the calculation for better distribution of material towards optimum starts. The design emerges slowly (Figure 34) during iterations and new design updates. More material gets penalized into void as the frame takes shape. Finally a design has come out with less grey intermediate densities. For in depth detailed information how the used Matlab SIMP 99 code works and the source code, it can be read from Sigmund's article "A 99 Topology Optimization Code for Matlab" [78].

LSM model of cantilever starts with a full volume of 100% from where the optimizer shrinks towards the volume constraint. After 25 cycles a hole is introduced into the design. LSM has a problem of creating holes as the LSF well defines the shape borders. For in depth detailed information how the used Matlab LSM 99 code works and the source code, it can be read from Challi's article "A discrete level-set topology optimization code written in Matlab" [79].

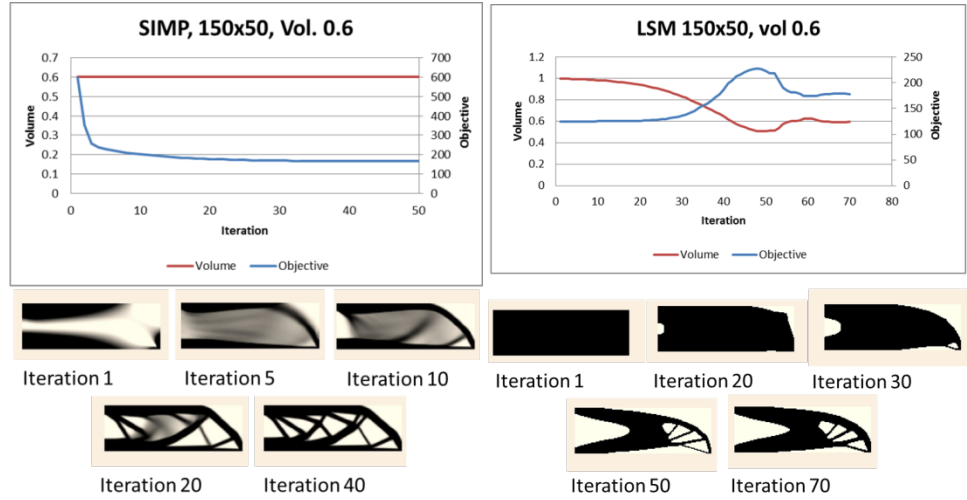


Figure 34. 150x50 mesh cantilever optimized: left Matlab SIMP [78] algorithm, right Matlab LSM [79] algorithm.

The simulation results for SIMP look similar with the shape as can be expected after Sigmunds paper [78] and Bensoes [44] book. However, differences between the methods are interesting to notice and what comes firstly in mind is time to process the calculations. LSM is taking a bit more time to converge into a solution in comparison with SIMP method. Also LSM has a problem with hole generation and that is visible in the first 30 iterations when the design space is forming into the shape of the part without holes. When the LSM algorithm is creating the holes it is possible to notice how objective function value becomes higher an volume fraction oscillates near the objective value. The stability of LSF is a drawback for the hole creation forcing the structure to create more Michell style structure. Whereas, in SIMP the topology optimizations shape can freely be formed and penalization is removing gray areas into 0/1 design. The shape and complexity of the part is partly defined with the size of the mesh, what defines the minimum member to be able to hold stresses. The different designs are results of two approaches into optimization leading to two varying optimums.

3.1.2. 3D Comparison: SIMP and LSM Algorithms

The toptop equation of the models gets more complex when the third dimension is added. Instead of three degrees of freedom, those increase to six and nodal points for one simple square shell goes from four to eight. In large meshes that are preferred for detailed simulations, things get complicated. Debugging and algorithm writing should be made in simple models.

SIMP 3D code for Matlab the simulation is done is by Liu et al. [80] and for in-depth detailed information how the used Matlab SIMP 3D code works and the source code, please refer to the article “An efficient 3D topology optimization code written in Matlab” [80].

Published **LSM 3D** codes did not exist during the research. Therefore, a level set code for 3D had to be written for this task. The code was written during the research visit in University of California San Diego (UCSD). The base for the code was taken from Challis [79] and 3D part was added from Liu [80] SIMP code. As reference material other journal articles about toptopt written in Matlab by Wang et al. [48] and Otomori et al. [81] are used to understand the code better. The completed and written 3D LSM code is in Appendix II – LSM 3D Code at full. The code outputs a gif image and an STL file as results. The STL file can be read by any CAD program and then 3D printed.

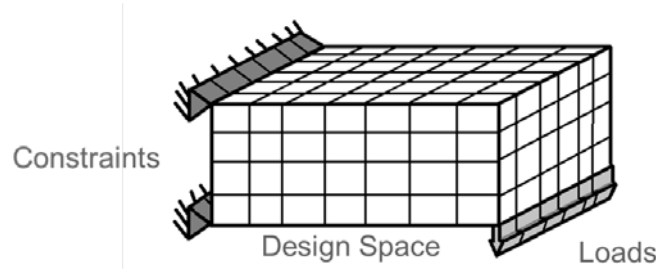


Figure 35. Cantilever in 3D model.

Comparing the two 3D optimization codes same problems were run on the codes. Firstly, a smaller problem with node count $15 \times 15 \times 15$ ($x=15$, $y=15$, $Z=15$) with 30% volume constraint problem was optimized (Figure 36). Both codes converge into a solution within 70 iterations. Similarity of the designs (Figure 37) shows through the STL model.

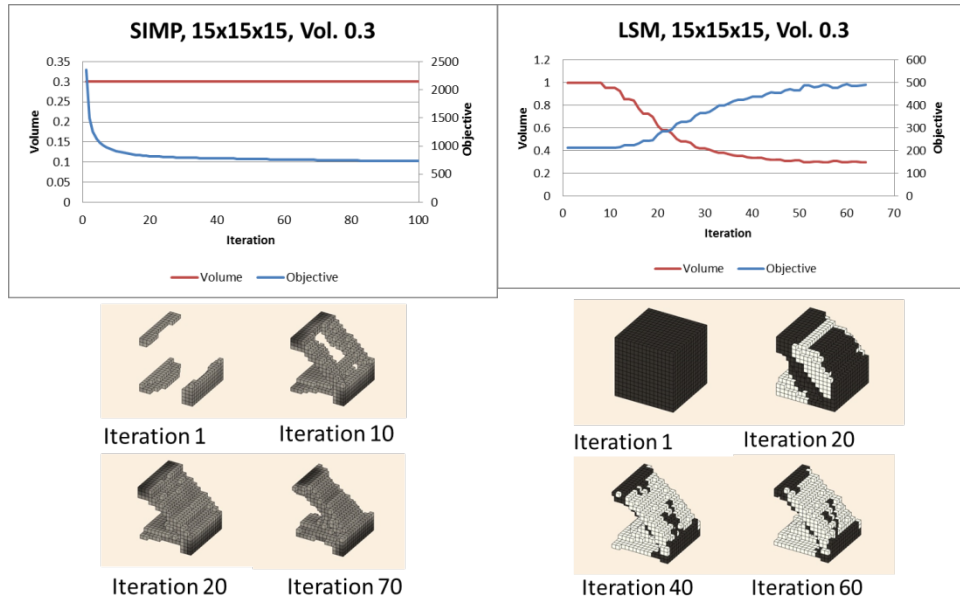


Figure 36. $15 \times 15 \times 15$ mesh cantilever optimized with Matlab: left 3D SIMP and right 3D LSM.

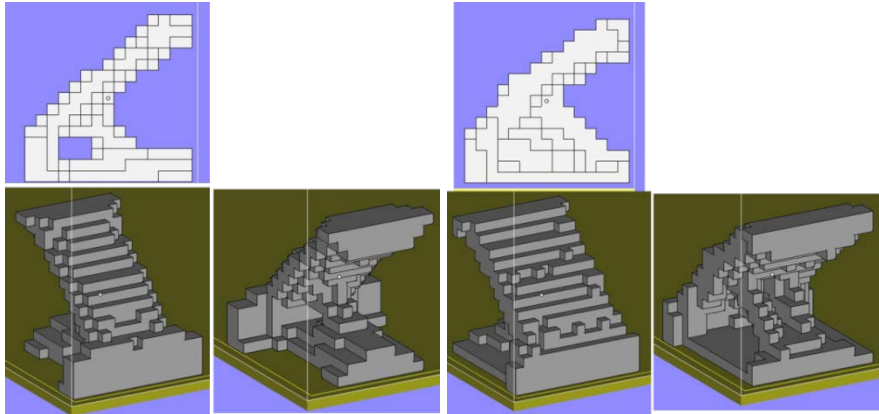


Figure 37. CAD model printed out from small 3D cantilever simulation: left 3D SIMP and right 3D LSM.

For larger optimization problem a design mesh size consisting of $60 \times 30 \times 30$ nodes with 30% volume constraint was chosen for simulation as the mesh is large enough to give good STL file as output. SIMP 3D and the written LSM 3D codes were run with Matlab 2016b. The results show convergence with both methods even in larger size with using iterative solver. The LSM convergence graph (Figure 38) is not smooth because the LSF is checked and updated every 5 turns to enable the design to be able to have hole creation and ability to pass over local optimums. Like in 2D design, in 3D the design is printed out in STL file and read with Materialise Magics 18. In Figure 39 the design differences are noticeable: where SIMP results have more freedom, the LSM results show symmetry with the y-axis.

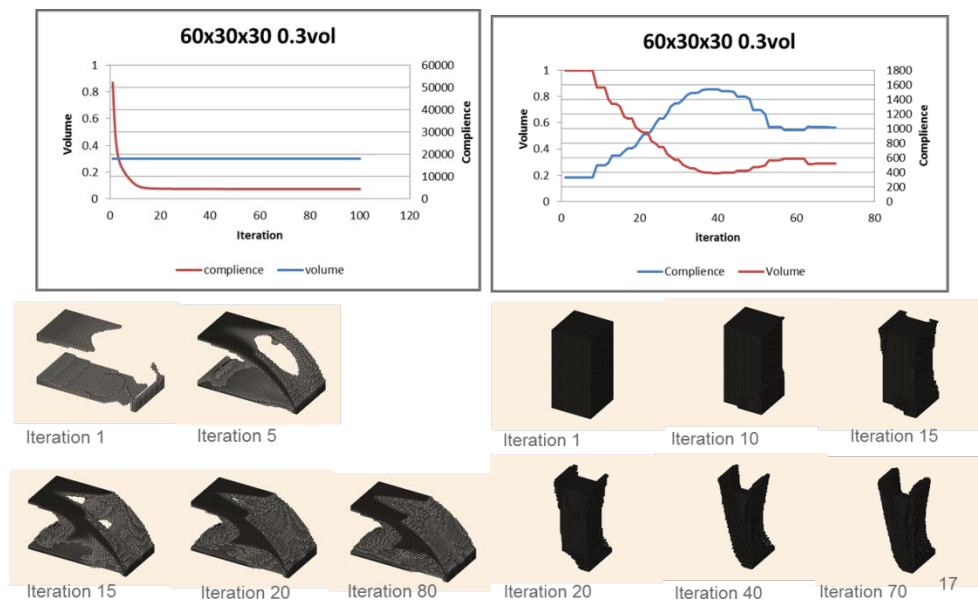


Figure 38. SIMP 3D convergence of $60 \times 30 \times 30$ mesh

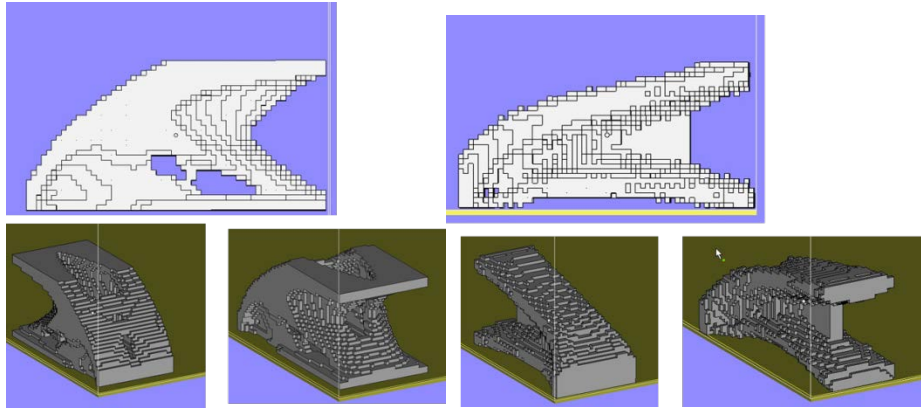


Figure 39. CAD model printed out from large 3D cantilever simulation: left 3D SIMP and right 3D LSM.

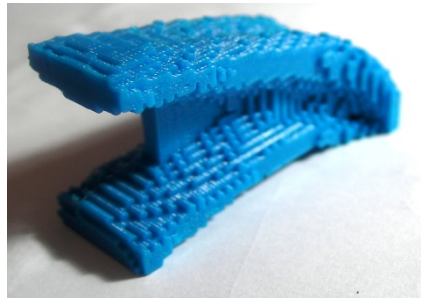


Figure 40. 3D printed model of 3D LSM output.

Commercial optimizer (Altair HyperWorks Inspire 2016) is compared with the SIMP and LSM codes run and written with Matlab. Inspire uses the same solver based on the SIMP approach as in Altair Optistruct [51]. The large cantilever problem of $60 \times 30 \times 30$ mesh is inputted into the program with corresponding forces (Figure 41). As the Inspire has additional constraints available, the problem is run with different design constraints to compare what is given by the Matlab scripts. The constraints are: no constraints, symmetry and extrusion. The results are given in Figure 41. The design without constraints are similar to the original results from SIMP as a strut like structure is formed in front. The symmetrical solution is close to the LSM solution from Matlab script. None of the cases gain from SIMP or LSM codes with Matlab are similar to the extruded constraint case. The extrusion is a 2D projection pressed in the y-direction to predefined thickness.

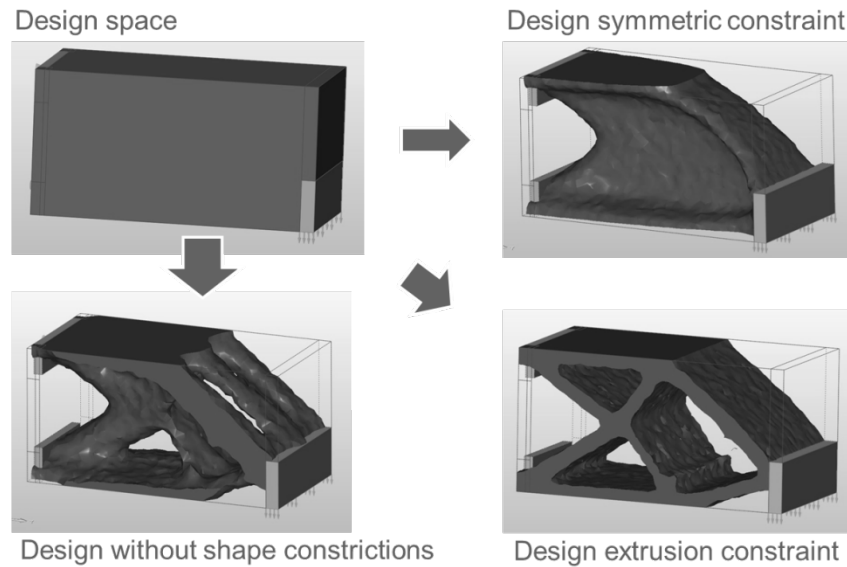


Figure 41. Altair Hyperworks Inspire simulation with the large cantilever 60x30x30 problem. Different design constrictions: free, symmetry, extrusion.

It can be said from 3 different algorithms (Matlab: SIMP and LSM, Inspire SIMP) there are as many different solutions. The open algorithm provides the user the transparency often needed to understand the mechanisms happening behind the scenes, whereas commercial solvers provide user-friendly experience, where no in-depth knowledge is necessary. Topology optimization is a useful tool for design suggestion but until now it needs verification by the designer before it can be utilized in the final product.

3.1.3. Summary

Topology optimization is powerful tool to use when understood well. The case study I was made to explore in depth the differences in two topology optimization methods. The methods have different approaches to the problem but the optimization path is similar. Where SIMP uses intermediate densities to calculate and update the design, the LSM uses fixed boundary.

Topology optimization algorithms were used through Matlab interphase. SIMP algorithm was written by O. Sigmund [78] and LSM algorithm was written by V.J. Challis [79] for 2D topology optimization. In the case classical cantilever problem was simulated and compared. SIMP approach achieved the final design and convergence in shorter computation time than the LSM approach. Slightly different outcome is noticed when comparing the two results. SIMP result is beam cantilever where LSM had an organic shape in cantilever. The major result might be the problem of inititing holes in LSM structure. The structure starts with full design space from where the shape is shrunk from. This inability to create

holes lead solutions like to artificial hole initiations by making the border instable.

The two optimization methods were converted into 3D optimization algorithms by Liu et al. [80] for SIMP and adapted for LSM by the author. The full code of the 3D LSM adaptation can be read from Appendix II – LSM 3D Code. The results were compared with Altair Inspire 2016 topology optimization and simulation. Inspire has few options to constrict the optimization code e.g. forging, extrusion and symmetries. These restrict the optimization into certain direction of optimization, whether it is good or not, it is up to the user to decide. The SIMP 3D code created free forming structure with openings and struts supporting the cantilever where as 3D LSM had structure resembling the symmetrical case from Inspire. With 3D LSM holes were unable to be created in the same fashion as in SIMP leading most likely to the difference in the geometry.

2D and 3D topology optimization codes were used and compared in this case study. Slight differences were noticed as the approaches were different. Topology optimization does not need fancy softwares as the mathematical solution is there and these result can be exported and 3D printed. FE-software makes life easier for engineers to be able to use the tools for their work.

3.2. Case Study II: Application of Product Design

There are commercial optimization software packages available for topology optimization and additive manufacturing in mind. One of these is Altair's SolidThinking Inspire 2016. It is a software for generating optimal structural concepts for parts and assemblies. It uses the optimization core of Altair OptiStruct linear SIMP optimization model [51] and makes it simpler to use for engineers. Introducing topology optimization and CAD with CAE is a powerful tool. Altair states in their brochure: *"Altair Inspire is a tool to help design structural parts right the first time, reducing costs, development time, material consumption, and product weight."* Inspire was used to draw, simulate and check the designs made in this research.

The aim of this case study was to use commercial software to optimize a simple shape with correct material properties that correspond to a specific 3D printing technology. The use of polymers is chosen because it is possible to manufacture shapes without restrictions as the parts can be manufactured without support structures or with dissolvable support structures.

3.2.1. Topology optimization and design

A simple shape for topology optimization of a three-point bending test specimen was optimized with Altair Inspire 2016. Design space of $H20 \times W20 \times L70 \text{ mm}^3$ (Figure 42) is used. The design is separated into 3 different areas: modifiable design space (red), two support plates 2 mm thick to allow the load pressure to

distribute equally through the design to compression rig. The design of compression rig consists of two cylindrical lower supports having a 10-mm diameter and an upper pressing cylinder with 10 mm diameter as the lower supports.

There is a standard for flexural three-point bending test specimen in ASTM Standard ASTM D790-10 [82] “*Standard test methods for flexural properties of unreinforced and reinforced plastics and electrical insulating materials.*” The topology optimized sample is not a standard specimen cut from sheet or laminate. Therefore, the flexural test is made for the non-standard specimen in the best way as possible to follow the standards guidelines.

The design with two plates and the pressure jig was chosen to create stable pressure points from the three-point bending pressure and let the optimizer have the freedom of design inside the sandwich. The optimizer was asked to solve a problem of minimizing volume with a pressure load of 5MPa (1000 N) with a safety factor of 1.2. A loading condition: “*Sliding with separation loading condition with 2 mm smallest details*” were used for the toptopt. The boundary condition allows sliding and separation of the pressing cylinders with the part in non-linear fashion. The pressure load of 5 MPa is implemented of the half of the pressing cylinder ($A_{\text{pressure}} = 10 \text{ mm} \times 20 \text{ mm}$) and on the centre line of the specimen. The design breakage point considering the safety factor is 1200 N. Material properties from topology optimization were implemented to the topology optimization material as written in Table 5. ABS Inspire material is a pre-existing material in the simulation program and it is shown as reference for other materials properties. The modified and inputted material properties are listed in Table 5.

It is known that the AM materials have asymmetric properties most notably alongside the build direction also referred as Z-axis. The asymmetry is taken account with the best tensile strength (yield) value and the lowest tensile strength (yield) value. For PEEK HP3 only one tensile strength (at yield) is reported on the xy-plane by the manufacturer, where in case of ABS Plus P430 the worst and the best values for yield breaking are used, hence, the 2 models from ABS plus. Model 01 is the best case with 52MPa strength and Model 02 is the worst case with 31MPa strength. With these models also the optimisations effect is considered as Model01a values are for 1000 N force (5MPa) with 1.2 factor of safety and Model01b values are for 800 N force (4MPa) with 1.5 factor of safety bringing the breaking point at the same value of 1200 N. The two different forces for ABS are shown in Figure 44. In polymers, a yield point is difficult to pinpoint accurately and for example with PEEK the material behaves as a brittle material, ultimate tensile strength is given in all reference material data sheets and therefore tensile strength is chosen as the variable to represent the yield.

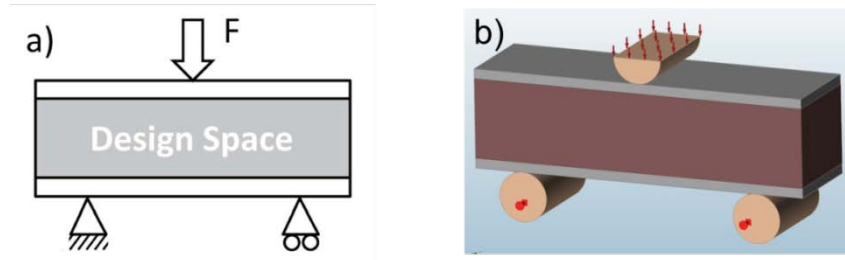


Figure 42. Flexural three-point bend specimen design: a) schematic of the design, b) design in Inspire 2016. Red: design space, silver: non-design space to equally distribute the load, round cylinders: support and force cylinder.

The single topology optimized structures are presented for PEEK in Figure 43. The two different models and a and b load cases are presented in Figure 44. With the same material parameters in Model01 between a and b there is a slight change in the volume of the optimized structure. Similarly, a larger design space is observed with the Model02. The a is slightly smaller than the b model.

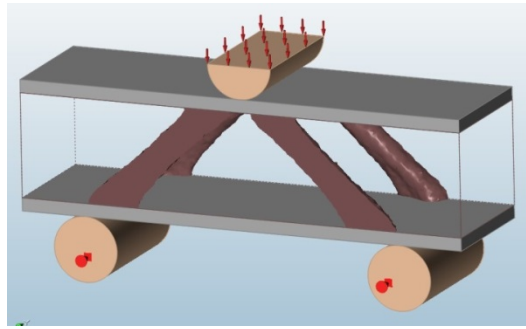


Figure 43. Topology optimized result EOS PEEK.

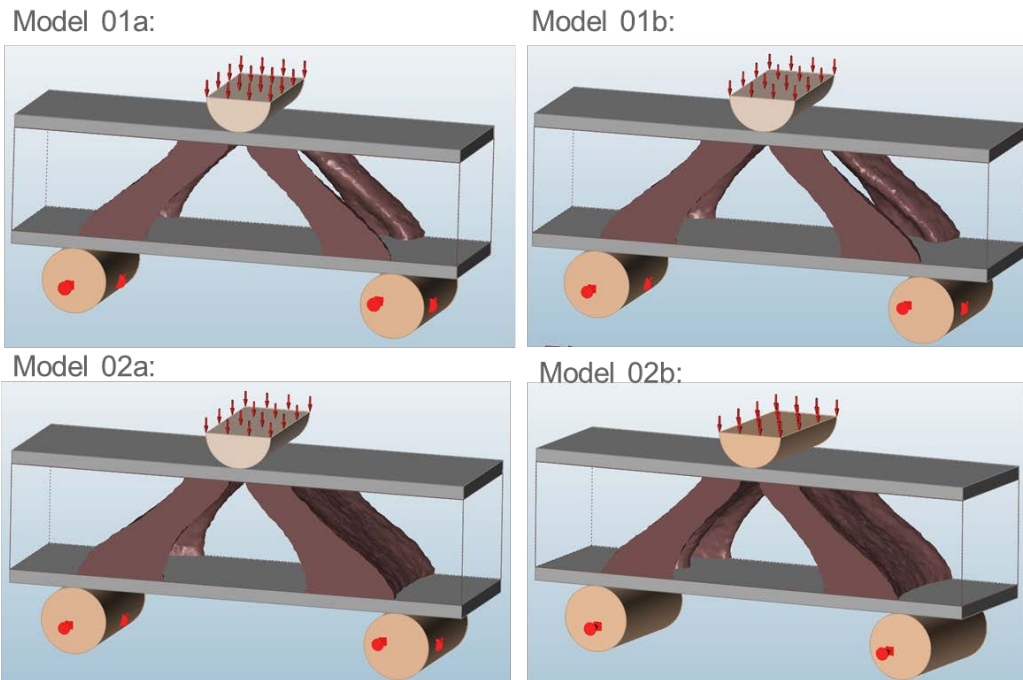


Figure 44. Topology optimization result with ABS Plus P430 at strength of 52 MPa (Model 01) and 32 MPa (Model 02). The a parameter set has pressure load of 5MPa with 1.2 factor of safety and b parameter set has pressure load of 4 MPa with 1.5 factor of safety.

Table 5. Material properties used in simulation

	ABS Inspire	PEEK HP3	ABS Plus P430	ABS Plus P430
E (MPa)	2000	4250	1650	1650
μ	0.35	0.3931*	0.35*	0.35*
Density (g/cm ³)	1.06	1.315	1.06*	1.06*
Yield Stress (TS yield)(MPa)	45	90 XY-direction	52 XY-direction	31 ZX-direction
Coefficient of thermal expansion (1/K)	63e-6	45e-6*	88.2e-6	88.2e-6
Manufacture system	Reference	EOS	Stratasys	Stratasys

*General value of plastic

3.2.2. Manufacture and Testing

ABS samples are manufactured with Stratasys Dimension Elite FDM (Figure 45) from ABS Plus P430 material provided by Stratasys. The parts are manufactured for both models with 3 different directions (Figure 47). The manufacture parameters are default parameters with 100% infill and solvable support structures.



Figure 45. Stratasys Dimension Elite material extrusion machine.

Laser sintering is done with EOS EOSINT P800 laser sintering system (Figure 46). It is an high-temperature laser sintering system, that can reach building temperature of 385°C in order to process higher melting polymers such as PEEK. Therefore, it can be distinguished from a normal SLS machine designed to process polyamide around 180°C temperatures. The build chamber diameter for P800 is 700 x 380 x 560 mm³ and the machine uses a layer thickness of 120 µm. Two 50 W CO₂-lasers scan with a speed up to 6 m/s. [83] Manufacture parameters are EOS manufacture parameters for PEEK.



Figure 46. EOS P800 laser sintering machine.

PEEK (Polyether Ether Ketone) is a biocompatible plastic with high-temperature performance, good wear resistance, good chemical resistance and high mechanical properties [84].

Parts are manufactured in 3 specific orientations as shown in Figure 47 for PEEK with LS and ABS with material extrusion.

- **X-direction** is built on the xy-plane and accordingly to bend test force.
- **Y-direction** is built on the xz-plane and 90 degrees rotated to bend test force.
- **Z-direction** is built on the zy-plane and the build layers will be directly loaded by the bend test force.

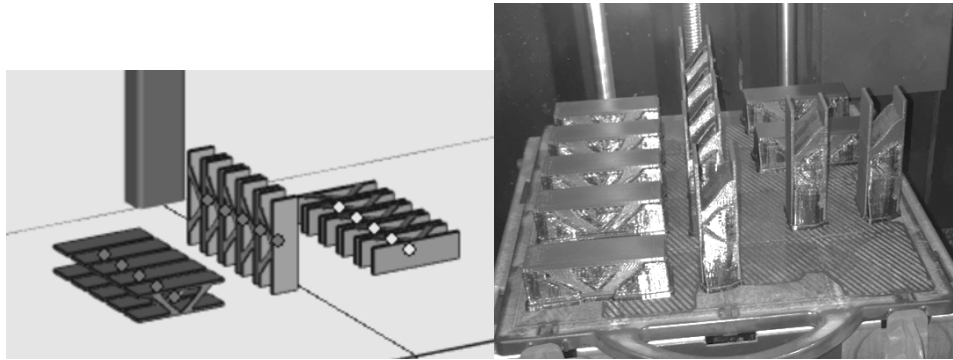


Figure 47. Manufacturing directions for EOS peek (left) and ABS (right)

The three-point bending apparatus used is a computer controlled Easydur testing machine (Figure 48). It has adjustable support span and accurate load cell. The numerical values for testing speed and testing variables (e.g. force) can be modified as required.

Testing values with three-point bending rig (Figure 48):

- Force: 0 – 5000N
(Design force 1000 N with 1.2 safety factor: breakpoint at 1200N)
- Speed: 0.0423 mm/s [85]
- Pressing distance max: 15 mm
- Support span: 50 mm
- The tests were filmed with 240 fps (1 frame in 0.004 s) camera for further analysis.



Figure 48. Three-point bending test machine.

3.2.3. Selective Laser Sintered Material

Bend test results for PEEK is presented for all the samples on Figure 50 and for individual directions: X-direction (Figure 51), Y-direction (Figure 52) and Z-direction (Figure 53). The design load is 1000N and the part is calculated to break at 1.2 times of the design load, that is at a force of 1200N.

The compliance for the factor of safety and the compression and tension fields are shown in Figure 49. The factor of safety shows that the major stress is in the struts and near the joints of the struts to the top and bottom layers. Instead tension and compression mapping show gradients of stress on the top and bottom of the structures.

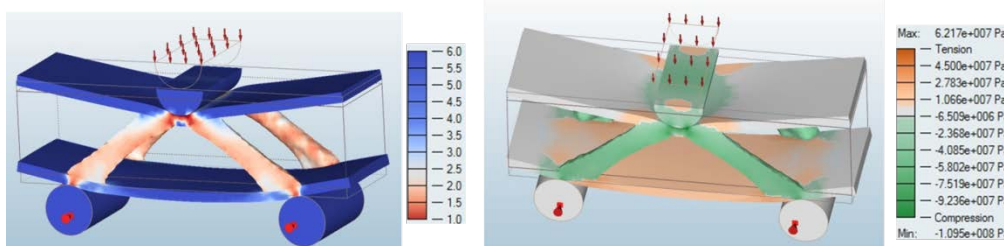


Figure 49. Left: Safety factor. Right: tension (orange) and compression (green) areas in the model EOS PEEK.

Results have a uniform slope but the failure happens in a different spot. X- and Y-direction builds can handle 1000N compression force as designed but in many cases the part cannot withstand the 1200N force. In case of Z-direction, the breakage force is lower and only one specimen made above 1000N force before breaking. The calculated strength from the material data is from the xy-directions,

because the property for the z-direction is not reported. However, it can be assumed that the strength in the z-direction is about 90% of the strength in the xy-plane. It is noted that the z-direction anisotropy has an effect lowering the strength of the part.

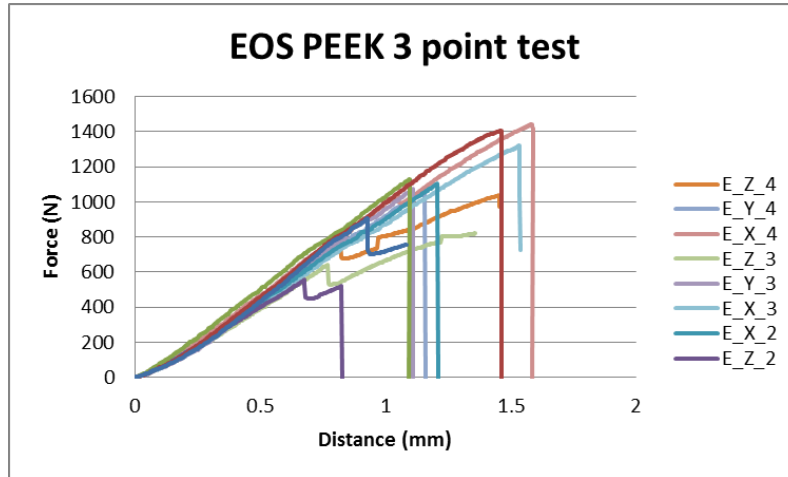


Figure 50. Pressure test results for PEEK sample X-, Y- and Z-direction. Design force 1000 N, break point 1200 N. Individual directions are shown separately in figures 51-53.

Specimens show two breaking patterns: single- and multiphase breaking. Single phase breaking (Figure 56) happens when the structure can handle the load before and at one point it breaks without a notice. The breakage is faster than 0.004s, that is the limit of the slow-motion video recording. Figure 56a is at the start of the force being applied. Figure 56b is when the force is the maximum and the bending is the most. Figure 56c is 0.004s later than the Figure 56b representing the spring motion release after breaking and the flight of the specimen away from the screen.

Multiphase breaking (Figure 57) happens slower than the single-phase breaking. It can be in all the manufacturing directions but the Z-direction shows it the most often. Figure 57 a&b represents the same loading as in one-step breaking. In Figure 57c a stress relaxation occurs by crack propagation when a part of the structure gives away lowering the top plate and resulting in a lowered force in the force diagram (Figure 53). A crack is started at a point where tensile and compression forces change and illustrated in (Figure 49 right). More common crack is observed below of the cylinder compressing the specimen (Figure 57d). The area below the pressing cylinder has both the compression and tensile stresses. These are shown in Figure 49. In the top part of the structure high forces create a crack and crack relaxation, but the compression forces near the crack structure keep the crack propagation under control. The failure pattern is revealed at Figure 57e, where it is visible how the left struts are accelerated away from the image and the rest of the structure is stationary before the collapse 0.004s later in Figure 57f.

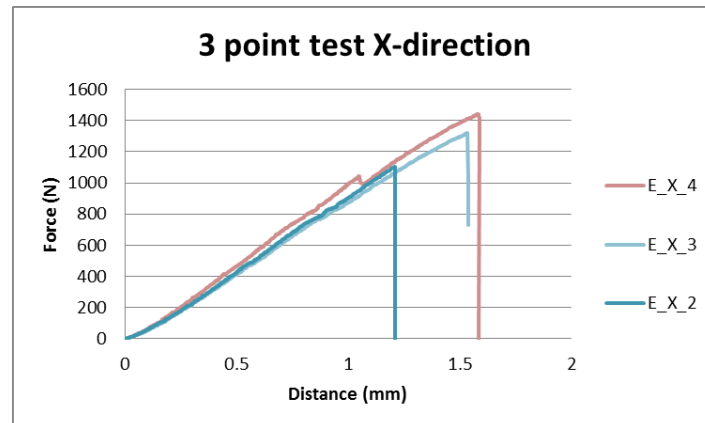


Figure 51. Pressure test results for PEEK sample X-direction. Design force 1000 N, break point 1200 N

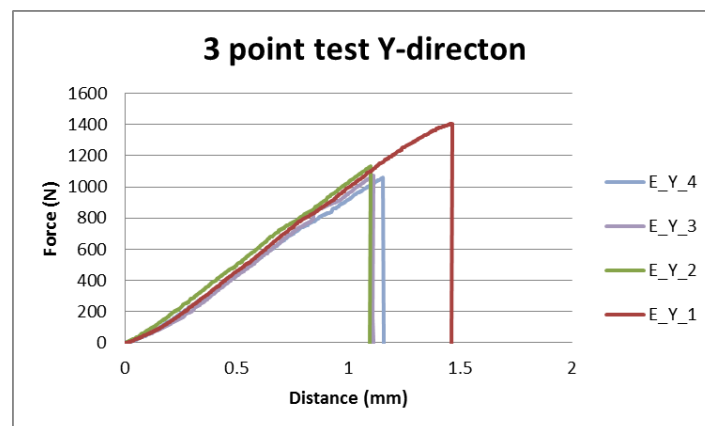


Figure 52. Pressure test results for PEEK sample Y-direction. Design force 1000 N, break point 1200 N

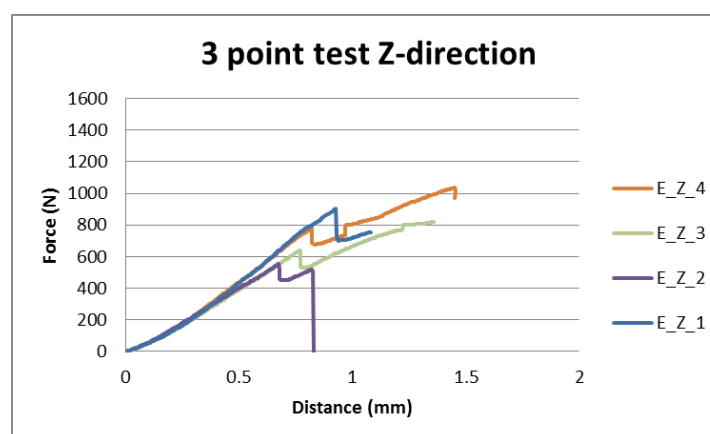


Figure 53. Pressure test results for PEEK sample Z-direction. Design force 1000 N, break point 1200 N

Figure 57 provides evidence about the method of breaking for the PEEK samples. The breakage happens in the lower strut where tensile and compression stresses meet as shown in Figure 49. The weakened part releases the spring tension stored in the system as the fracture continues as shear fracture forward. All of the broken PEEK samples have two similarities: break surface under the compression force and break surface before the lower support struts as seen in Figure 54.

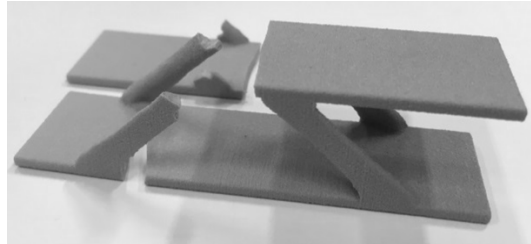


Figure 54. Broken specimen build in showing break pattern.

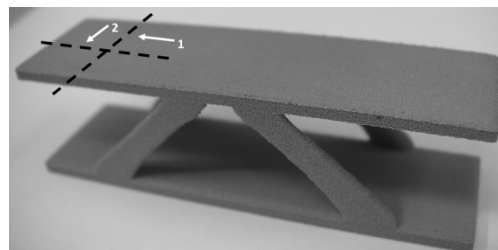


Figure 55. Material sample from pressure test specimen

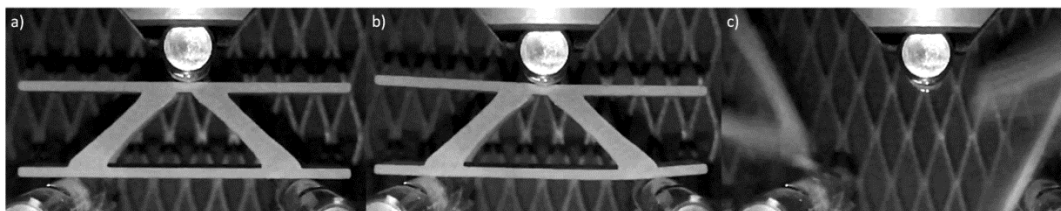


Figure 56. One phase breaking pattern when the whole structure fails at same time: a) specimen without load, b) specimen at max load, c) specimen failure.

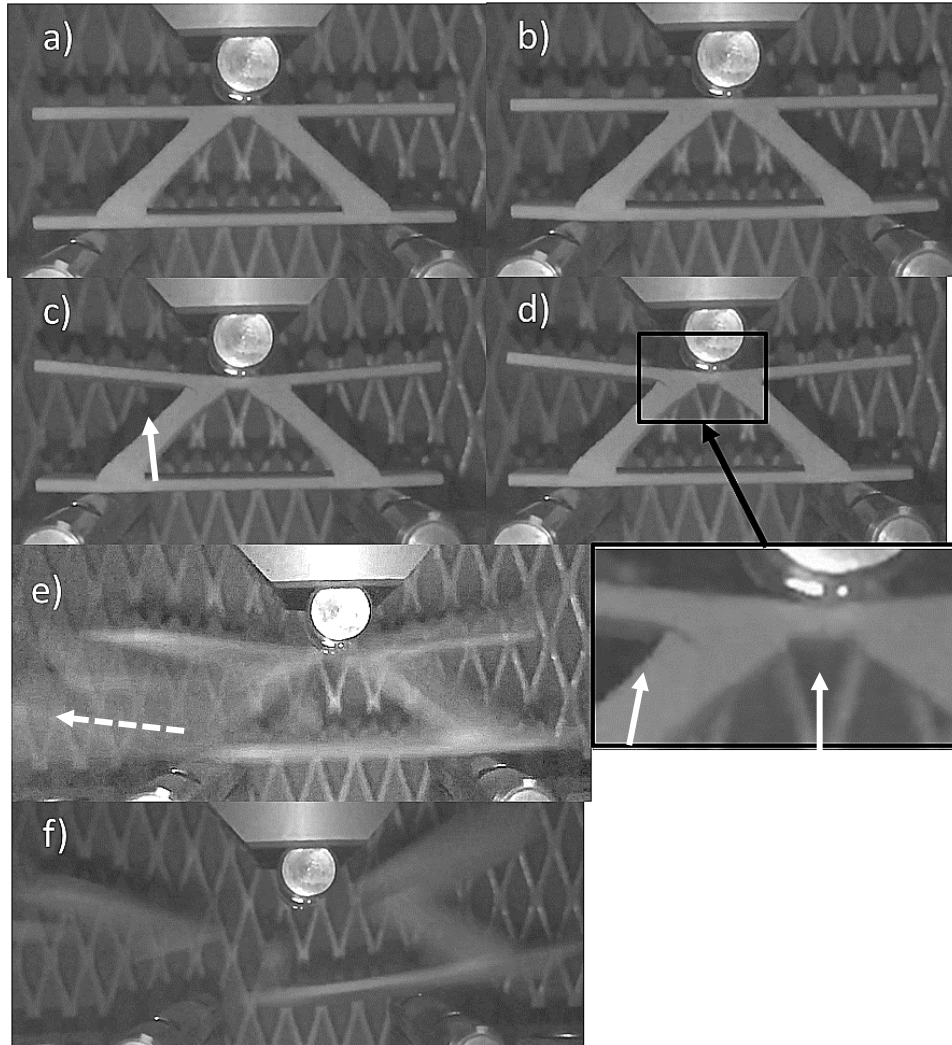


Figure 57. Two-phase breaking pattern. Bend test of EOS PEEK sample manufactured in Z-direction (E_Z_1): a) Specimen without pressure, b) specimen under load, c) specimen cracked under load on top left corner, d) crack propagation under load and new crack under the pressing tool, e,f) failure of the specimen

The microstructure of the PEEK specimen is analysed from the top of the specimens as shown in Figure 55. Cross sections to direction one and direction two are made to show the microstructure longitudinally (direction 2) and crosswise (direction 1). Material distribution and the manufacturing direction are visible in these cross sections and give hints about the plastic properties of the PEEK pieces. In Figure 59 (direction 1) and Figure 60 (direction 2) are stereomicroscope images of the part cut as shown in Figure 55. The slices show a layered structure similar to a slice from a tree. The layer structure creation is in Figure 58 and build directions (Figure 47) shown schematically how layers are

depending on the build direction. When build happens in X-direction in both slice directions the stacked Z-layers are visible. Build on the Y-direction cut slice 1 has the 90-degree tilted Z-layers visible, when in the longitudinal direction 2 the top layer of the build is seen. The same as in Y-direction happens for the Z-direction build but in opposite order. The part microstructure is not uniform, but rather layered and the layers are distorted depending on the build direction. During the build, the laser melts the plastic and when it solidifies the plastic curls upwards due to the shrinkage.

Figure 59 is the slice from the critical direction of the load at the manufactured part. In X-direction manufactured samples the cross section consists of layers into Z-direction and the direction of load is concentrated plate wise at the X-direction. In Y-direction manufactured samples there is a 90-degree shift of the plates from X-direction. In both X-direction and Y-direction, the load is distributed alongside the layers, whereas in the Z-build the force applied by the bending test apparatus is in the same direction as lamellae are. This means that any weakness between layer adhesion will show in the results, especially for the Z-direction.

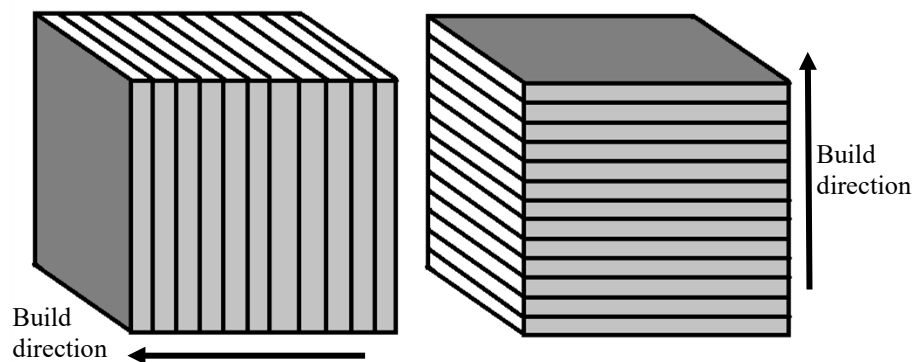


Figure 58. Material slice according to build direction.

The X-direction cuts (Figure 59 and Figure 60) show darker porosity as black spots on every layer interphase near the end of the part. Similar pores are also visible on Z-direction builds, but in Y-axis this is not visible as large scale as in X-direction. This might be due to the higher thermal input or the larger melt area in X-direction in comparison with Y direction. The powder bed is preheated 3 – 12 degrees lower than the melting temperature and the heating effect is more visible in the corners where the CO2 laser needs less energy to melt the polymer powder. The darker layers can be an indication of degradation by re-melting the structure. The porosity near edges of the part can create stress concentration that will evolve into a failure point. This works as a starting point for fractures that lead to eventual failure of the specimen. From the failure point, the fracture (Figure 61) does not proceed in alongside of the Z-plane, but sheared on a 45-degree angle. In Figure 61 both sides of the struts failure point from Figure 57 are

shown. The fracture has the breakpoint and the dynamic crack propagation direction.

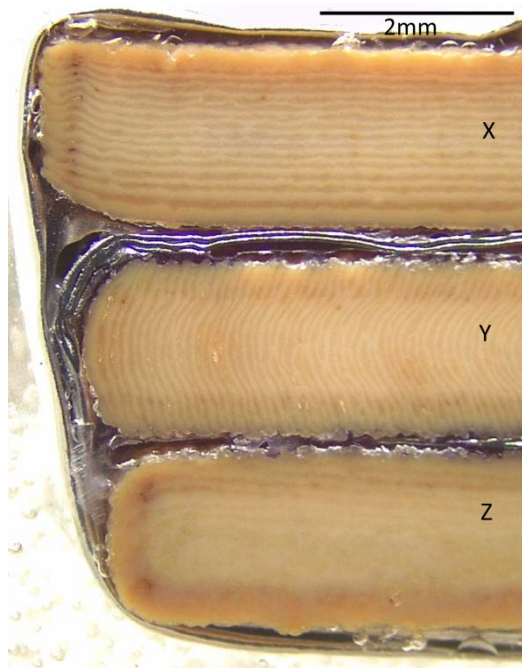


Figure 59. Material in direction 1, top X-direction, middle Y-direction, bottom Z-direction.

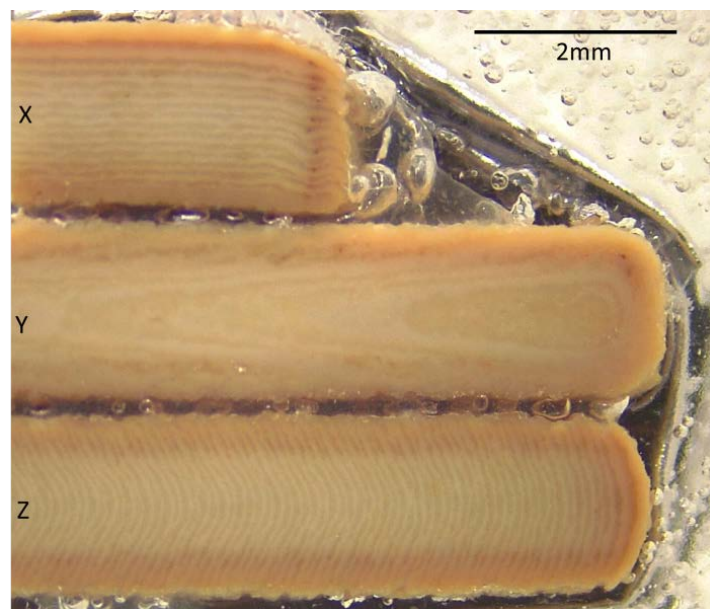


Figure 60. Material in direction 2, top X-direction, middle Y-direction, bottom Z-direction.

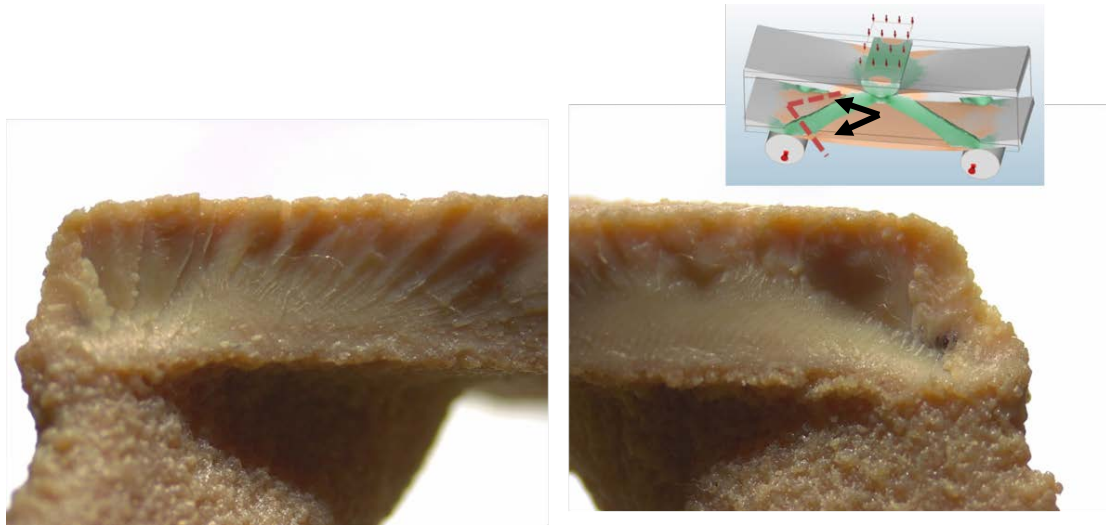


Figure 61. Fracture surface along Z-direction PEEK specimen.

PEEK manufactured by LS behaves similarly to brittle material in temperature below glass transition temperature [86]. On the right side of Figure 61 there is a dark pore where a distinguished crack propagation path is starting. On the left side of Figure 61, there is similar brittle breakage area surrounding a rapid fracture with flakes on the top.

Vickers micro hardness of the PEEK material is measured with 100g weight 30.5 GPa HV0.1. Average values of the material through the cross sections (Figure 59 and Figure 60) to both directions are measured and visualized in Figure 64.

Grid measurements from the different build directions do not give a wide range of hardness values indicating that the microstructure is homogenous. Nano hardness measurements made with Berkovich nano hardness tip (Figure 63) gives average nano hardness of 0.45 GPa with both of the directions and all build directions. The hardness measurement tip is small and it is possible to measure different phase hardness for metals. In PEEK, a line hardness measurement was made to investigate possible differences between the layers on Z-axis. The measurements (Figure 64) show two different hardness clusterizations. One with 0.3 GPa nano hardness and the other 0.5 GPa nano hardness. The hardness is not yet fully understood from where the difference comes from but it can be the difference between crystallized and amorphous phases or it can be the difference in the dark and bright area of the microstructure. The effect needs to be investigated more carefully to be able to say an accurate reason for the difference. The first and the last measurement points of 0.2 GPa come from mounting resin hardness

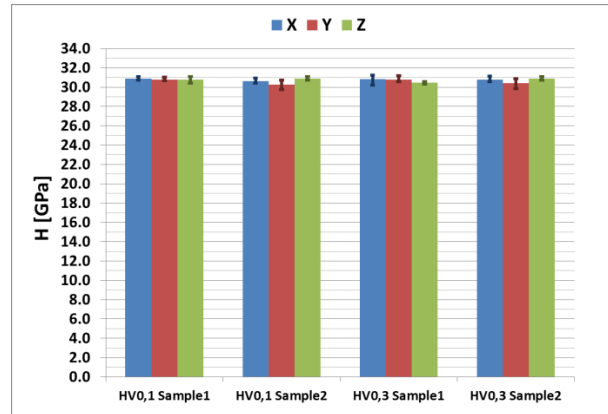


Figure 62. Vickers micro hardness (HV0.1) of the PEEK slices with 100g weight.

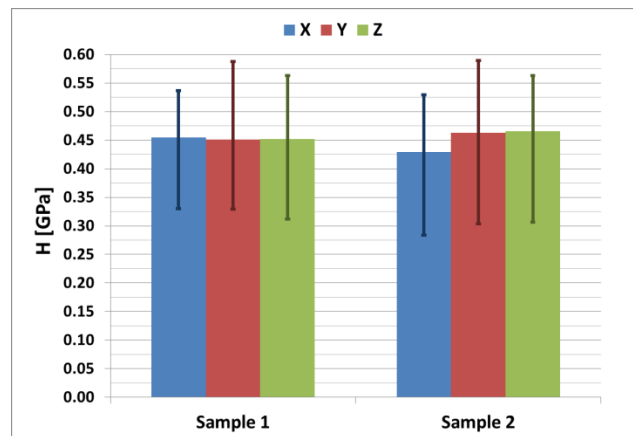


Figure 63. Average hardness measurement with Berkovich nano hardness tip.

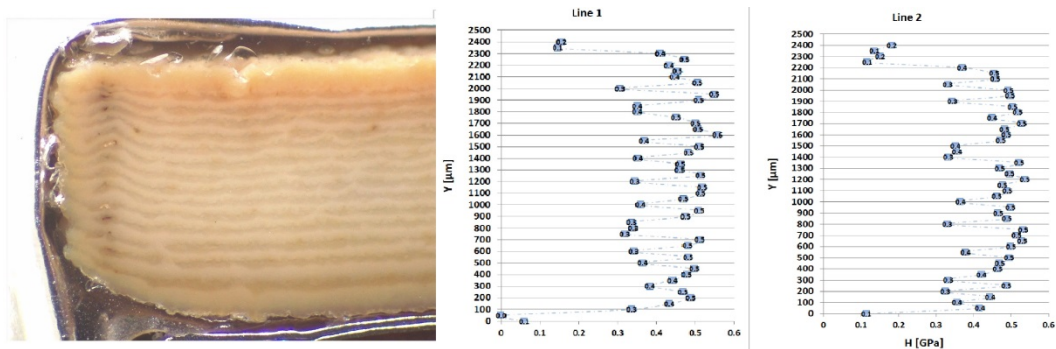


Figure 64. Hardness profile of X-direction alongside of Z-axis with hardness measurement with Berkovich nano hardness tip.

3.2.4. Material Extrusion Material

Acrylonitrile butadiene styrene (ABS) is thermoplastic with good mechanical properties and it is used widely with material extrusion. ABS samples are manufactured in X-, Y- and Z-orientations (Figure 47) from Stratasys ABS plus

P430 with dissolvable support structures. The compression test specimens are simulated with the lowest (Model 02) and highest (Model 01) material properties by the material extrusion filament producer. It represents the worst and the best case that can happen when parts are manufactured with material extrusion. The samples were produced in all three orientations. Anisotropy of the parts is the worse in the Z-direction of the build where the layers are stacked on top of another.

The compliance of the model with a factor of safety is shown in Figure 65. The safety factor is smaller in the a) models in comparison with the b) model. This model resembles the stress model with the highest stresses. The high stress is not enough to be able to know about the model. The change of stress direction between tension and compression Figure 66 gives important information. The stresses are similarly as in PEEK material (Figure 49). The difference is in the model02 where the stress concentration spread equally in the bottom plate via wide support instead of struts.

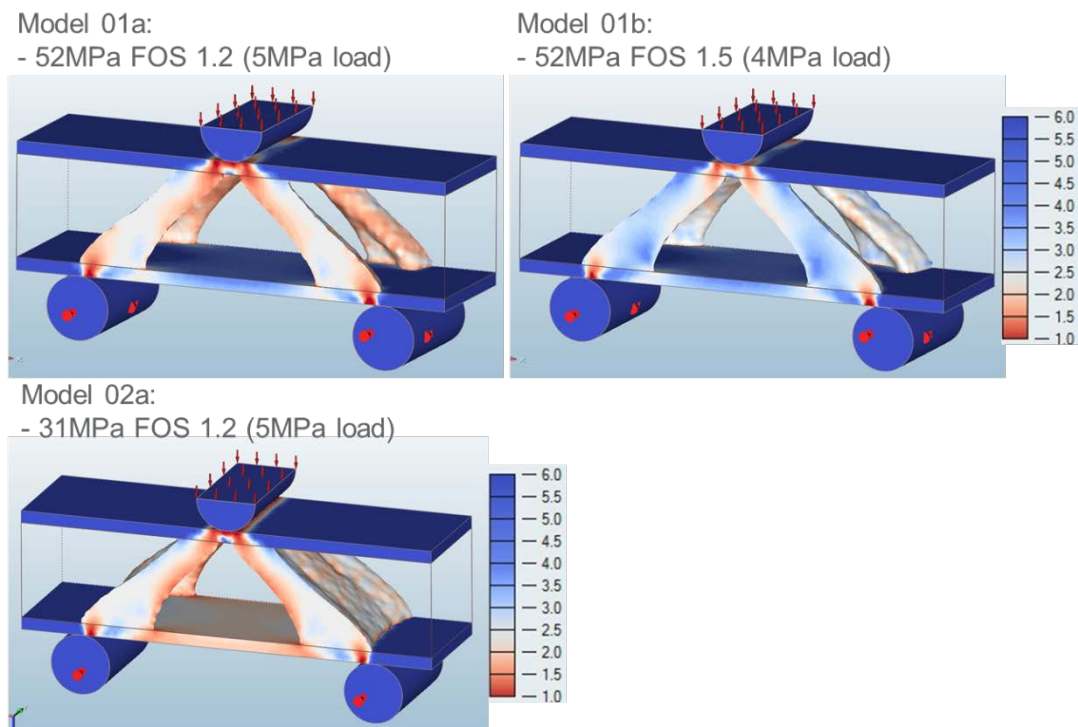


Figure 65. Safety factor between high stressed model 01 and low stressed model 02.

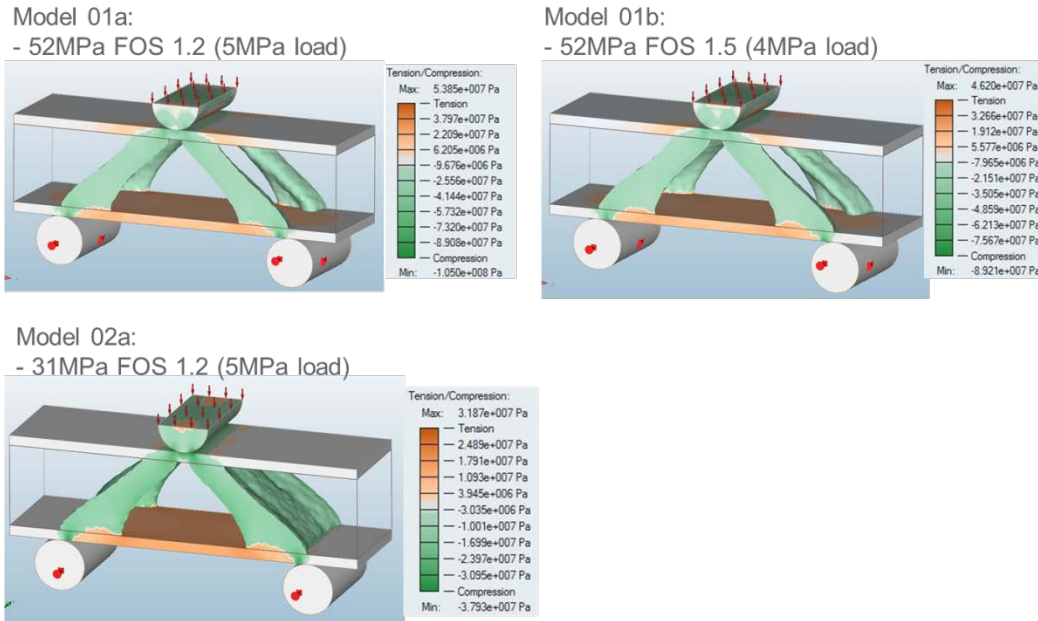


Figure 66. Tension and compression maps between high stressed model 01 and low stressed model 02.

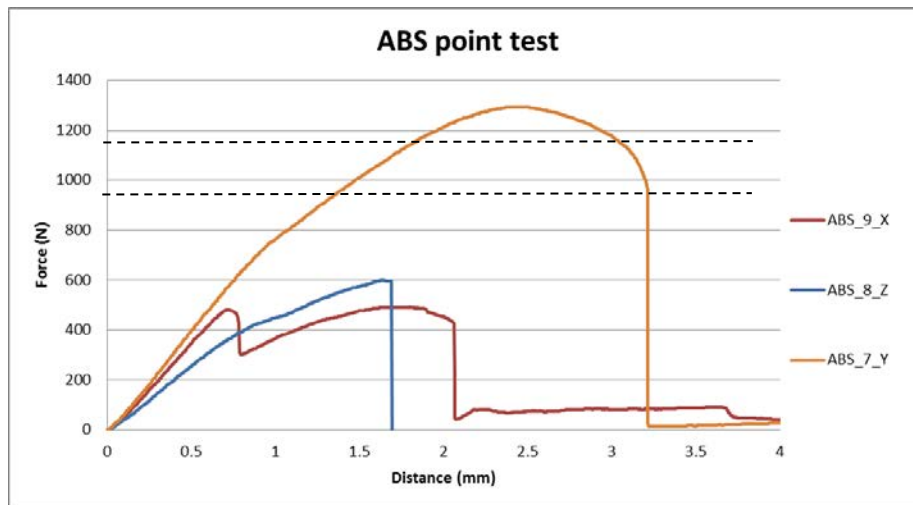


Figure 67. Model 01b, 3 point pressure test with x-, y- and z-directions showing the effect of direction. Design force 1000 N, breakpoint 1200 N. The individual directions are shown in figures 71-73.

A strong reminder of anisotropy and the difference from build directions is given in Figure 67, where the best case for material properties model 01b is tested for all directions. The mechanical behaviour of all parts is classified hereafter by direction:

X-direction, part delaminates from one bottom support followed later by the delamination of a second support and leading to collapse of the piece (Figure 69).

This fashion of breakage is observed in all the x-directionally manufactured specimens. Changing from the best case Model01 to the worst case Model02 creates larger support leading to better delamination resistance and the breaking force to reach 2000N (Figure 71). The resistance to pressure load increases when material properties change to lower.

Y-direction, delamination happens from a filling strategy discontinuity. The upper strut starts to give away and the bending from upper part continued until the piece snapped between layers near lower support skin (Figure 68). Moving from high material values to lower material values increase the stiffness of the structure that it will be able to hold over 2000N forces (Figure 72) as happened in X-direction. In both X- and Y-directions topology optimization is able to increase the stiffness with lower material properties dramatically.

Z-direction, breaking is brittle alongside the layer boundary (Figure 70). The failure happens for both models in the exactly the same place with little to change in force (Figure 73). This indicates much lower tensile properties than given to the optimizer. A bit lower material value than 31MPa might have been needed to have more material, that would have strengthened the bottom plate. The breaking happened near the area where Model02a shows a factor of safety close to 1.2.

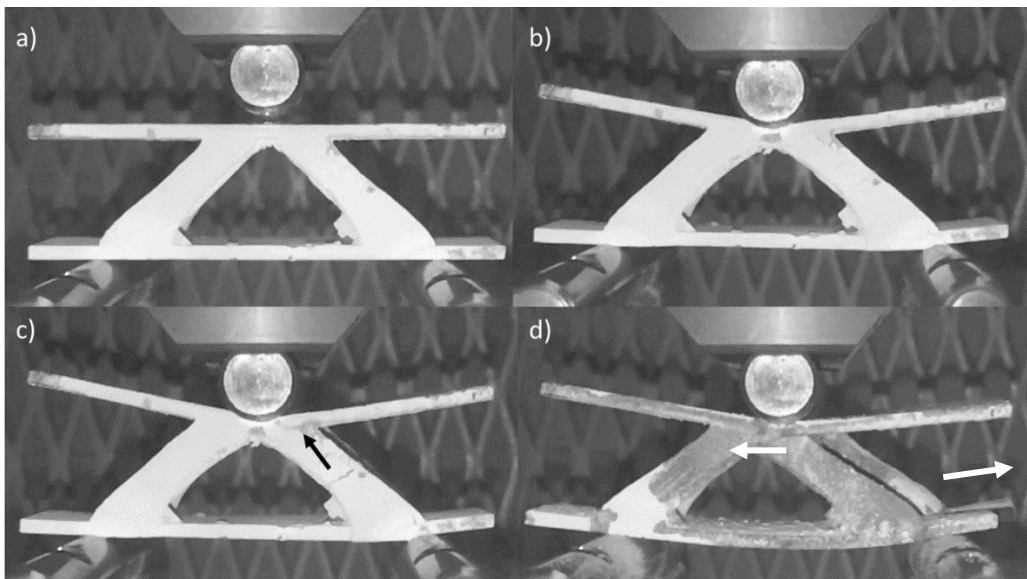


Figure 68. ABS Y-direction breaking: a) before pressing, b) ultimate pressing force, c) yield of the strut pointed by the arrow and the cutting of the strut, d) failure of the strut made the piece fail also on the lower side corner.

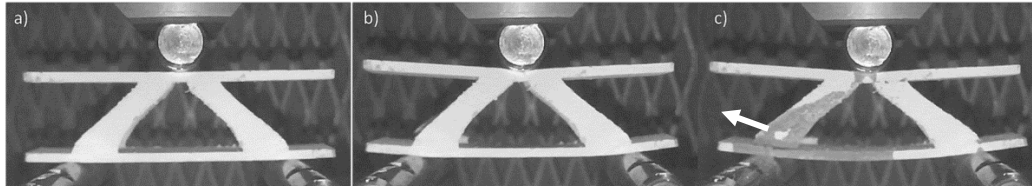


Figure 69. ABS X-direction breaking: a) before pressing, b) strut on the left side and behind gives away, c) second left struts gives away.

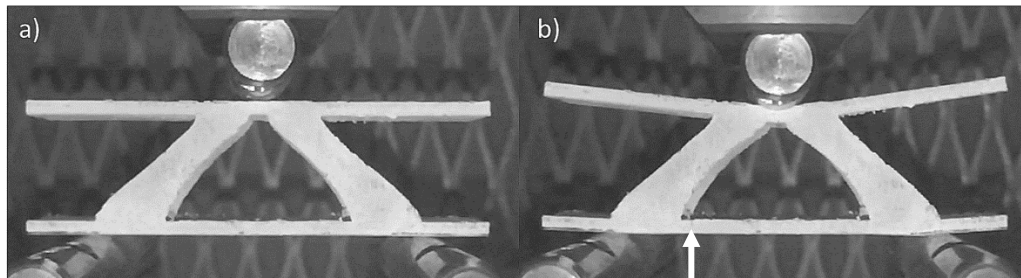


Figure 70. ABS Z-direction breaking: a) before pressing, b) breakpoint, a crack has formed below of the presser firstly and then to the left bottom of a strut.

The flexural three-point bending test specimen is not shaped according to ASTM Standard ASTM D790-10 [82] “*Standard test methods for flexural properties of unreinforced and reinforced plastics and electrical insulating materials.*” The test specimen is optimized with the values gain from datasheets that have been made from standard specimens. The difference in structure size is likely to be a factor as for smaller structures and other 3D printed parts the material values can be lower as noticed in [87] [88] for tensile strength. The tension and flexural strength in 3D printed part not only in Z-axis direction can be much lower than given in manufacturers datasheet as reported for ABS in literature 15MPa [89] and 20MPa [90] for the standard flexural specimen. The manufacturing method as well as the parameters inputted for the build matter. In current software packages the topology optimized structure is optimized with a specific material property given. If this property is off by e.g. 50%, it will mean that the optimizer is not getting the correct information about anisotropy to be able to make reliable optimization. The optimizer considers the material to be isotropic in this case. Selecting a manufacture direction in advance and giving individual strength tensors for all corresponding directions can be a solution for correcting the anisotropy problem. In current stage with easy to use commercial software there is no possibility to modify non-isotropic material properties. Therefore, a small change like the worst and the best properties values cannot be added inside one model to the performance along with a specific direction.

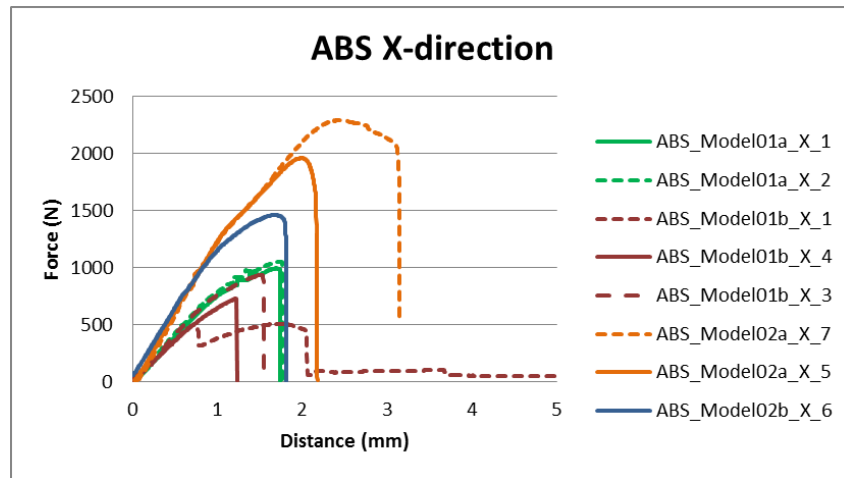


Figure 71. ABS Plus P430 X-direction bend test.

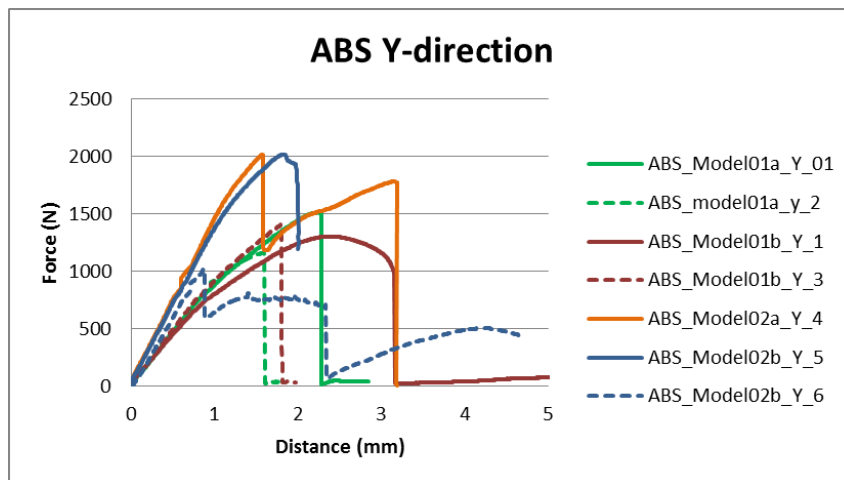


Figure 72. ABS Plus P430, Y-direction bend test.

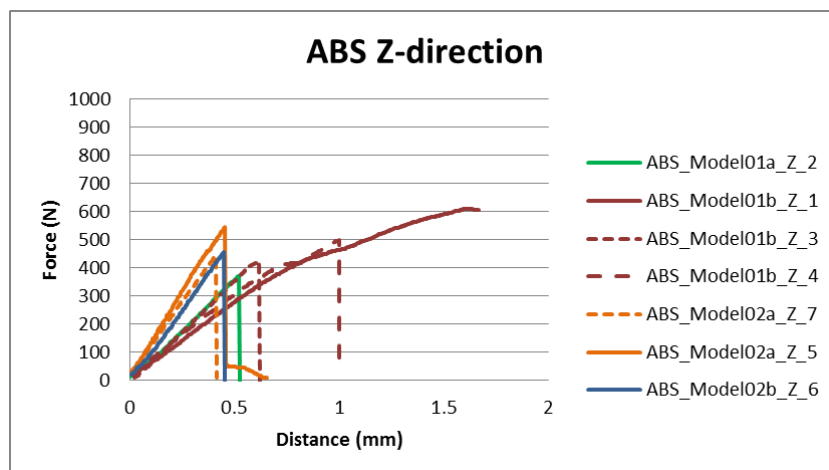


Figure 73. ABS Plus P430, Z-direction bend test.

Another reason for low material properties is in the filling strategy. Figure 74 has an X-direction strut and Z-direction cross sections. In these figures, the filling strategy is clearly visible. More than the filling strategy, the area shows empty space meaning that the actual filling is less than 100%. A small part of the structure can be holding the full load in the Z-axis direction and this will increase with increasing cross section. Thirdly surface structure is important for stress concentrations. A surface modification where the top layer is smoothed might affect positively in parts life in means of fatigue and load bearing.

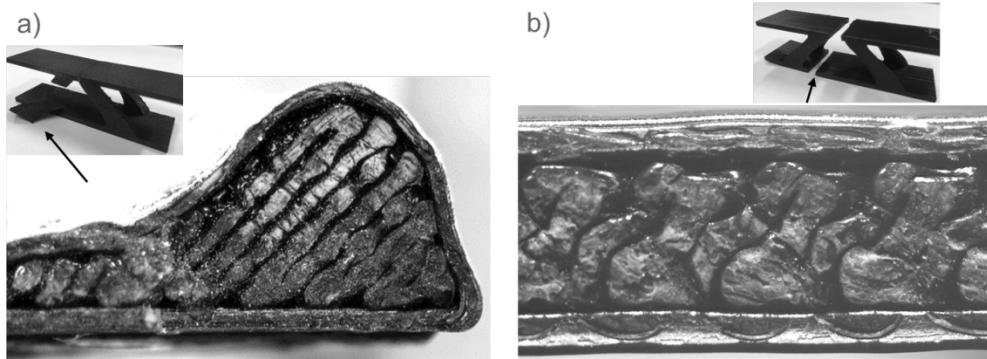


Figure 74. Cross section of failed ABS parts: a) x-direction, b) z-direction

3.2.5. Summary

Design approach for the topology optimization is made with commercial software of Altair Inspire 2016. The software was chosen as it had both topology optimization capabilities as well as simulation validation. Design to validate and test was chosen to be 3 point bending specimen as it has in perfect case only one known force affecting into know direction.

Material properties from a LS performance material PEEK and a common material with material extrusions good impact toughness ABS were chosen and optimized with the corresponding material properties given by the polymer manufacturer. The aim of this approach was to check if the simulated values would correspond in the actual verified values of the material. Also the unisotropy was a mystery as with PEEK the values given is XY-direction and the variation in ABS from different sources were high.

Samples were fabricated in 3 main directions and tested with 3 point bending test. LS samples were the most uniform with the samples holding the design load of 1000 N. The LS PEEK direction Z provided the weakest results and the fracture behavior was in two stage rupture where a pre failure happens releasing stresses what eventually leads to full failure in higher load forces. The similar behavior is observed with failing lattice structures as the stress concentration moves from a failing strut into different area. In X- and Y-directions the failure

was sudden. The difference between minimum Z- and XY-directions lowest value are 500 N in comparison with 1000 N having 50% difference in worst case.

Material extruded ABS behaved differently than PEEK. In ABS the weakest point was the layer boundary. In Z-direction the part snaps broken with low energy and this could not be compensated with calculating the results with different safety factor. Safety factor and different loading case indeed made X-direction better as delamination of struts became more difficult. In Y-direction, the layer orientation is the most suitable for bending load and therefore had the best resistance. The difference between Z- and Y-directions lowest values are 400 N in comparison with 1000 N having 60% difference.

The case study II highlighted the huge variety in anisotropy. Where LS material was similar between the directions, in material extrusion the variance was larger and not one off. It has to be said that in polymer side topology optimization was not successful to replicate accurate results. The differences might come from aspects what has not been addressed in the toptopt algorithm e.g. directional stiffness tensors with anisotropic material properties or breaking behavior of the corresponding material from a manufacture failure i.e. missing layer in material extrusion.

3.3. Case Study III: Metal Application of Process Design

3.3.1. Manufacture Equipment

Manufacturing equipment has a great impact on manufacturing quality. The product might be made with two similar machines but small differences create variance in quality e.g. in sense of accuracy, chemical composition and performance. This fact is especially true with additive manufacturing equipment where the quality of individual parts can have a huge effect on overall performance. These factors can be laser power, a 200W laser, and a 1000W laser might not produce exactly the same parts.

Laser powder bed fusion (LPBF) equipment used for the metal results is an EOSINT M270 dual mode (Figure 75) with PSW 3.7 software. Maximum laser power is 200W and effective building volume of the machine is 250 mm x 250 mm x 185 mm. Layer thickness can be varied between 10 – 60 μm and as shielding gas nitrogen or argon can be used. [91]



Figure 75. AM-machine: EOS EOSINT M270.

AlSi10Mg is a common cast alloy of aluminium and it is the main choice for LPBF AM manufacturing. It has high silicon content for the castability and the material can be used for thin walls and complex geometries. In addition to low weight and good mechanical properties, the parts can be heat treated to T6 heat treatment. However, hardening treatments are not recommended by EOS as the regular stress relieving in air atmosphere for 2h at 300 °C produce sufficient results. [92] The relative density is according to EOS after built 99.85% and density of 2.67 g/cm³. The chemical composition given by the manufacturer [92] is shown in Table 6. Material composition EOS AlSi10Mg Wt. % [92] Table 6.

Table 6. Material composition EOS AlSi10Mg Wt. % [92]

Al	Si	Fe	Cu	Mn	Mg	Ni	Zn	Pb	Sn	Ti
Balance	9.0 - 11.0	≤ 0.55	≤ 0.05	≤ 0.45	0.2 - 0.45	≤ 0.05	≤ 0.10	≤ 0.05	≤ 0.05	≤ 0.15

Ti6Al4V [93] is a strategic material for the industry and therefore it was the first AM material to be standardized. The material usage is varied from medical sector due to its bio-compatible to aerospace applications due to its lightweight with a density of 4.41 g/cm³ and excellent properties. The standardized composition is given in Table 7 for Ti6Al4V.

Table 7. Material composition EOS Ti64 Wt. % [93]

Ti	Al	V	O	N	C	H	Fe	Y	Other
Balance	5.5 - 6.5	3.5 - 4.5	≤ 0.15	≤ 0.04	≤ 0.08	≤ 0.012	≤ 0.25	≤ 0.005	≤ 0.4

Material parameters for these two alloys were studied and optimized at the Istituto Italiano di Tecnologia [94]. The AlSi10Mg and Ti6Al4V parameters are summarized in Table 8.

Table 8. EOSINT M270 fabrication parameters.

EOS M270	AlSi10Mg			Ti6Al4V		
	Scan speed (mm/s)	Laser power (W)	Hatching distance (mm)	Scan speed (mm/s)	Laser power (W)	Hatching distance (mm)
Core	800	195	0.17	1250	170	0.1
Up-skin	1000	195	0.2	1000	120	0.1
Down-skin	900	190	0.1	1000	120	0.1
Contour	900	80		1250	100	

Ecoblast/F machine made by Silco S.r.l., Italy was used for shot peening and surface treatments of manufactured parts. The blasting substance could be silica or zirconia beads, in a range of 100-200 μm diameter and an air pressure of 6 – 8 bars was used.

Optical microscope pictures used is a Zeiss Axio Scope A1 equipped with a Leica DFC295 camera. Field-emission scanning electron microscope (FESEM) images are taken with a Zeiss Supra 40 microscope. Macro photography is made with Sanyo DMX-HD1000 digital movie camera 10x optical zoom and 2.8 megapixel resolution.

Image processing software is a java based open source image processing software called ImageJ [95] developed originally by American National Institute of Health. After publication in 1997, the open source software has provided a platform where researchers and scientist can develop and expand the needed image processing algorithms for their niche application.

3.3.2. Design of holes

The design of holes is important in removing support structures from internal channels. How the size and design elements affect the results is experimented in this chapter. Different diameter and length holes build in vertical and horizontal are studied with a stereo microscope. The 2D pictures are processed and analysed with ImageJ software for roundness results.

Determining a shape of a particle or hole is more than just selecting the diameter of the hole. This can be demonstrated with British hexagonal 50 pence coin (Figure 76). Both the coin and a circle have a constant diameter, but the shapes are different. Many other form factors have to be considered to measure the pure roundness of a hole. ISO standard EN ISO 12181-1 [96] defines the


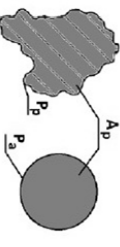
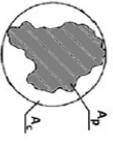

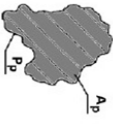
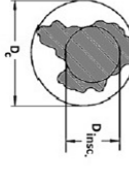
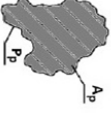
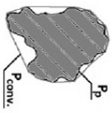
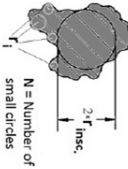

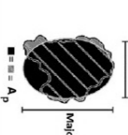
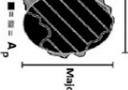
vocabulary for measurements that can be taken from a circle to describe the shape. In the standard four different methods for testing roundness is suggested. Those are described in detail in Figure 78.



Figure 76. British hexagonal 50 pence coin with a constant radius.

In order to examine the perfect shape, many sophisticated tools need to be used and the data accurately analysed. For shapes Rodriguez et al. [97] in lists many methods how shape factors can be calculated with or without image processing software. Table 9: 5 and 12 show the theory and equations behind results with ImageJ- software.

Table 9. Shape describing quantities and descriptions listed by Rodriguez et al. in [97]

EQ.	QUANTITY	DEF.	FIGURES	REF.
1	Sphericity (Φ)	$\frac{D_a}{D_c}$		Wadell, 1935
2	Degree of circularity	$\frac{P_a}{P_p}$		Wadell, 1935
3	Roundness	$\frac{A_p}{A_c}$		Tickell, 1938
4	Angularity	$\frac{A_p}{A_c}$		Pentland, 1927
5	Roundness/Circularity	$\frac{4\pi A_p}{P_p^2}$		Riley, 1941/ ImageJ
6	Inscribed circle sphericity	$\sqrt{\frac{D_i}{D_c}}$		Riley, 1941
7	Circularity	$\frac{P_p^2}{A_p}$		Blott & Pye 2008
8	Roughness	$\frac{P_p}{P_{conv.}}$		Jaino, 1998
9	Roughness	$\frac{P}{\pi * D_{avg}}$		Kuo, et. al. 1998
10	Roundness	$\frac{\sum r_i}{N * r_{max}}$		Wadell, 1932; Krumbein & Sloss, 1963; Mitchell & Sega, 2005
11	Sphericity	$\sqrt[3]{\frac{b * c}{a^2}}$		Krumbein, 1941, (def) Stuckraht et al., 2006 (picture)
12	Aspect Ratio ⁴⁾	$\frac{Major}{Minor}$		ImageJ and Image Analysis Pro 5)

A_p Area of the particle outline
 D_a Diameter of a circle with an area equal to that of the particle outline
 D_c Diameter of smallest circumscribed circle
 P_p Perimeter of particle outline
 P_a Perimeter of a circle of the same area as particle outline
 A_c Area of the smallest circumscribing circle
 A_i Area of a circle with a diameter equal to the longest distance between two points on the particle outline
 $D_{insc.}$ Diameter of the largest inscribed circle
 $P_{conv.}$ Perimeter, convex
 D_{avg} Diameter, average

1) This definition is almost the same as no. 3. There will be a difference if the particle is very bent, e.g. L-shaped.
 2) The average diameter may be calculated by usage of software.
 3) The dimensions a, b and c (length, width and thickness) are perpendicular to each other.
 4) AR defined as in the same image analysis software.
 5) Used software.

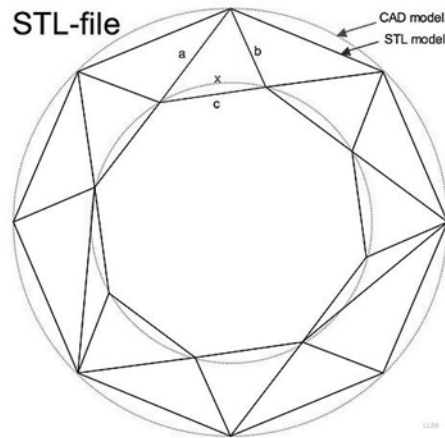


Figure 77. STL-approximation of a round object.

The holes are drawn as perfect circles in the CAD file. However, the quality of the STL file triangulation affects the quality of the model as illustrated in Figure 77. It is a common practice to remove details smaller than the layer thickness from the STL file to make the file smaller in size as these features cannot be manufactured with the accuracy given. Even if the computation efficiency was a bottleneck in the AM-machines, this was necessary. For characterizing holes there are four common methods defined in ISO-standard “Geometrical product specifications (GPS) - Roundness - Part 1: Vocabulary and parameters of roundness” [96]:

1. Minimum zone reference circle (MZCI)
 - Figure 78a, two concentric circles with least radial separation are fitted inside and outside of the shape.
2. Least squares reference circle (LSCI)
 - Figure 78b, one circle with the least number of squares to have the minimum local roundness deviation.
3. Minimum circumscribed reference circle (MCCI)
 - Figure 78c, the smallest possible circle to be able completely to surround the shape.
4. Maximum inscribed reference circle (MICI)
 - Figure 78d, the largest possible circle to be able to fit inside of the shape.

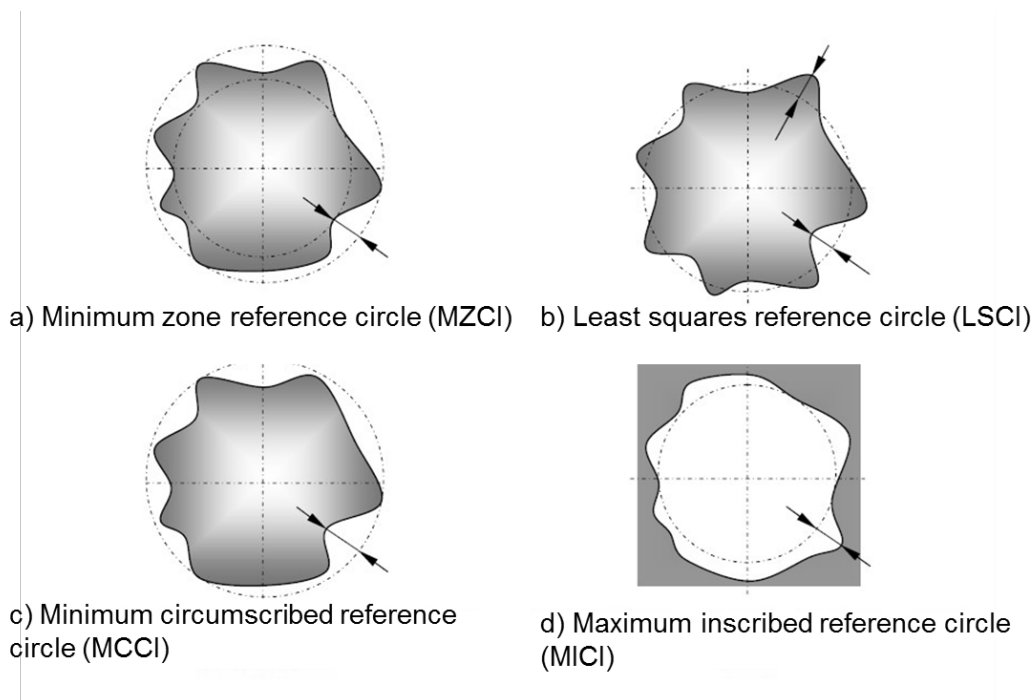


Figure 78. Circles mentioned in [96] standard. a) Minimum zone reference circle, b) least squares reference circle, c) minimum circumscribed reference circle and d) maximum inscribed reference circle. Figure from [98]

In every method (Figure 78) a circle called ‘a reference circle’ is drawn on the profile and the measurements are taken from the reference circle to the profile. The least squares reference circle is selected for measurements to be able to gain reference circle to peak and reference circle to valley values.

Four specimens were fabricated in Al10SiMg with EOSINT M270 Extended machine in IIT@Polito. Two pieces were manufactured horizontally with vertical holes (Figure 79a) to Z-direction and two were manufactured vertically with horizontal holes (Figure 79b). The hole diameters are 0.5, 1, 2, 3, 4 and the wall thicknesses are 15, 7, 4, 2 and 1 mm.

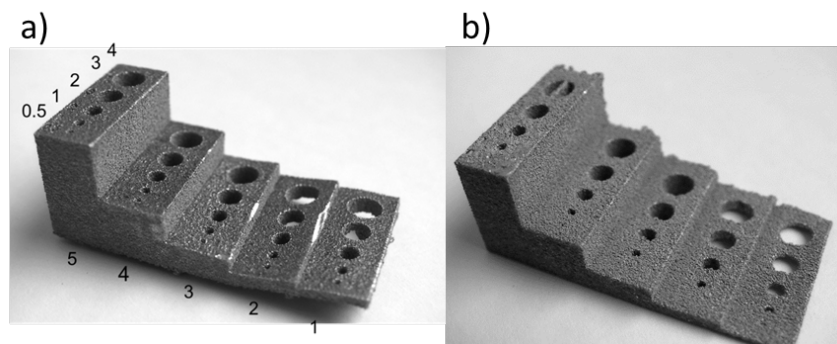


Figure 79. Accuracy hole sample a) vertical and b) horizontal

Images of the fabricated holes were taken with stereomicroscope Leica EZD4 from 4 specimens containing 25 holes each. A constant magnification of 8x is used and images are analysed with ImageJ software by modifying the original images to the binary shape of the hole. An example of this is shown in Figure 80, where stereomicroscope quality is compared with a light optical microscope (LOM): a) vs b). The reference circles are then fitted on the binary and roundness parameters are taken from the image.

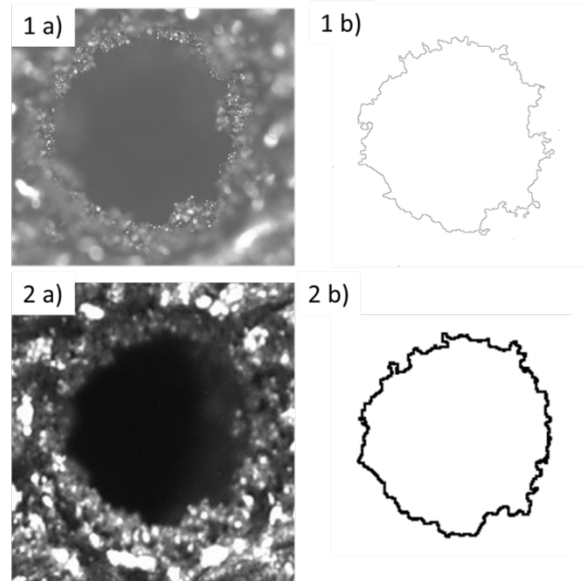


Figure 80. Comparison of LOM and stereo microscope in making a mask of the hole. 1a) LOM 5x image of 1mm diameter hole and 1b) its hole mask. 2a) stereomicroscope 8x image of the same hole and 2b) its mask.

To be sure of the accuracy of stereomicroscopy figures, a comparison from a light optical microscope (LOM) was concluded. The images were taken with Zeiss Axio Scope A1 (Figure 80: 1a) and Leica EZD4 (Figure 80: 2a), in respect, and converted to binary mask in the similar fashion. The results in Figure 80 1&2 b, show a big difference in the resolution of the picture, but the overall size and shape do not differ in large scale. Roundness for 1b is 0.960 and aspect ratio is 1.038. For 2b roundness is 0.955 and aspect ratio is 1.047. Therefore, it is concluded that stereomicroscopic image is good enough to measure the roundness variations for the holes in question. The limitation for LOM was that holes with diameter 2 or larger are too large to be analysed with the smallest magnification of 5x.

Measurements from these binary holes include:

- Roundness
- Aspect ratio
- Major axis
- Minor axis
- Feret's distance
- Least Squares Reference Circle Diameter
- Peak to reference circle
- Valley to reference circle

Roundness is a value of ellipse that ImageJ is fitting on top of the binary image. The roundness is calculated with the formula in section 5 of Table 1, where a value of 1 is a perfect circle and value 0 is a line. From the roundness, the Aspect Ratio is gained. The major and minor axis will describe if the hole is pressed. An Aspect Ratio of 1 is for a perfect circle and larger values indicate that the circle is elongated. Feret's distance is the longest distance between any two points along the hole's boundary. It is also known with the name of maximum calibre. Least Squares Reference Circle is fitted with multipoint area selection on top of the hole. It created a circle with the same area as the hole on the centroid of the hole. The maximum distance from this reference circle was taken to valley and peak to gain the maximum variation.

In vertical builds, the 0.5 mm diameter holes could not be manufactured. The holes had collapsed during the build and there was a discontinuity line showing on the surface that there had been something in the CAD file. In the 2nd horizontal build, the 1 mm thick surface had broken off on 4 and 3 mm diameter holes during removal and the results are not available.

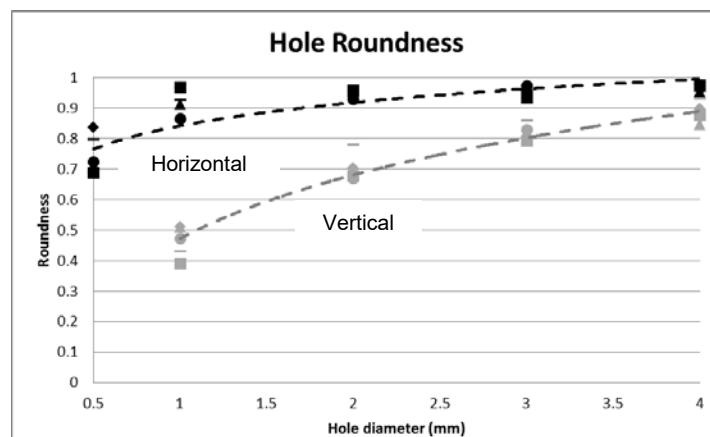


Figure 81. Hole roundness values in comparison to the hole diameter values. Black: horizontal hole and grey: vertical hole.

Hole roundness values are plotted out in Figure 81. The values for the different thicknesses vary a bit but the trend is logarithmic showing that the larger the hole the smaller the deviation from the roundness. In horizontal sections, it is possible to produce smaller details than in vertical sections. With horizontal samples, the minimum peak to valley Rz was 0.086 mm when the maximum difference Rz was 0.271 mm and the mean value for Rz was 0.165 mm. For vertical samples, roundness increased greatly when larger features were manufactured. The minimum peak to valley Rz ratio was 0.388 mm and the maximum Rz was achieved at 0.882 mm. These large values are explained with sagging effect at the top of the hole. The sagging effect of AlSi10Mg is clearly visible on vertical builds in figures Figure 82 and Figure 83 for the extreme case of small details and for large details. Moreover, the push of melt pool by scanning strategy effects on the features as Figure 82 in horizontal build indicates.

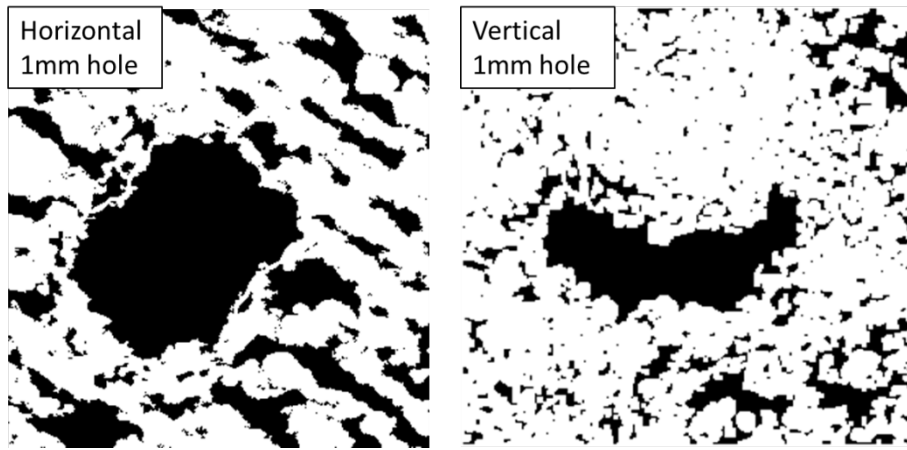


Figure 82. 1 mm diameter hole from horizontal build (left) and vertical build (right)

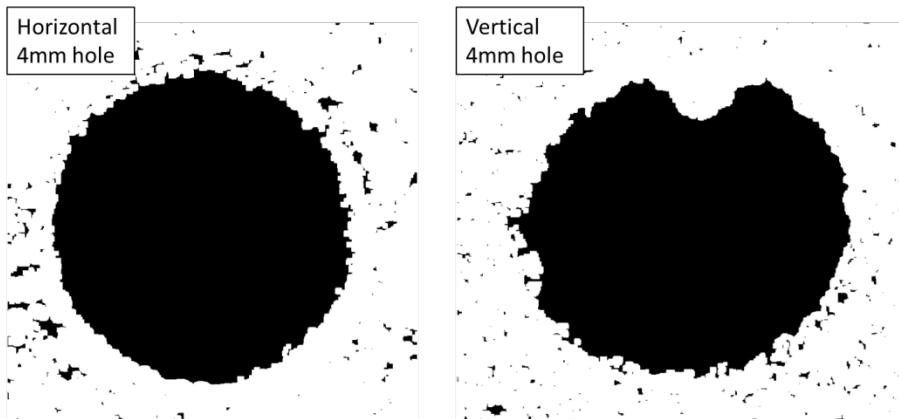


Figure 83. 4 mm diameter hole from horizontal build (left) and vertical build (right)

3.3.3. Design of tubes

In order to investigate the internal surface roughness in more detail, a cylindrical hollow geometry for internal channels was designed and built. The tube is aligned with different building angles with respect to the building plane (Figure 84) and the design took the shapes of hydraulic tube components shown in Figure 85 and Figure 86. Materials used were AlSi10Mg and Ti6Al4V alloys supplied by EOS for LPBF. The internal surfaces of the channels produced were analysed optically and with a surface roughness tester to evaluate the effects of the building angle.

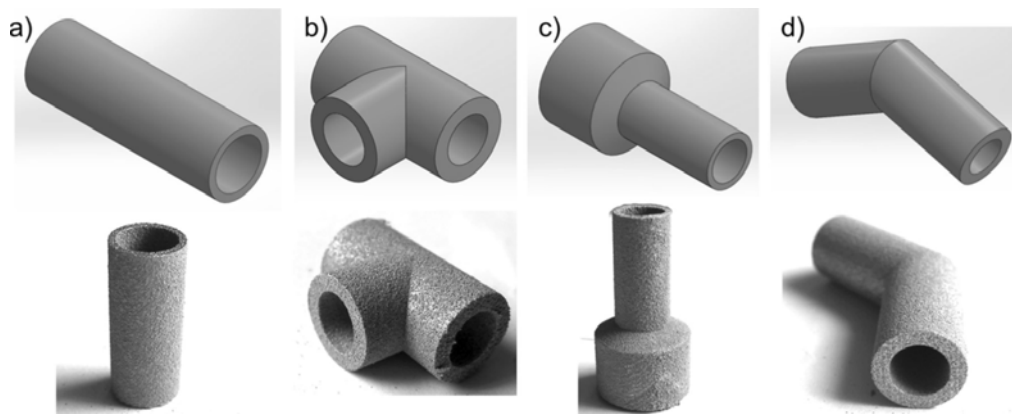
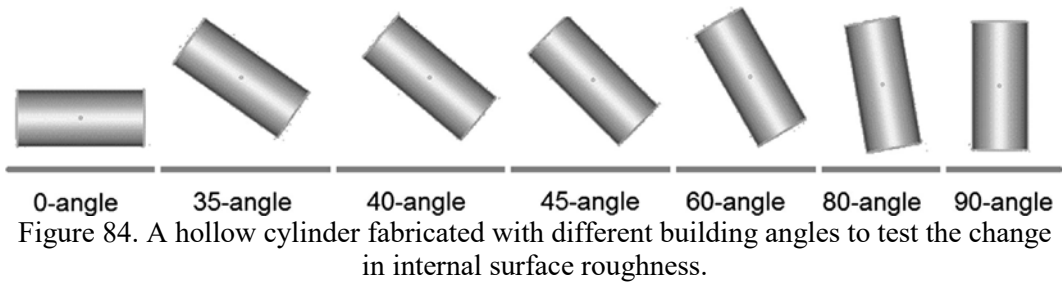


Figure 85. Manufactured hydraulic component shapes from AlSi10Mg and Ti6Al4V.

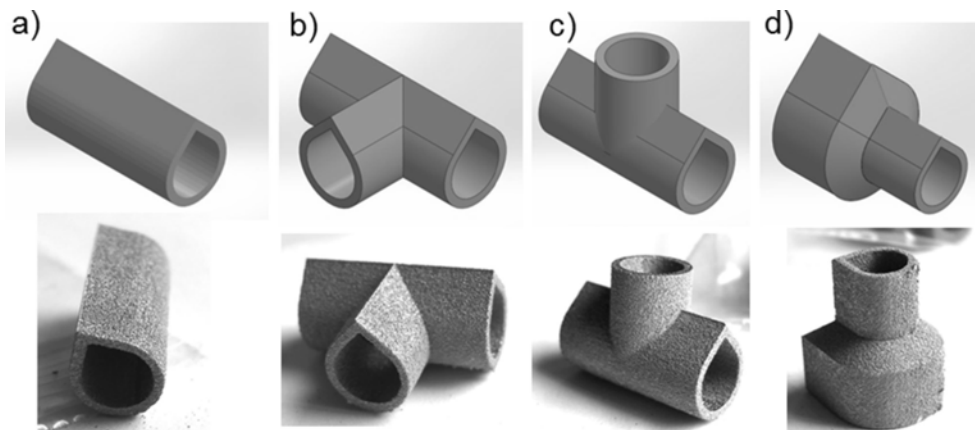


Figure 86. Manufactured hydraulic component shapes from AlSi10Mg and Ti6Al4V at 0-angle.

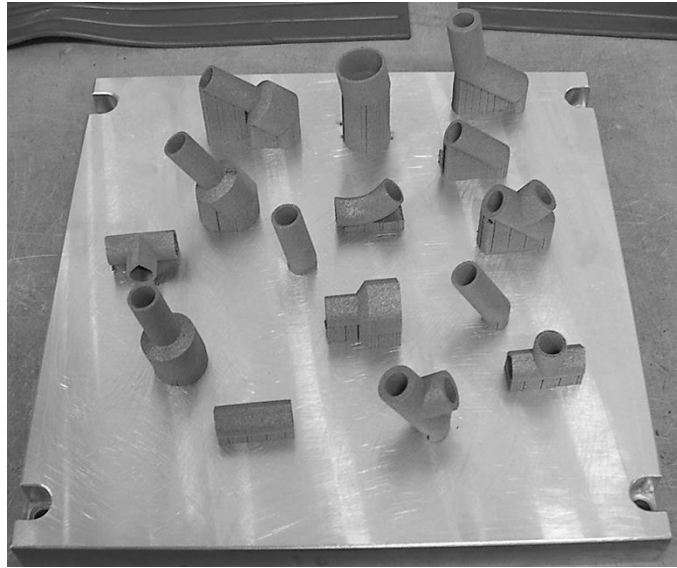


Figure 87. Tubes manufactured from AlSi10Mg in different angles.

As already stated, the use of LPBF allows design and manufacturing freedom that traditional machining processes cannot give. These benefits are for example internal cooling channels in dies and lighter components. Internal channels benefit especially for hydraulic components with the ability to create desired flow paths inside of a block and make the components lighter. The knowledge of internal surface structure assists the design and orientation of the part for the building.

LPBF parts have high surface roughness in the so-called as-built conditions in comparison to machined parts. This is a drawback for all AM methods for metals [99]. In a previous study Calignano et al [43] demonstrated that on AlSi10Mg top plane surfaces, the roughness was reduced using optimized parameters and shot peening from $R_a=24\text{ }\mu\text{m}$ to $R_a=6\text{ }\mu\text{m}$ [43]. However for regions where support structures are placed, they have higher roughness: this could be due to the fact that the support structures penetrate some layer into the piece. In the ideal case, it would consider having no support structures at all. Using internal channels in as-built condition is possible with hydraulic tubing according to [100] and [101] where it was investigated for robotic application. The surface roughness of additively manufactured piece outside varies depending on a fabrication material [68] [102], main process parameters [103] [43], particle size and distribution and the AM method [102] in use. Considering materials in LPBF, titanium has higher building accuracy in build radius than aluminum, but poorer behavior in overhang [68].

External roughness has been characterized in previous studies [102] [43] with different materials e.g. AISI 316L, Ti6Al4V, and AlSi10Mg. The layered structure and the effect of contour translated into steps affect high roughness. The powder is trapped and partly molten on the steps of the contour. In addition to

contour, unsupported overhang is a problem since particles are stuck on melt pool and solidification shrinkage bends the structure out of place. Depending on the angle of build the particle size and density of these joined particles on the surface varies. Inside and overhangs of the design, some powder tends to stick to the sides with bigger agglomerates. Cut internal channel surfaces have visually different appearance when comparing an up-skin and a down-skin. The visual appearance has a strong connection with the building angle of a piece. These slight differences are characterized in the research.

The external dimensional accuracy was measured by measuring roundness from all of the specimen bottom and top in stereo micrographs by fitting an ellipse as described in the previous chapter. The roundness was near one as well as major and minor axes aspect ratio was similarly close to one meaning that the tubes don't have external distortions. This fact excludes the build direction 0 as it has a different design with 45 degrees angled slope on the top. It was also without noticeable distortions. A decrease in dimensional accuracy was noticed within the surface where a reduction piece with diameter 20 mm is reduced to a diameter of 10 mm (Figure 88). At 40 and 45 degree builds the bottom diameter aspect ratio (minor/major axes) was decreased to 0.94 and the difference between axes was 5.5%.

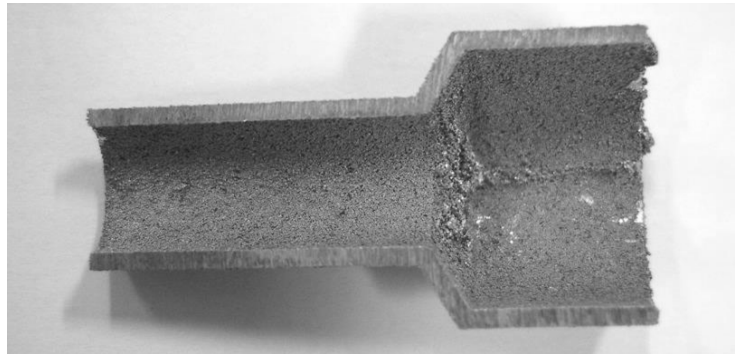


Figure 88. Unsupported bend in dimension reduction part of a piece leading to sagging effect on the piece.

Halves were cut horizontally from the middle to reveal top internal surfaces built with down-skin parameters and bottom internal surfaces produced with up-skin parameters. Both top and bottom surfaces have different evolution structures depending on the build orientation. On the top half 0 degree consists of 45-degree incline that joins together. This joint has dross formation that is similar to slight cave in of unsupported top surface and the size of the cave in less than 600 μm (Figure 89a). Top surfaces from 35 to 40 degrees have similar roughness microstructure (Figure 89c) consisting of dross formation and larger clusters (diameter 150 – 250 μm) of fully and partially molten particles. When the top half reaches 45-degree build angle the surface structure changes from large particles influenced from dross formation to smaller particles (diameter 100 μm) with

powder filling the gaps. Top surfaces built with 45 to 60 degrees build angles (Figure 89c, e) have resemblance in particle size. With 45-degree angle there is more powder attached as satellites on the particle surface than at 60 degrees. The next change is when the build angle reaches 80 and 90 degrees. In those angles, both bottom and top have a similar surface microstructure with less unmolten powders and more melt lines visible. All the surfaces trap little quantity of unmelted powder: therefore for some precision applications, like hydraulic manifolds, it is necessary to perform a post-treatment like shot peening to remove all this loose powder.

Bottom halves of the internal channels have distinguished and different appearance than the top halves. In the 0 angle build, there are original scanning lines visible and the first steps from the contour layering. This bottom surface is smoothly affected by the waviness of the scan tracks. As the building angle increases the bottom surface will develop waves of molten structure similarly to staircase and between these lines there are partly molten particles sintered. After 45 degrees build angle the bottom surface microstructure resembles the top surface. In the angle between 45 and 60 degrees, the roughness measurement shows a change in the surface roughness values between top and bottom. The top becomes less rough as the top.

The surface of Ti6Al4V is more heterogeneous than the surface of aluminum on 45-degree build angle. The top surface has small spherical particles stuck on it. The bottom surface consists more of molten waves inheriting the layers positions.

The surface roughness in AlSi10Mg between upper and lower part (Figure 89) changes depending on the build angle and the surface structures start to resemble near 60-degree build angle. There is a change recorded between 45 and 60 degrees that the upper part will have a slightly lower surface roughness in comparison to the bottom. This change is due most likely to the changing in contour and 60 degrees. With a 60-degree angle the steps become higher than wider and it will reduce the energy leaked into the powder bed. In AlSi10Mg larger angles than 60 degrees lead to fewer differences in the top and bottom surfaces. Notable the staircase effect and scan lines are visible on all the 0-angle build bottom surfaces (Figure 89b) revealing effective laser spot size of 80 μm .

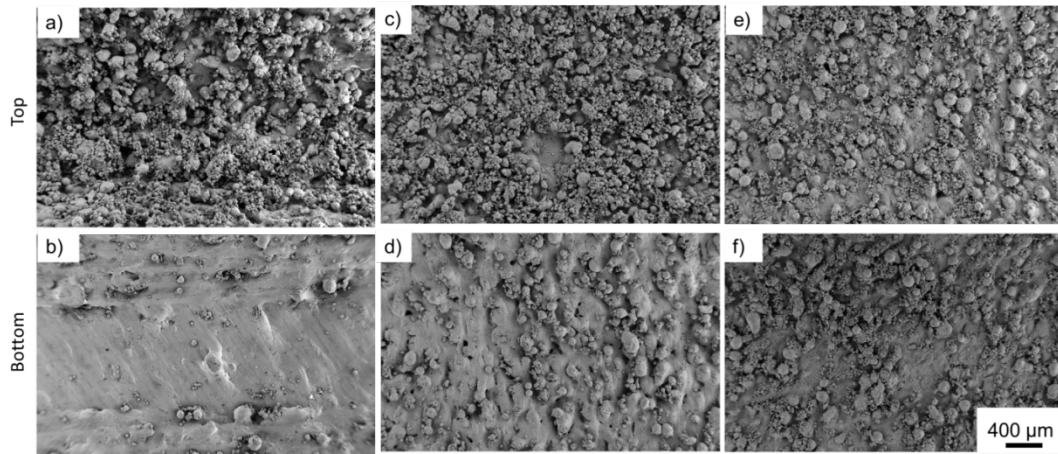


Figure 89. FESEM image of the internal surfaces of the cylindrical shapes produced by SLM with different angles: a) 0 angle top, b) 0 angle bottom, c) 45 angle top, d) 45 angle bottom, e) 60 angle top and d) 60 angle bottom surface.

Changing building angle is shown in Table 10 with the roughness values. These changes are visualized in Figure 89 where are the major changes. During roughness measurements, the surface is not always flat or wavy, but consisting of clusters of fully and partly molten particles joined together. FESEM Figure 90a is from 0-degree build and it has relatively flat surface from where a black line is the path of the roughness measurement probe. Similar place of measurement is found in Figure 90b from a build with a 45-degree angle. Figure 90b shows a problem with surface roughness measurements: the darker measurement track not so optimal, since the probe has travelled from high pillar down to the valley. When the measurement line is not continuous it is not ideal for measurement and the cuts in measurement line can affect to the measurement accuracy by not being able to measure the full effective peak to valley ratio. The average difference in R_a between these two surfaces is measured to be $7\text{ }\mu\text{m}$. This can explain why the average measured roughness R_a is near $20\text{ }\mu\text{m}$ in all the measurements and has a big error bar (Figure 91).

Measurement results are reported in Table 10 and graphically in Figure 91. In Figure 91 the homogenization of the surface affects the bottom and top roughness to meet and stabilize in the same roughness area as seen earlier with the microstructure.

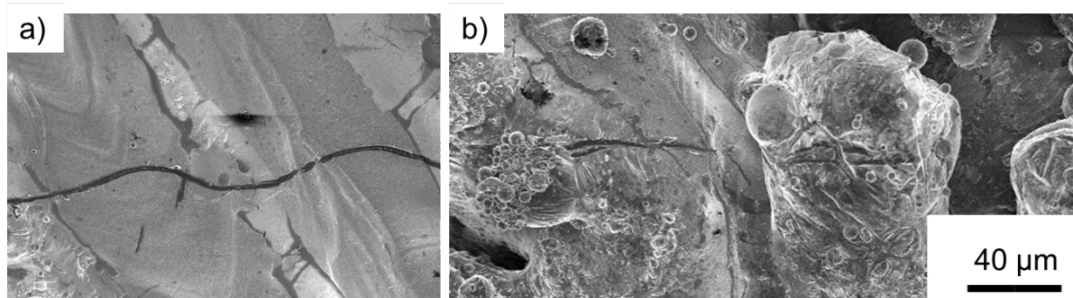


Figure 90. Dark stylus tracks representing the surface roughness tester indentation on internal surfaces: a) 0° angle bottom and b) 45° angle bottom surface with not optimal stylus path.

Table 10. Roughness measurements from samples (μm).

degree		Ra	st.dev	Rz	Wa	Rmax
0	Bottom	13.6	2.9	64.2	18.1	91.1
	Top	21.6	3.4	107.4	33.3	128.4
35	Bottom	19.0	1.8	90.9	12.5	121.3
	Top	22.5	3.8	100.2	12.4	128.5
40	Bottom	20.1	4.2	96.6	17.2	129.1
	Top	22.8	2.8	111.8	27.0	150.0
45	Bottom	20.2	2.4	88.2	17.7	131.8
	Top	21.7	3.5	102.4	21.4	135.7
60	Bottom	19.8	1.5	97.9	20.7	129.0
	Top	18.5	1.4	104.3	20.1	112.5
80	Bottom	20.9	3.0	99.6	17.7	128.5
	Top	18.9	1.8	90.0	16.8	113.0
90	Bottom	19.2	2.1	105.6	16.2	173.5
	Top	20.9	1.7	120.4	17.6	168.7

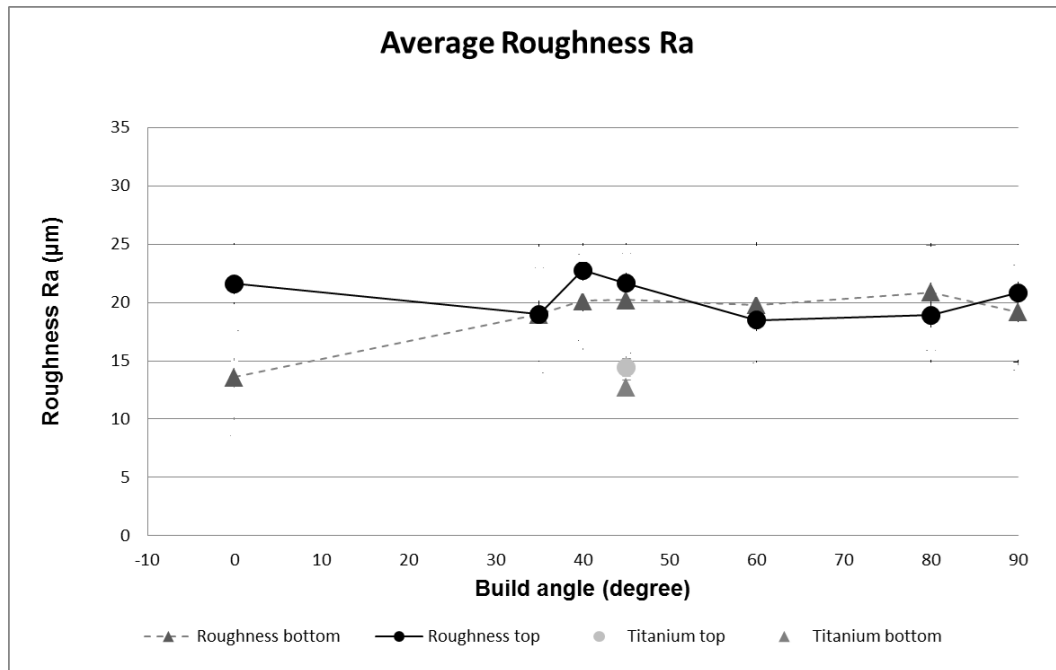


Figure 91. Roughness measurements on AlSi10Mg and Ti6Al4V internal surfaces

Cross section roughness is taken to check the roughness profile in 2D plain and the maximum peak and valley difference. These differences are checked from the perpendicular cross section. All cross sections show roughness peak to valley average from 100 to 200 μm pointing out to the direction that minimum roughness achievable in internal channels as build condition with LPBF of AlSi10Mg seems to be 2 – 3 times of the powder diameter and it is affected with the staircase effect [102]. Improving staircase effect modification of layer thickness would be needed. It is evident from the cross sections that the roughness is mainly considered from partly molten particles and sintered powder stuck to the surface. Figure 92a is a bright field cross section displaying the polished cut line. Large particles are on the surface covering it with cavities. Figure 92b is a dark field of the same image and it is possible to see further on the surface. There are different sized particles sintered on the surface. The bright spots on the Figure 92a are particles connected to the surface.

The cross-sectional roughness measurements are in agreement with stereo microscopic and roughness measurements indicating the same behavior of surface roughness profile: a change between 45 and 60 degrees build angle from higher top roughness to higher bottom roughness. Figure 93 is a comparison of the optical cross-section roughness and Rmax top to bottom values measured. Rmax measurement values are lower with small build angles that might be based on the effect observed in FESEM micrographs (Figure 90) where the stylus is not being able to travel top to bottom efficiently.

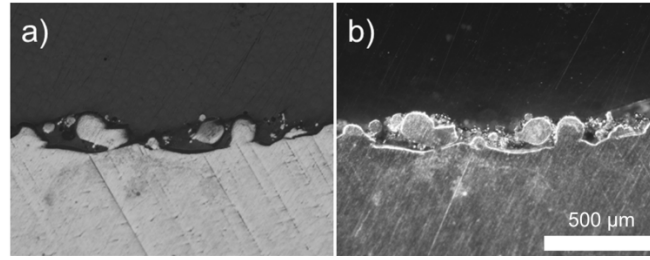


Figure 92. Difference in cross-section roughness between a) bright field and b) dark field images. Dark field shows the surface structure below the cross section.

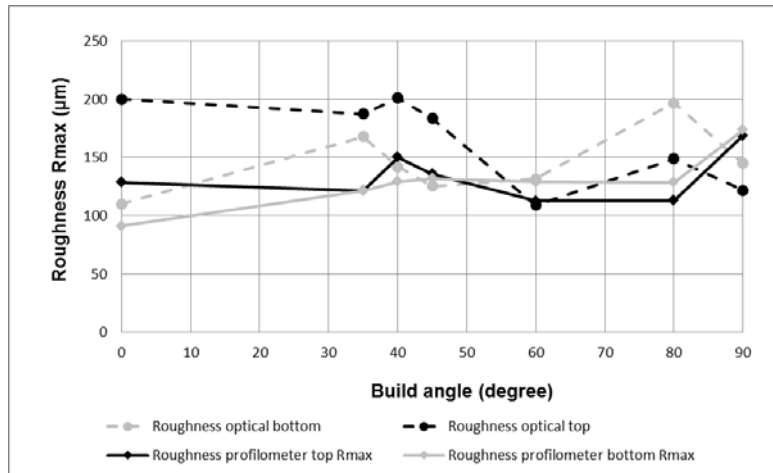


Figure 93. Comparison of measured Rmax and cross-section peak to bottom measurements.

Four different shapes (Figure 85) commonly used in hydraulic components were designed and fabricated with LPBF. The shapes were built in AlSi10Mg with building angles of 0, 35, 40, 45, 60, 80 and 90 degrees. Ti6Al4V parts were manufactured with 45-degree build angle. Build shape on the XY-plane, so parallel to the building platform, was redrawn to resemble a teardrop, as suggested in design for AM literature [66]. As for the holes, the pieces were analyzed with stereomicroscope and image analysis to check their dimensional accuracy. In funnel part shape fabricated with 40 and 45 degrees, deformation was noticed. Samples were then cut in half horizontally and the top and bottom surfaces were examined with stereomicroscopy, roughness tester, cross section and FESEM.

It could be stated that surface roughness of AlSi10Mg internal channels evolves depending on the building angle. The top surface of the internal channel until 30 degrees has to be redesigned to have self-supporting properties. Angles from 35 to 45 degrees show rough and big particles. From 60 degrees onwards the top and bottom surfaces differences get smaller and the top surface is smoother than the bottom. Internal channels bottom surface on xy-plane show smooth surface with visible scan tracks. As decline increases the stare case effect affects the surface roughness. Surface roughness measurements have an average of Ra 20

μm with large error $\pm 5 \mu\text{m}$. The error in measurements can be the effect of the probe not being able to travel efficiently to peak and valley. This is supported by the FESEM images and cross sections showing cluttered surface. The building angle with staircase effect with the resolution of the machine will affect the roughness. The residue of stairs can be noticed in the position of joined particles on the surface. On the top surface, the excess energy leaked into the powder bed increases small particle capture on the surface, however, not affecting the base roughness. Titanium has better dimensional accuracy and smaller surface roughness than aluminum. With titanium, the roughness measurement deviation is considerably less than with aluminum.

3.3.4. Design of Hydraulic Components

Design of a successful build is not straight forward process and needs understanding from the build method. Different machines with higher and lower energy might work differently. Physical properties of the manufacturing method are still similar within the LPBF manufacture method and these results can be elaborated into different machinery with caution. Alongside the method and machinery, the build quality depends highly on factors deriving from correct orienting of the piece to not have distortions in moving joints or shapes and angle of overhang. The results obtained during the Ph.D. are presented as design suggestions for LPBF, considering also the materials.

A simple hydraulic system consists of a hydraulic pump, a control circuit, pressure lines, a hydraulic actuator, return lines and suction lines. In pressure lines, the pressure and the velocity of the fluid are the highest. A small tube for hydraulic line raises fluid velocity, that effects to the whole system, causing frictional losses and turbulence by the fluid [104]. The internal roughness of the tube might also cast its effect on drag of the fluid, but according to [100] the smoother design by additive can even enhance the flow of hydraulic fluid. Results of bad flow are pressure drop elsewhere in the hydraulic and heating of the fluid. The higher heat of the fluid can accelerate wear of moving parts and aging of hoses and gaskets. The right design choice is important for the component life and the performance efficiency of the hydraulic system [104]. Hydraulic systems and electronic systems are used in control systems in aerospace industry and robotics, where reliable operation is needed. Hydraulic control systems are used e.g. for hydraulic actuators controlling large pieces e.g. flaps of an airplane [105]. In solutions that require light weight it is beneficial to cut away as much weight as possible in order to increase efficiency. The pressure in pressure line is often around 200 bars, but in the unlikely event of a malfunction the line has to withstand pressures up to 400 bars. Special attention needs to be given to hydraulic fluid at low-temperature applications as the fluid itself is corrosive. Highly inert materials as stainless steel and aluminum are often used in conventional hydraulic piping. Usage of AlSi10Mg as aluminum alloy is considered in this study: it is well known and studied for LPBF, as deeply

reported in literature [43] [101] [102] [106] [107] [108], thanks to high fluidity of the liquid phase that makes easier the preparation of pore-free samples.

However, there is a large potential for AM with aluminium alloys especially for hydraulic components, since it has several advantages over titanium:

- Lower cost: aluminium alloy powders (e.g. AlSiMg) are on average around 4 times cheaper than titanium powder (e.g. Ti6Al4V);
- Higher thermal conductivity [109] [110]: AlSiMg has a thermal conductivity of 103-119W/mK, compared to 6-7W/mK of Ti6Al4V. It is therefore very suitable for hydraulic components since it helps to dissipate heat in a distributed manner;
- Lower density: AlSiMg has 2.68 g/cm³ vs. 4.41 g/cm³ in the case of Titanium Ti64; easier to post-process, e.g. for adding threads or polishing surfaces.

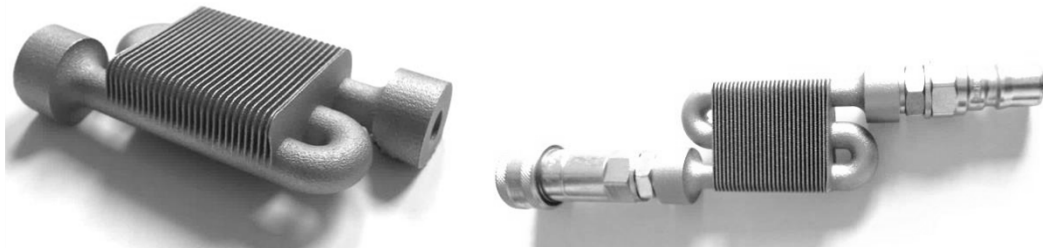


Figure 94. The two S-shaped aluminum manifolds made by Direct Metal Laser Sintering (DMLS): just after shot-peening (on the left), and after testing with pressurized oil (on the right).

As proof of concept and a pre-study of LPBF hydraulic parts, an S-shaped hydraulic tube is designed (Figure 94). The strength of the design is analysed with a numerical FE-model for the part to handle the stress induced by 40MPa of hydraulic pressure inside the tube. Design usage pressure is 20 MPa so the calculations have a safety factor of two. From the design, two S-shaped hydraulic manifold (Figure 94) were fabricated from AlSi10Mg.

Stress relieving treatment in 300°C for 2h in air (EOS standard stress relieving for AlSi10Mg) was performed to gain the mechanical properties. After stress relieving parts were detached from a building platform and the parts were shot-peened for better surface quality. Shot peening was not performed inside the tube. The aluminium manifold was cut half in as build condition as well as after being tested with the hydraulic fluid. The section of the manifold after the shot peening (Figure 95), with the indication of the areas observed with a stereomicroscope. Areas examined (Figure 95) are 1: the inside cavity (Figure 96) that is reachable with full reach of shot peening. 2: the middle of the manifold (Figure 97), that is out of the reach of shot peening. 3: the corner of the manifold (Figure 98), where it might be possible to reach with shot peening and the hydraulic fluid will induce drag. The black arrow on the spot of Figure 95 shows

the direction of the image from the larger figure. Both as-built and tested with oil manifolds are examined the same way and the same positions.

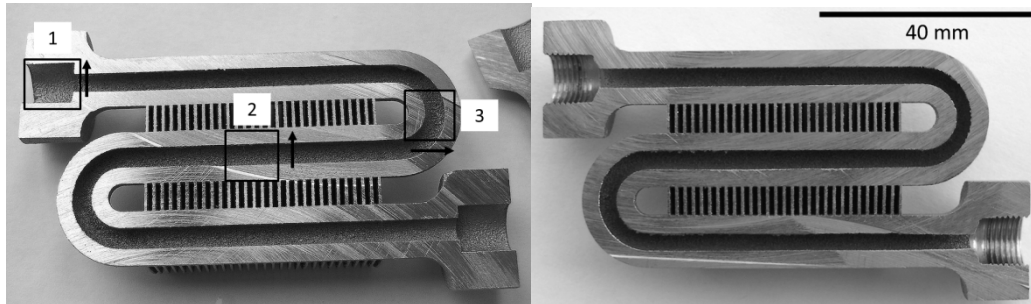


Figure 95. Internal channel of the manifold (left: as build, right: tested with oil) and the stereomicroscopically examined spots: 1. Fixing cavity, 2. Inside channel and 3. Curve.

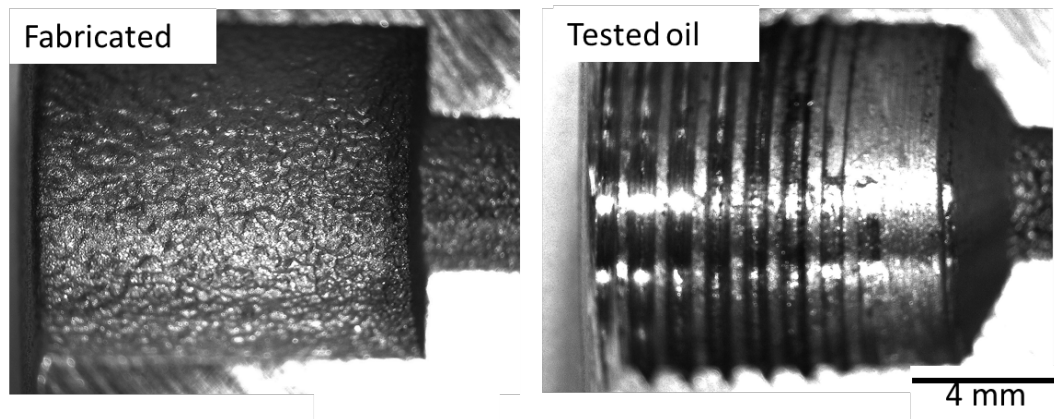


Figure 96. Inside cavity reachable with shot peening and machined with threads.

The inside channel of the manifolds is as designed. Between the two states of usage visual differences are scarce as the fabricated piece and the piece tested with oil visually look similar. The comparison is shown in Figure 97 from inside of the cavity's long and straight part and Figure 98 from the corner of the bend in the manifold. The corner of the bend has collected clustered powder particles as the heat input in the inner corner have been a bit higher.

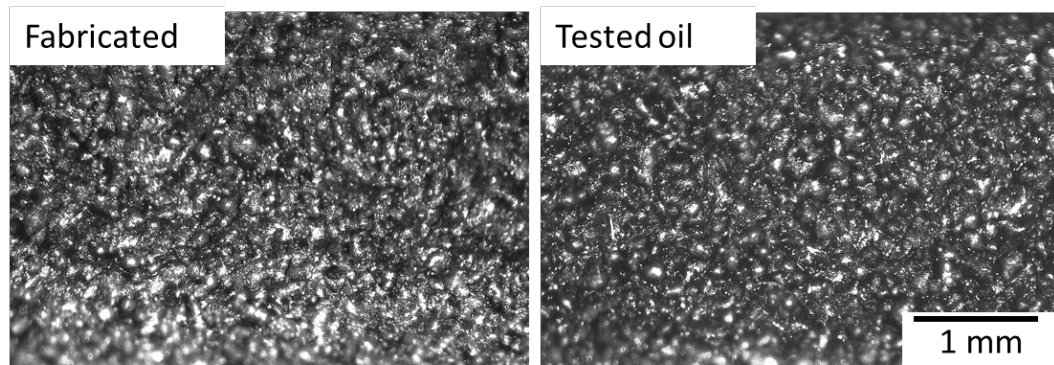


Figure 97. Inside channel of the manifolds: after shot peening (on the left) and tested with oil (on the right).

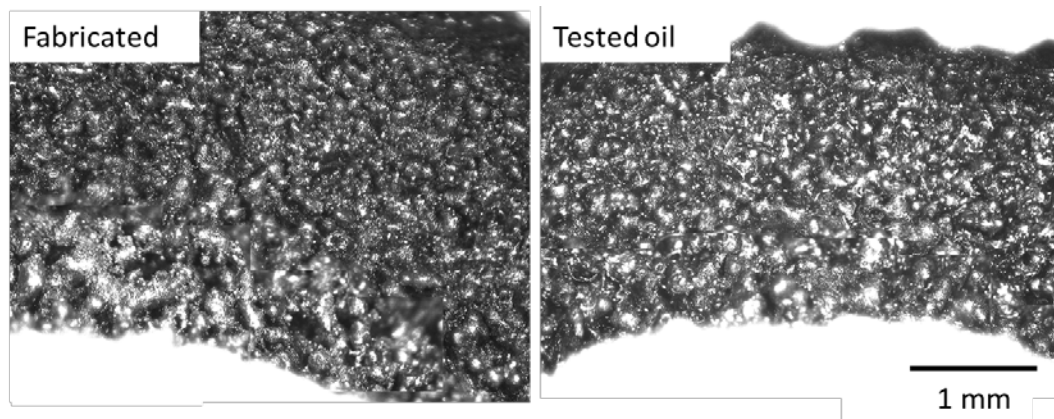


Figure 98. Corner of the manifolds: after shot peening (on the left) and tested with oil (on the right).

HyQ2Max robot is a quadruped legged robot from Istituto Italiano di Tecnologia's Genoa [111]. It has hydraulic actuators, and for these the weight could be a problem. For this application, AM-hydraulic manifold was designed (Figure 100) to save in weight and size and to add in functionality. The robot has three hydraulic actuators that are supplied with hydraulic fluid through a pressure supply and return line. These hydraulic manifolds need to be close to the frame of the robot in order not to affect weight balance negatively. Image of the HyQ2Max robot and the final position of the hydraulic manifold is shown in Figure 99. [112]

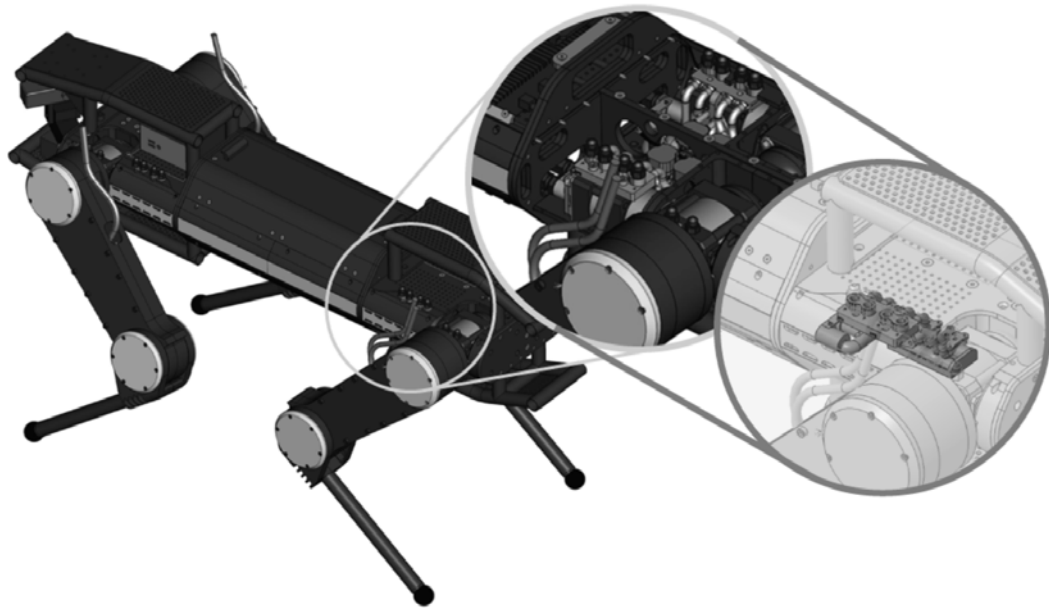


Figure 99. CAD model of HyQ2Max with close-up views of the highly-integrated hydraulic manifolds of the two hind legs. [100]

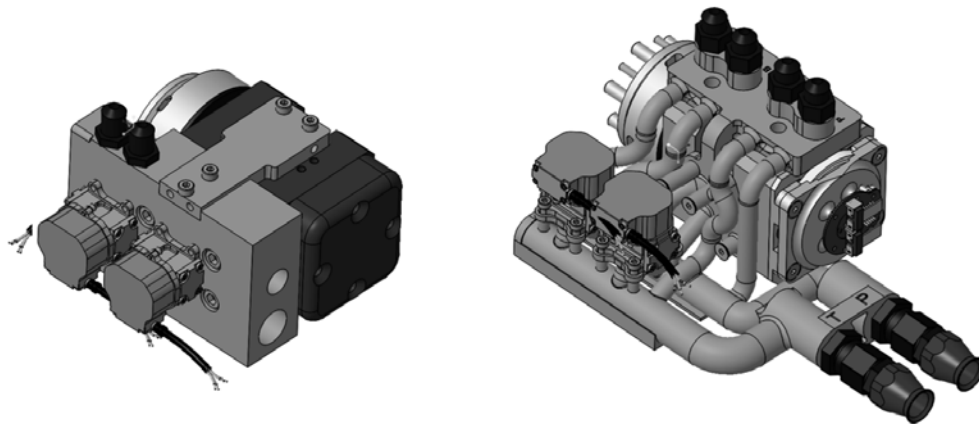


Figure 100. CAD models of hydraulic manifolds for the legs of the HyQ2Max robot. Left: traditionally manufactured manifold (green parts). Right: highly integrated AM manifold. [100]

By building near net shape features and parts used as it is, it is important to maintain accuracy and avoid distortions. Inserting support structures inside of tubes is not possible to maintain achieve the outside shape. Therefore, the structure needs to be self-supporting such as an overhanging structure. For AlSi10Mg self-supporting structures Calignano et al. [68] reported that build

angles larger than 30 degrees are feasible to manufacture as an overhang. Unsupported top layers are molten on powder that then causes the melt pool to sink deeper into the powder bed leading to dross formation and sintering unmolten powder on the part. This phenomenon has a negative impact on the circularity, surface roughness and accuracy of the internal cavities. However, after 45 degrees build angle the dimensional accuracy does not suffer from extensive dross formation by the powder as seen in Figure 89. The best positions for internal channels are high angles and close to 90 degrees relative to the building platform. These positions might not be possible to achieve as parts have complex geometries. There might be vertical sections that might be needed to be redesigned with an ellipse or angled shape to make it self-supporting. Other times a simple reorientation might be a solution.

The orientation of 45 degrees (Figure 101) was chosen for the production of the hydraulic manifold. In addition to this, an angle of 15° is added between the recoater blade to soften the spreading of the powder on the powder bed while building. Figure 101 c&d show the use of support material in Materialise Magics and after the build. Shot peening clears the dark grey feel of the part and makes it shiny. The manufactured and finished manifold (Figure 102) was tested and mounted successfully for the design pressure of 20 MPa.

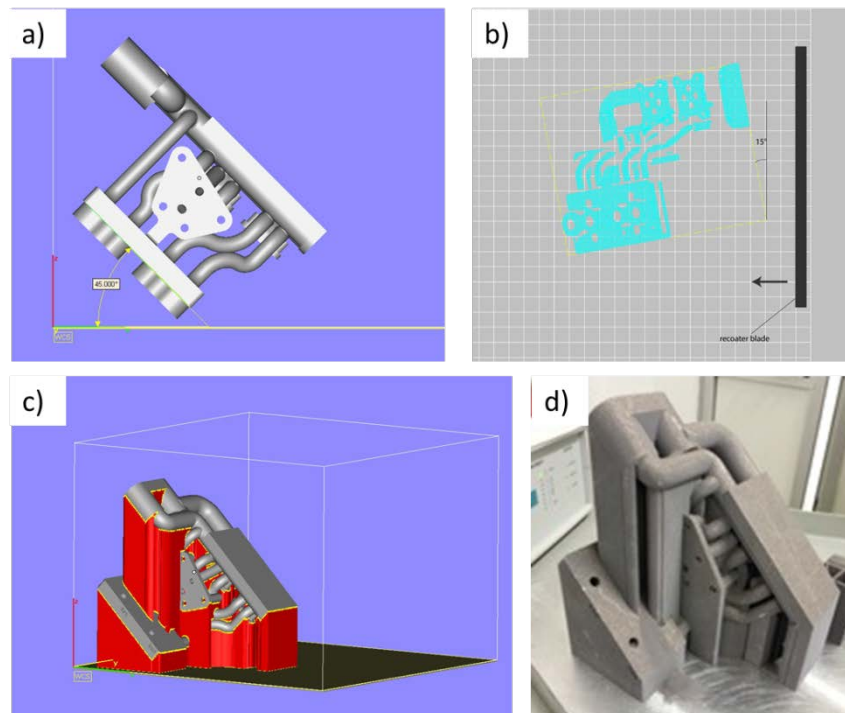


Figure 101. Orientation of hydraulic block a) 45-degree slope, b) 5-degree tilt for recoating blade angle, c) hydraulic block with support structures in Magics 18 and d) the final part.

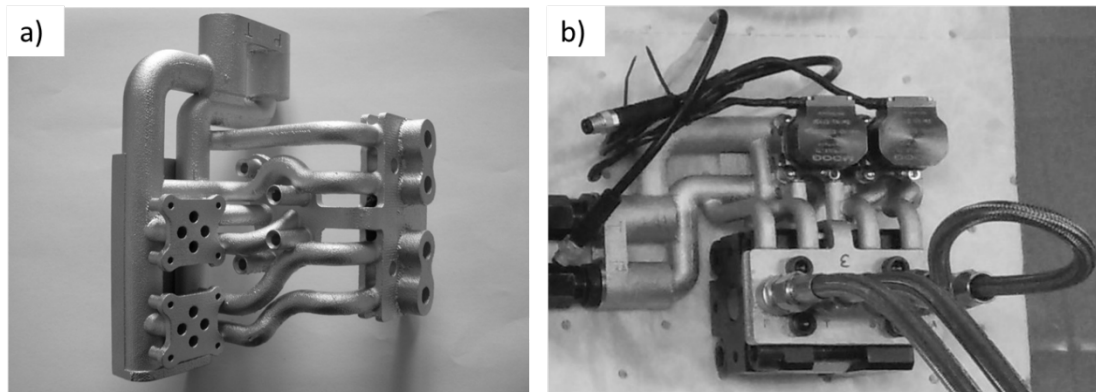


Figure 102. The hydraulic manifold a) after shot peened and b) during pressure testing.

The main advantages of the AM produced manifold could be summarized as follows: it changed the design from traditionally manufactured part (e.g. drilling) to light weight and tubes flowing naturally avoiding e.g. 90-degree bends; the AM manifold weight 313 g whereas the same functionality from traditional manifold weights 520 g. It allows saving 39.8 % in weight for one part, and therefore for all four parts, it is possible to save 828g.

3.3.5. Summary

Process driven design is limiting the design freedoms in manufacture. Knowing well the manufacture process allows the full utilization of the process. In metal AM the achilles heal is the process itself needing support structures as founding to be able to build on. These supports need to be strong enough to carry residual stresses deriving from new layers. It has to be also accessable to be able to remove from the part. To reduce support structures or to be able to build without those the knowledge of overhangs were investigated.

Dimensional tolerances showed in case of holes manufactured from AlSi10Mg that the surface roughness is in range of 100 μ m. This is 3 times of the powder size. The surface roughness consists of particles sintered on the surface, scanning lines and discritisation of the shapes. This affected into small holes by reducing circularity and accuracy where as in larger holethe effect of surface became smaller.

Gravity and the build orientation concluded a great deal into the accuracy. When building 90° angle from base plate small features were possible, the same features at 0° were not. This was shown eith 0.5 mm diameter holes, where 0° hole was reduced into a line. Larger holes than the diameter 0.5 mm were having trouble of keeping the shape as the arch of the cirle sagged downwards. Gravity pulls the unsupported roof lower before it could support itself. Due to this behavior higher agles inside of closing cavities are necessary i.e. tier drop or elliptical shape.

The accuracy of these design guidelines were investigated in longer sections of tubes. Top and bottom sections were analysed and compared. It was noticed that the collapsing of roof is angle related. Different build angles correspond into their own surface structures. The surface structures are formed from scanning strategy and slicing parameters of the part. For example in a tube build on 0° , there is visible scan lines and stair cases on the bottom where the curvature was simplified as flat. Where as on the top side there was small extrusion from penetration of the laser. When examining different angles, it was noticed that these top and bottom surfaces become similar when a threshold value is reached, in case of AlSi10Mg it was 60° .

A complex and large part is difficult to manufacture. It will not be possible to make the perfect orientation due to limitations. These can be build chamber size, critical features (e.g internal channels), melt area size of single layer or possibility to support it. In the hydraulic manifold the crucial factor was chosen to be the internal channels. These channels were support free and the whole part was made in the orientation because of this choice. In the part some angles in internal structures were not so optimal as well as melt pool evolution leading to large support structures around the part. However, due to knowledge of the process it was possible to manufacture hydraulic component what was lighter than conventional part almost 40%. In robot application where center of gravity is important this brought additional benefits.

Chapter 4

4. Conclusions

Design is an integral part of any object. On paper and in imagination it is possible to create breathtaking imaginary shapes similar to Gaudi's molten clocks or Da Vinci's 2-dimensional paintings that seem to have the 3rd dimension. Computer-aided design has changed the landscape of design from 2D space to 3D space and allowing reproducibility of the design. Once a design is completed it can be copied and reproduced without needing a master designer or artisan. Computer-aided manufacturing methods like CNC milling and now additive manufacturing (AM) have brought a new wave of change into the design. The cost of a CAD software and computational power is not an issue anymore with free to use open source CAD software. The AM has taken away the need of knowing how to manufacture a part oneself as it is enough to know how to design and the AM-machine does the rest.

Conventionally there have been limitations on what can be manufactured. These design limitations derive from constraints of manufacture, material properties and the forces affecting during and after the build. AM has brought a disruptive force into the equation with additive thinking instead of subtractive thinking. Where a part is machined from larger billet and a cast is made in a pre-carved cavity, additive manufacturing is made layer by layer where only the necessary material is used. This allows less material to be used and pushes the trend into less and less material as the cost of material works as the driver for this direction. The less input material, the more is saved and the lighter is the piece.

Product-driven design comes from the possibility of manufacturing with various methods and with fewer constraints. The product can be designed for its functions and the production aspects do not need to consider. This allows the most efficient or the most eye-pleasing object to exist. Topology optimization is one

method how this can be achieved. It is possible for a master in their field to make a beautiful design with optimal shape after several tries. However, when a shape becomes more complex, boundary conditions and loading cases multiple, the design will not be so easy to understand as people rarely see through glasses of stress distributions, heat patterns, and flow models. Therefore, computer-aided optimization will be able to do the work aid in making the design. Topology optimization offers an automated way to calculate large-scale problems from the product-driven design aspect.

3D printing with polymers offers greater design freedom than AM with metals, as with 3D printing multiple materials can already be used. This is true in fabrication methods like material extrusion or ink jetting. Usage of different materials allows combining the properties for sacrificial material in case of the final shapes that will be necessary during the build. This sacrificial material can be chemically dissolved providing the final functional shape. Even if the support structures are not needed as in case of Laser Sintering (LS) as the powder is supporting the part, some compromises might be needed. In LS the compromise is a hole and a tab where it is possible to empty the excess powder from hollow cavities. Already these additions have created a shift from product driven design to the middle ground towards process-driven design with the support structures. As powder bed AM methods are not flexible enough to be able to manufacture with multiple materials, there are more compromises. With metals these compromises come in support structures made to anchor the structure into the build platform, they distribute heat away from the part and keep the structure intact without deforming during the build. A second step in manufacture post-treatment is aimed to remove the process design, that allows the part to be built, from the final design of the part.

In this thesis, the application of topology optimization without production constraints was investigated. It is noted that in itself the optimization is a mathematical model that cannot be implemented directly into manufacturing stream. Commercial software packages are developed and those could help the designers to utilize this powerful tool. The commercial software still lacks many features that can be utilized in the normal algorithm and often will produce results in various qualities. There is still the need for the expertise of the designer to take full advantage of the software potentials. All the materials and methods are not suitable for achieving the designs gain from topology optimization and the more heterogeneous the material properties gain from AM process the more difficulties there will be in achieving functional parts. In addition to these points, process dependent parameters as building angle and supports need to be added into a model with the knowledge of the expert. The design choices made by the producers will affect the quality of the part in ways of features, anisotropy and surface quality as found out in studies.

Topology optimization was applied with two different AM methods: LS and material extrusion. In the consideration of the optimization, the material datasheets of the specific methods were used as source data. The investigations found anisotropy to play a big role as well as the material boundaries in fracture mechanisms. It is possible to gain strength as expected through calculations, however, due to the anisotropy only in best orientations where the layer defects are not under load. AM methods are individual and what will work for one manufacturing method better, might not work for another as was noticed when comparing LS and material extrusion.

Design rules for metal additive manufacturing are considered through hole and internal cavity studies. What are the shapes that can be made without losing in dimensional accuracy? The hole study revealed with AlSi10Mg the possibility of manufacturing small holes without support structures. The smaller the holes, the larger the surface roughness and the distortion from the gravity and. The knowledge about the holes was used to create larger internal channels as needed in cooling channels for dies and hot temperature applications. It was found out that 0, 45 and 60 degree building angles have different surface morphology for AlSi10Mg. Large build angles give the most uniform surface structures as build status when in lower builds the top and bottom surfaces have a different appearance. A large hydraulic manifold was oriented and built for a hydraulic robot, where light weight and mass centre were important factors. The orientation angle knowledge from internal channel study was used in orienting the hydraulic manifold in an optimal position without support structures in the channels and minimizing the surface roughness.

Additive manufacturing is not a new manufacturing method anymore and the leaps that have happened in the past years towards wider utilization are impressive. The knowledge about different AM methods is increasing and the demand will pull down the prices for the equipment and the materials. The design for AM needs a bit different state of mind than the current subtractive manufacture mindset. Many AM methods were used for this thesis and the mechanisms behind are explained. Sharing knowledge in this world is important.

Chapter 5

5. Recommendations for Future Work

Additive manufacturing is developing in a high pace. There is a new generation of AM machines coming out from different manufacturers and the manufacturing industry is pulling the utilization as well as pushing standardization forwards. It can be said that AM is maturing quickly. However, these advances does not come fast or painless. The pain is in the machinery to age and how to bring the new processes into market. Understanding of the AM processes help in learning and developing for the new.

The future developments can be sen in two different perspective: the process dependent and the product dependent. In process dependent design, the experience of AM needs to be made available into larger pool as the equipment becomes more common. Studies of accuracy, process parameters and the process helps to gather information to be able to use in the future endeavors. This is not a useless because the research should be done for every new machine with changed process condition e.g. enlarged build chambe size, nozzle or laser spot size. These affect the outcome but not the core process. Future work can be expanding the LPBF process from one machine into different manufacturers equipment and being able to compare the results from these manufacturers. Not all processes are the same when one uses hard recoating other uses soft.

In product design point of view more experience is needed. The commercial software aimed to join topology optimization and additive manufacturing are getting more common. There are collaborations between companies like Materialise (AM build processor), Siemens (CAD, CAE), Ansys (FE simulation) and Fürstentum (topopt) to join all the aspects of product design into AM

fabrication chain into a common software. These chains are not yet established to operate fluently. More research in integration on AM and topt is needed as the job is not simple. Further research in applying the tools, testing in both simulation and fabricated state in addition to publishing the gained knowledge will help the technological advance to further.

In topic of the thesis further research would be to use topology optimization algorithm into object. The case study II opened possibility to understand deeper the anisotropic nature of the failure. Using similar approach this can be applied to metals and optimization input parameters e.g. material properties.

References

- [1] Wohlers Associates, Wohlers Report 2015, Fort Collins, CO: Wohlers Associates Inc., 2015.
- [2] H. Kodama, "Automatic method for fabricating a threedimensional plastic model with photo hardening polymer," *Review of Scientific Instruments*, vol. 52, p. 1770, 1981.
- [3] "Reprap-project," [Online]. Available: <http://reprap.org/>. [Accessed 04 07 2015].
- [4] R. Larsson, "Method and device for producing three-dimensional bodies". Sweden Patent US5786562, 11 05 1993.
- [5] Arcam, "Arcam history," [Online]. Available: <http://www.arcam.com/company/about-arcam/history/>. [Accessed 12 03 2018].
- [6] American Society for Testing Materials, "ASTM International Committee F42," [Online]. Available: <https://www.astm.org/COMMITTEE/F42.htm>. [Accessed 18 05 2017].
- [7] International Organization for Standardization, "ISO committee ISO/TC 261," [Online]. Available: <https://www.iso.org/committee/629086.html>. [Accessed 2017 05 18].
- [8] Support Action for Standardisation in Additive Manufacturing, "SASAM standardisation roadmap june 2015," SASAM, Den Haag, 2015.
- [9] European Committee for Standardization, "CEN/TC 438 Work programme," [Online]. Available: https://standards.cen.eu/dyn/www/f?p=204:22:0:::FSP_ORG_ID,FSP_LANG_ID:1961493,25&cs=1DBC499E4A879D8D3D3862EB0C6702EE4. [Accessed 17 07 2017].
- [10] CECIMO - European Association of the Machine Tool Industries, "European Additive Manufacturing Strategy," Filip Geerts , Brussels,

16.06.2017.

- [11] American Society for Testing Materials, "ASTM F2792 - 12a - Standard Terminology for Additive Manufacturing Technologies," ASTM International, West Conshohocken, PA, 2011.
- [12] American Society for Testing Materials, "ASTM/ISO 52900 – Additive manufacturing – General principles: Terminology," Geneve, Switzerland, 2015.
- [13] American Society for Testing Materials, "ASTM F3187 Standard Guide for Directed Energy Deposition of Metals," 2016.
- [14] Norsk Titanium, "Norsk Titanium to Deliver the World's First FAA-Approved, 3D-Printed, Structural Titanium Components to Boeing," [Online]. Available: <http://www.norsktitanium.com/norsk-titanium-to-deliver-the-worlds-first-faa-approved-3d-printed-structural-titanium-components-to-boeing/>. [Accessed 18 05 2017].
- [15] European Union, "EUR-LEX Regulation (EC) No 216/2008," 20 02 2008. [Online]. Available: <http://eur-lex.europa.eu/legal-content/EN/TXT/?uri=celex%3A32008R0216>.
- [16] I. Stratasys, "APPARATUS AND METHOD FOR CREATING THREE-DIMENSIONAL OBJECTS". USA Patent US 5121329, 30 10 1989.
- [17] R. Jones, P. Haufe, E. Sells, P. Iravani, V. Olliver, C. Palmer, A. Bowyer, "RepRap – the replicating rapid prototyper," *Robotica*, vol. 29, no. 1, pp. 171 - 191, 2011.
- [18] Slic3r, "Slic3r Manual," Slic3r, [Online]. Available: <http://manual.slic3r.org/>. [Accessed 04 08 2017].
- [19] F.V. Miguel, C. Wilson, F. Santiago, C. Andres, "Effect of Infill Parameters on Tensile Mechanical Behavior in Desktop 3D Printing," *3D Printing and Additive Manufacturing*, vol. 3, no. 3, pp. 183 - 192, 2016.
- [20] R. Jones, "Stratasys Blog: After the Build: Preparing 3D Printed Composite Tools for Use," Stratasys, [Online]. Available: <http://blog.stratasys.com/2017/07/31/post-processing-3d-printed-composite-tooling/>. [Accessed 04 08 2017].

- [21] M.I Molitch-Hou, "Made In Space Begins 3D Printing PEI/PC on the ISS," Engineering.com, 14 07 2017. [Online]. Available: <http://www.engineering.com/3DPrinting/3DPrintingArticles/ArticleID/15254/Made-In-Space-Begins-3D-Printing-PEIPC-on-the-ISS.aspx>.
- [22] S.M. Al-Salem, P. Lettieri, J. Baeyens , "Recycling and recovery routes of plastic solid waste (PSW): A review," *Waste Management*, vol. 29, pp. 2625 - 2643, 2009.
- [23] F. Perugini, M. Mastellone, U. Arena, "A life cycle assessment of mechanical and feedstock recycling options for management of plastic packaging wastes," *Environ. Progr.*, vol. 24, pp. 137 - 154, 2005.
- [24] J. Hopewell, R. Dvorak, E. Kosior, "Plastics recycling: challenges and opportunities.," *Philosophical Transactions of the Royal Society B: Biological Sciences*, vol. 364, no. 1526, pp. 2115 - 2126, 2009.
- [25] F. Cruz, S. Lanza, H. Boudaoud, S. Hoppe, M. Camargo, "Polymer Recycling and Additive Manufacturing in an Open Source context: Optimization of processes and methods," in *2015 Annual International Solid Freeform Fabrication Symposium - An Additive Manufacturing Conference*, Austin, TX, 2015.
- [26] M. Zenkiewicz, J. Richert, P. Rytlewski, K. Moraczewski, M. Stepczyńska, T. Karasiewicz, " Characterisation of multi-extruded poly(lactic acid)," *Polymer Testing*, vol. 28, no. 4, p. 412–418, 2009.
- [27] I. Pillin, N. Montrelay, A. Bourmaud, Y. Grohens, "Effect of thermo-mechanical cycles on the physico-chemical properties of poly(lactic acid)," *Polymer Degradation and Stability*, vol. 93, no. 2, pp. 321 - 328, 2008.
- [28] M.A. Kreiger, M.L. Mulder, A.G. Glover, J.M. Pearce, "Life cycle analysis of distributed recycling of post-consumer high density polyethylene for 3-D printing filament," : , *Journal of Cleaner Production*, no. 70, pp. 90 - 96, 2014.
- [29] C. Baechler, M. DeVuono, J.M. Pearce, "Distributed recycling of waste polymer into RepRap feedstock," *Rapid Prototyping Journal*, vol. 19, no. 2, pp. 118 - 125, 2013.
- [30] H. Hamod, BSc thesis, Suitability of recycled HDPE for 3D printing filament, Helsinki: Arcada University of Applied Science, 2014.

- [31] N. Torres, J.J. Robin, B. Boutevin, "Study of thermal and mechanical properties of virgin and recycled poly(ethylene terephthalate) before and after injection molding," *European Polymer Journal*, vol. 36, pp. 2075 - 2080, 2000.
- [32] E.J. Hunt, C. Zhang, N. Anzalone, J.M. Pearce, "Polymer recycling codes for distributed manufacturing with 3-D printers," *Resources, Conservation and Recycling*, no. 97, pp. 24 - 30, 2015.
- [33] D.L. Bourella, T.J. Watt, D.K. Leigh, B. Fulcher, "Performance limitations in polymer laser sintering," *Physics Procedia*, vol. 56, pp. 147 - 156, 2014.
- [34] U. Ajoku, N. Hopkinson, M. Caine, "Experimental measurement and finite element modelling of the compressive properties of laser sintered Nylon-12," *Materials Science and Engineering A*, vol. 428 , p. 211–216, 2006.
- [35] B. Caulfield, P.E. McHugh, S. Lohfeld, "Dependence of mechanical properties of polyamide components on build parameters in the SLS process," *Journal of Materials Processing Technology*, vol. 182, pp. 477 - 488, 2007.
- [36] S.I. Bakhtiyarov, R.A. Overfelt, "Measurement of liquid metal viscosity by rotational technique," *Acta mater.*, vol. 47, no. 17, pp. 4311 - 4319, 1999.
- [37] M. Fixman, "Polymer Dynamics: Non-Newtonian Intrinsic Viscosity," *The Journal of Chemical Physics*, vol. 45, p. 793, 1966.
- [38] Wikipedia of Commons, "Selective laser sintering - Wikipedia," [Online]. Available: https://en.wikipedia.org/wiki/Selective_laser_sintering. [Accessed 24 10 2017].
- [39] Spencer wright, "3D printing titanium and the bin of broken dreams," [Online]. Available: <http://pencerw.com/feed/2015/3/15/3d-printing-titanium-and-the-bin-of-broken-dreams>. [Accessed 28 10 2017].
- [40] L.P. Grinan, O.J. Ferrando, L.J. Ferrando, A. Uriondo, E.M. Diaz, M. Esperon-Miguez, S. Perinpanayagam, "Additive Manufacturing: Certification in the Aircraft Market and a Qualification Procedure for Metal Parts," in *EASN 2015*, 2015.
- [41] D.M. Bauer, K. Dietrich, M. Walter, P. Forêt, F. Palm, G. Witt, "Effect of Process Gas and Powder Quality on Aluminum Alloys Processed by Laser

- Based Powder Bed Melting Process," in *Solid Freeform Fabrication 2016: Proceedings of the 27th Annual International*, Austin, TX, 2016.
- [42] Finish Standards Association, "SFS-EN 1274 - Thermal spraying – Powders – Composition, technical supply conditions," Finish Standards Association, Helsinki, 2004.
- [43] F. Calignano, D. Manfredi, E.P. Ambrosio, L. Iuliano, P. Fino, "Influence of process parameters on surface roughness of aluminum parts produced by DMLS," *International Journal of Advanced Manufacturing Technology*, vol. 67, pp. 2743 - 2751, 2013.
- [44] M. Bendsoe and O. Sigmund, *Topology Optimization: Theory, Methods and Applications*, Berlin: Springer-Verlag, 2004.
- [45] D. Braess, *Finite Elements: Theory, Fast Solvers, and Applications in Solid Mechanics*, London: Cambridge University Press, 2001.
- [46] N. Aage, E. Andreassen, B.S. Lazarov, O. Sigmund, "Giga-voxel computational morphogenesis for structural design," *Nature*, vol. 550, p. 84–86, 2017.
- [47] S. Osher and R. Fedkiw, *Level Set Methods and Dynamic Implicit Surfaces*, New York: Springer-Verlag, 2003.
- [48] M.Y. Wang, X. Wang, D. Guo, "A level set method for structural topology optimization," *Computer methods in applied mechanics and engineering*, vol. 192, pp. 227 - 246, 2003.
- [49] Z. Zuo, PhD Thesis: *Topology Optimization of Periodic Structures*, Melbourne: RMIT University, 2009.
- [50] O.M. Querin, M. Victoria, C.A. Gordo, R. Ansola, P. Martí, *Topology Design Methods for Structural Optimization*, Chennai: Elsevier, 2017.
- [51] Altair, *Practical Aspects of Structural Optimization: A Study Guide*, second edition, Altair, 2015.
- [52] Z.H. Zuo, Y.M. Xie, "A simple and compact Python code for complex 3D topology optimization," *Advances in Engineering Software*, vol. 85, pp. 11 - 11, 2015.

- [53] Autodesk, "Netfabb: Additive manufacturing and design software," [Online]. Available: <https://www.autodesk.com/products/netfabb/overview>. [Accessed 18 10 2017].
- [54] Geonx, "Virfac: Additive Manufacturing," [Online]. Available: <http://www.geonx.com/index-3.html>. [Accessed 18 10 2017].
- [55] Additive Works, "Amphyon: Simulation and Process Software for Additive Manufacturing," [Online]. Available: <https://additive.works/>. [Accessed 18 10 2017].
- [56] MSC, "Simufact Additive," [Online]. Available: <http://www.mssoftware.com/product/simufact-additive>. [Accessed 18 10 2017].
- [57] Dassault Systems, "Simulia," [Online]. Available: <https://www.3ds.com/products-services/simulia/>. [Accessed 18 10 2017].
- [58] G. Mastinu, "BRAKE DEVELOPMENT METHODS – Topology optimization of a brake caliper and upright of a race car," in *7th International Munich Chassis Symposium*, Munchen, 2016.
- [59] Brembo, "Brembo Calipers," [Online]. Available: <http://www.brembo.com/en/bike/sporting-use/calipers>. [Accessed 18 07 2017].
- [60] K. Domond, Thesis: Brake Rotor Design and Comparison using Finite Element Analysis: An Investigation in Topology Optimization, San Diego: University of California San Diego, 2010.
- [61] J.H. Zhu, W.H. Zhang, L. Xia, "Topology Optimization in Aircraft and Aerospace Structures Design," *Arch Computat Methods Eng*, vol. 23, no. 4, p. 595–622, 2015.
- [62] C.T. Smyth, Functional Design for 3D Printing - Second Edition, Amazon, 2013.
- [63] 3D Hubs, "Design Rules for 3D Printing leaflet," [Online]. Available: www.3dhubs.com. [Accessed 2017 10 20].
- [64] S. Wen, S. Li, Q. Wei, Y. Chunze, S. Zhang, Y. Shi, "Effect of molten pool boundaries on the mechanical properties of selective laser melting parts,"

- Journal of Materials Processing Technology*, vol. 214, p. 2660–2667, 2014.
- [65] S.S. Al-Bermani, M.L. Blackmore, W. Zhang, I. Todd, "The Origin of Microstructural Diversity, Texture and Mechanical Properties in Electron Beam Melted Ti-6Al-4V," *Metallurgical and Material Transactions A*, vol. 41, no. 13, pp. 3422 - 3434, 2010.
- [66] D. Thomas, PhD Thesis: The Development of Design Rules for Selective Laser Melting, Cardiff: University of Wales Institute, 2009.
- [67] E. Atzeni, A. Salmi, "Study on unsupported overhangs of AlSi10Mg parts processed by Direct Metal Laser Sintering (DMLS)," *Journal of Manufacturing Processes*, 2015 In press.
- [68] F. Calignano, "Design optimization of supports for overhanging structures in aluminum and titanium alloys by selective laser melting," *Materials and Design*, vol. 64, p. 203–213, 2014.
- [69] American Society for Testing Materials, "ISO / ASTM52910 - 17 Standard Guidelines for Design for Additive Manufacturing," ASTM International, West Conshohocken, PA, 2017.
- [70] J. Kranz, D. Herzog, C. Emmelmann, "Design guidelines for laser additive manufacturing of lightweight structures in TiAl6V4," *Journal of Laser Applications*, vol. 27, no. 1, pp. 1 - 17, 2015.
- [71] M. Brandt, *Laser Additive Manufacturing: Materials, Design, Technologies, and Applications*, Amsterdam: Elsevier, 2017.
- [72] A.T. Gaynor, N.A. Meisel, C.B. Williams, J.K. Guest, "Topology Optimization for Additive Manufacturing: Considering Maximum Overhang Constraint," in *15th AIAA/ISSMO Multidisciplinary Analysis and Optimization Conference, AIAA AVIATION Forum*, Atlanta, USA, 2014.
- [73] A.T. Gaynor, J.K. Guest, "Topology optimization considering overhang constraints: Eliminating sacrificial support material in additive manufacturing through design," *Structural and Multidisciplinary Optimization*, vol. 54, no. 5, p. 1157–1172, 2016.
- [74] A.M. Mirzendehtdel, K. Suresh, "Support structure constrained topology optimization for additive manufacturing," *Computer-Aided Design*, vol. 81, p. 1–13, 2016.

-
- [75] V.B. Venkayya, "Design of optimum structures," *Computers & Structures*, vol. 1, pp. 265 - 309, 1971.
- [76] A.S.L. Chan, "Design of Michell Optimum Structures," in *CoA Report 142*, Cranfield, College of Aeronautics Cranfield, 1960, pp. 1-52.
- [77] W.S. Hemp, H.S.Y. Chan, "Optimum Structures," in *CoA Reports*, Cranfeld, College of Aeronautics, 1965, pp. 1 - -62.
- [78] O. Sigmund, "A 99 line topology optimization code written in Matlab," *Struct Multidisc Optim*, vol. 21, p. 120–127, 2001.
- [79] V.J. Challis, "A discrete level-set topology optimization code written in Matlab," *Struct Multidisc Optim*, vol. 41, p. 453 – 464, 2010.
- [80] K. Liu, A. Tovar, "An efficient 3D topology optimization code written in Matlab," *Struct Multidisc Optim*, vol. 50, p. 1175–1196, 2014.
- [81] M. Otomori, T. Yamada, K. Izui, S. Nishiwaki, "Matlab code for a level set-based topology optimization method using a reaction diffusion equation," *Struct Multidisc Optim*, vol. 51, p. 1159 – 1172, 2015.
- [82] ASTM International, *ASTM D790-10. Standard test methods for flexural properties of unreinforced and reinforced plastics and electrical insulating materials*, 2010.
- [83] EOS GmbH - Electro Optical Systems, *EOSINT P800 - Technical data*, Munich: EOS GmbH, 2014.
- [84] EOS GmbH - Electro Optical Systems, "Material data sheet: EOS HP3 PEEK," EOS, München, 2015.
- [85] D. L. Goble, E. G. Wolff, "Strain-rate sensitivity index of thermoplastics," *Journal of Material Science*, vol. 28, no. 22, p. 5986–5994, 1993.
- [86] P.J. Rae, E.N. Brown, E.B. Orler, "The mechanical properties of poly(ether-ether-ketone) (PEEK) with emphasis on the large compressive strain response," *Polymer*, vol. 48, pp. 598 - 615, 2007.
- [87] W.Zh. Wu, P. Geng, G. Li, D. Zhao, H. Zhang, J. Zhao, "Influence of Layer Thickness and Raster Angle on the Mechanical Properties of 3D-Printed PEEK and a Comparative Mechanical Study between PEEK and

- ABS," *Materials*, vol. 8, no. 9, pp. 5834-5846, 2015.
- [88] L. Virgin, "On the flexural stiffness of 3D printer thermoplastic," *International Journal of Mechanical Engineering Education*, vol. 45, no. 1, pp. 59 - 75, 2017.
- [89] O. S. Es-Said , J. Foyos , R. Noorani , M. Mendelson , R. Marloth, B. A. Pregger, "Effect of Layer Orientation on Mechanical Properties of Rapid Prototyped Samples," *Materials and Manufacturing Processes*, vol. 15, no. 1, pp. 107-122, 2000.
- [90] C. Ziemian, M. Sharma, S. Ziemian, "Anisotropic Mechanical Properties of ABS Parts Fabricated by Fused Deposition Modelling," in *Mechanical engineering, InTech.*, 2012.
- [91] EOS GmbH - Electro Optical Systems, *EOSINT M270 - Technical data*, Munich: EOS GmbH, 2007.
- [92] EOS GmbH - Electro Optical Systems, "Material data sheet: EOS Aluminium AlSi10Mg," EOS, München, 2015.
- [93] EOS GmbH - Electro Optical Systems, "Material data sheet: EOS Titanium Ti64," EOS, München, 2016.
- [94] F. Calignano, D. Manfredi, E.P. Ambrosio, S. Biamino, M. Pavese, P. Fino, "Direct fabrication of joints based on direct metal laser sintering in aluminum and titanium alloys.," *Procedia CIRP*, vol. 21, pp. 129 - 132, 2014.
- [95] National Institute of Health, "ImageJ - Image processing with Java," [Online]. Available: <https://imagej.nih.gov/ij/>. [Accessed 07 07 2017].
- [96] International Organization for Standardization, *EN-ISO 12181-1:2011: Geometrical product specifications (GPS) - Roundness - Part 1: Vocabulary and parameters of roundness*, Helsinki: Finnish Standards Association, 2011.
- [97] J.M. Rodriguez, J.M.A Johansson, T. Edeskär, "Particle Shape Determination by Two-Dimensional Image Analysis in Geotechnical Engineering," *Danish Geotechnical Society. Proceedings of Nordic Conference on Soil Mechanics and Geotechnical NGM*, vol. 27, pp. 207-218 , 05/2012.

- [98] A. Goeroeg, "Number of Points For Roundness Measurement – Measured Results Comparison," *Research Papers Faculty of Materials Science and Technology Slovak University of Technology*, vol. 19, no. 30, pp. 19-24, 2011.
- [99] A. Gebhardt, *Understanding Additive Manufacturing*, Munich: Hanser Publishers, 2011.
- [100] C. Semini, J. Goldsmith, D. Manfredi, F. Calignano, E.P. Ambrosio, J. Pakkanen, D.G. Caldwell, "Additive Manufacturing for Agile Legged Robots with Hydraulic Actuation," in *International Conference on Advanced Robotics*, Istanbul, 2015.
- [101] D. Manfredi, F. Calignano, E. P. Ambrosio, M. Krishnan, R. Canali, S. Biamino, M. Pavese, E. Atzeni, L. Iuliano, P. Fino, C. Badini, "Direct Metal Laser Sintering: an additive manufacturing technology ready to produce lightweight structural parts for robotic applications," *La Metallurgia Italiana*, vol. 10, pp. 1 - 10, 2013.
- [102] G. Strano, L. Hao, R.M. Everson, K.E. Evans, "Surface roughness analysis, modelling and prediction in selective laser melting," *Journal of Materials Processing Technology*, vol. 213, pp. 589 - 597, 2013.
- [103] T.A. Krol, C. Seidel, M.F. Zaeh, "Prioritization of process parameters for an efficient optimisation of additive manufacturing by means of a finite element method," in *Procedia CIRP 12*, Ischia, 2012.
- [104] L.W. Mays, *Hydraulic Design Handbook*, Milan: McGraw-Hill Education, 1999.
- [105] Vickers Aerospace, "Brosure: Fluid Power, Control and Actuation Products on the Boeing 747-400," Vickers Aerospace, London, 1993.
- [106] L. Thijs, K. Kempen, J.P. Kruth, J.V. Humbeeck, "Fine-structured aluminium products with controllable texture by selective laser melting of pre-alloyed AlSi10Mg powder," *Acta Materialia*, vol. 61, pp. 1809 - 1819, 2013.
- [107] D. Manfredi, F. Calignano, M. Krishnan, R. Canali, E.P. Ambrosio, S. Biamino, D. Ugues, M. Pavese, P. Fino, "Chapter 1: Additive Manufacturing of Al Alloys and Aluminium Matrix Composites (AMC)," in *Light Metal Alloys Applications*, Rijeka, InTech, 2014, pp. 1 - 32.

-
- [108] J. Rodriguez, J. Johansson, T. Edeskär, "Particle shape determination by two-dimensional image analysis in geotechnical engineering," in *Proceedings of Nordic Conference on Soil Mechanics and Geotechnical NGM*, Copenhagen, 2012.
- [109] E. Chiavazzo, L. Ventola, F. Calignano, D. Manfredi, P. Asinari, "A sensor for direct measurement of small convective heat fluxes: Validation and application to micro-structured surfaces," *Experimental Thermal and Fluid Science*, vol. 55, pp. 42 - 53, 2014.
- [110] L. Ventola, F. Robotti, M. Dialameh, F. Calignano, D. Manfredi, E. Chiavazzo, P. Ashinari, "Rough surfaces with enhanced heat transfer for electronics cooling by direct metal laser sintering," *International Journal of Heat and Mass Transfer*, vol. 75, pp. 58 - 74, 2014.
- [111] Istituto Italiano di Tecnologia, "HYQ-Robot," [Online]. Available: <http://www.iit.it/hyq>. [Accessed 28 06 2017].
- [112] C. Semini, PhD thesis: HyQ – design and development of a hydraulically actuated quadruped robot, Genoa: University of Genova, 2010.

Appendix I – Finite Element Analysis

Finite Element Analysis (FEA) starts by calculating individual elemental stiffness matrixes K_e for Equation 3 and from there assembling the global stiffness matrix K for Equation 4 [45]. In linear model Figure 103 is a simple one dimensional truss element between points a and b that has connectivity and material stiffness K_e in the middle corresponding any loads (f) and dislocations (u). The points have a load and a dislocation in one degree of freedom (DOF) assigned to them.

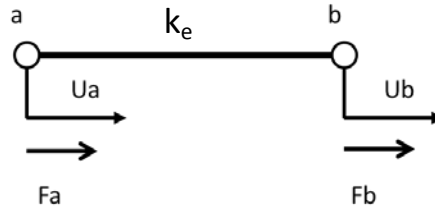


Figure 103. Stiffness matrix element

For the K_e it is possible to write force equilibrium equations:

$$\text{Node a: } k_e u_a - k_e u_b = f_a$$

$$\text{Node b: } -k_e u_a + k_e u_b = f_b$$

Equation 16. Elemental stiffness matrix force equilibrium equations.

Converting this into matrix form gives:

$$\begin{bmatrix} k_e & -k_e \\ -k_e & k_e \end{bmatrix} \begin{bmatrix} u_a \\ u_b \end{bmatrix} = \begin{bmatrix} f_a \\ f_b \end{bmatrix}$$

Equation 17. Elemental stiffness matrix force equilibrium equations in matrix form.

The size of the stiffness matrix depends on the number of DOF. In the case of the single truss element the matrix is 2x2 as it has only 2 DOF. To compile larger global stiffness matrix, elemental stiffness matrixes are joined together depending on their relationships. To create more complex systems the two-node system can be scaled up and how it is done will be shown with 3 node system.

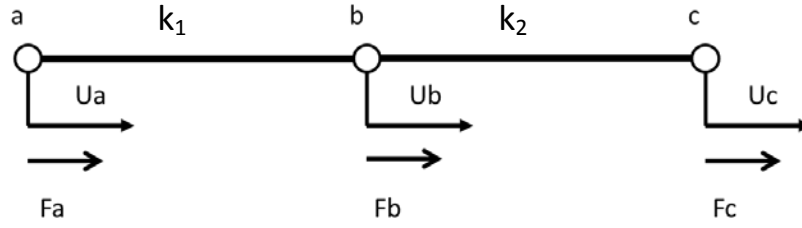


Figure 104. Two stiffness elements

Similarly to a single element, for the two-element system it is possible to write force equilibrium equations:

$$\begin{aligned}\text{Node a: } & k_1 u_a - k_2 u_b = f_a \\ \text{Node b: } & -k_1 u_a + (k_1 + k_2) u_b - k_2 u_c = f_b \\ \text{Node c: } & -k_1 u_b + k_2 u_c = f_c\end{aligned}$$

Equation 18. Global stiffness matrix force equilibrium equations.

That is written in matrix form:

$$\begin{bmatrix} k_1 & -k_1 & 0 \\ -k_1 & k_1 + k_2 & -k_2 \\ 0 & -k_2 & k_2 \end{bmatrix} \begin{bmatrix} u_a \\ u_b \\ u_c \end{bmatrix} = \begin{bmatrix} f_a \\ f_b \\ f_c \end{bmatrix}$$

Equation 19. Elemental stiffness matrix force equilibrium equations in matrix form.

The global stiffness matrix is symmetrical in diagonal axis and consists of the individual stiffness matrixes added together with the corresponding relations, where there is no relationship between the nodes, the k_e stiffness values are zero. For example as node a and node c aren't connected the corresponding value is zero. The global stiffness matrix is symmetric on the diagonal axis. The simplified matrix form of Equation 19 is $KU=F$ as shown in Equation 4.

$$\begin{bmatrix} \boxed{k_1} & \boxed{-k_1} & 0 \\ -k_1 & \boxed{k_1 + k_2} & -k_2 \\ 0 & -k_2 & \boxed{k_2} \end{bmatrix} \begin{bmatrix} u_a \\ u_b \\ u_c \end{bmatrix} = \begin{bmatrix} f_a \\ f_b \\ f_c \end{bmatrix}$$

Equation 20. Elemental stiffness matrix force equilibrium equations showing the conjunction of the matrixes.

Solving displacements U from $KU=F$ is the objective as the global stiffness matrix K can be constructed and force F is given in defining boundary conditions. For solving U it is necessary to make inverse stiffness matrix (K^{-1}) out of K and then it is possible to solve the equation as $U=K^{-1}F$. In order an inverse matrix to be possible the determinate of the matrix K has to be non-singular and not zero. Reversing a matrix can be done for example with the identity matrix and row

operations with Gauss elimination in augmented form. Where k_1 and k_2 are considered scalar values.

$$\begin{aligned}
 & KK^{-1} = I \\
 & \left[\begin{array}{ccc|ccc} k_1 & -k_1 & 0 & 1 & 0 & 0 \\ -k_1 & k_1 + k_2 & -k_2 & 0 & 1 & 0 \\ 0 & -k_2 & k_2 & 0 & 0 & 1 \end{array} \right] \parallel +R_1 \\
 & \left[\begin{array}{ccc|ccc} k_1 & -k_1 & 0 & 1 & 0 & 0 \\ 0 & k_2 & -k_2 & 1 & 1 & 0 \\ 0 & -k_2 & k_2 & 0 & 0 & 1 \end{array} \right] \parallel +R_2 \\
 & \left[\begin{array}{ccc|ccc} k_1 & -k_1 & 0 & 1 & 0 & 0 \\ 0 & k_2 & -k_2 & 1 & 1 & 0 \\ 0 & 0 & 0 & 1 & 1 & 1 \end{array} \right] \parallel :k_1 \\
 & \left[\begin{array}{ccc|ccc} k_1 & -k_1 & 0 & 1 & 0 & 0 \\ 0 & k_2 & -k_2 & 1 & 1 & 0 \\ 0 & 0 & 0 & 1 & 1 & 1 \end{array} \right] \parallel :k_2
 \end{aligned}$$

Reversing the matrix is not possible without applying boundary conditions. Those have to be enforced to make the global stiffness matrix non-singular. Adding boundary condition sets nodal displacement zero and that row can be neglected in calculations as it is a fixed point.

$$\left[\begin{array}{ccc|ccc} k_1 & -k_1 & 0 & 1 & 0 & 0 \\ -k_1 & k_1 + k_2 & -k_2 & 0 & 1 & 0 \\ 0 & -k_2 & k_2 & 0 & 0 & 1 \end{array} \right] \left[\begin{array}{c} u_a \\ u_b \\ u_c \end{array} \right] = \left[\begin{array}{c} f_a \\ f_b \\ f_c \end{array} \right]$$

The problem becomes solvable:

$$\begin{aligned}
 & \left[\begin{array}{cc|cc} k_1 + k_2 & -k_2 & 1 & 0 \\ -k_2 & k_2 & 0 & 1 \end{array} \right] \parallel +R_2 \\
 & \left[\begin{array}{cc|cc} k_1 & 0 & 1 & 1 \\ -k_2 & k_2 & 0 & 1 \end{array} \right] \parallel :k_1 \\
 & \left[\begin{array}{cc|cc} 1 & 0 & 1/k_1 & 1/k_1 \\ -k_2 & k_2 & 0 & 1 \end{array} \right] \parallel :k_2 \\
 & \left[\begin{array}{cc|cc} 1 & 0 & 1/k_1 & 1/k_1 \\ -1 & 1 & 0 & 1/k_2 \end{array} \right] \parallel +R_1 \\
 & \left[\begin{array}{cc|cc} 1 & 0 & 1/k_1 & 1/k_1 \\ 0 & 1 & 1/k_1 & 1/k_2 + 1/k_1 \end{array} \right] \\
 & K^{-1} = \begin{bmatrix} 1/k_1 & 1/k_1 \\ 1/k_1 & 1/k_2 + 1/k_1 \end{bmatrix}
 \end{aligned}$$

To check if the $KK^{-1}=I$, it is possible to solve KK^{-1} :

$$\begin{aligned}
 & \begin{bmatrix} k_1 + k_2 & -k_2 \\ -k_2 & k_2 \end{bmatrix} \begin{bmatrix} 1/k_1 & 1/k_1 \\ 1/k_1 & 1/k_2 + 1/k_1 \end{bmatrix} \\
 = & \begin{bmatrix} \frac{k_1 + k_2}{k_1} + \frac{-k_2}{k_1} & \frac{k_1 + k_2}{k_1} + \frac{-k_2}{k_2} + \frac{-k_2}{k_1} \\ \frac{-k_2}{k_1} + \frac{k_2}{k_1} & \frac{-k_2}{k_1} + \frac{k_2}{k_2} + \frac{k_2}{k_1} \end{bmatrix} \\
 & = \begin{bmatrix} 1 & 0 \\ 0 & 1 \end{bmatrix} = I
 \end{aligned}$$

Appendix II – LSM 3D Code

```

%% 3D TOPOLOGY OPTIMIZATION USING LEVEL-SET METHOD,
% Standing behind the works of giants. The code is based on the previous
% codes written and published.
%
% 2D SIMP 99 code via Bendsoe 2004
% -Struct Multidisc Optim 21, 120-127, 2001
% 2D level set method via VIVIEN J. CHALLIS 2009
% -Struct Multidisc Optim, 41:453-464, 2010
% 2D LSM 88-code via Otomori. 2015
% -Struct Multidisc Optim, 43:1-16, 2011
% 3D SIMP via Liu K. 2011
% -Struct Multidisc Optim, 50:117-1196, 2014
%
% recommed parameters toptopt_LSM_3D(30,30,6,0.3,3,4,4)
%                                     toptopt_LSM_3D(30,30,30,0.3,3,4,4)
%
%%Application 2D to 3D by Pakkanen J. 08.07.2016
% University of California San Diego & Politecnico di Torino
% e-mail: jukka.pakkanen@iki.fi

function [struc] =
topopt_LSM_3D(nelx,nely,nelz,volReq,stepLength,numReinit,topWeight)
% Initialization
struc = ones(nelx,nely,nelz); %Design space initialization
[lsf] = reinit(struc); %Initialise lsf
shapeSens = zeros(nelx,nely,nelz); %Objective function
topSens = zeros(nelx,nely,nelz); %Sensitivity function
maxloop = 200; %Max iteration number
gif_name = 'file_output01.gif'; %Name of output gif
stl_name = 'file_output01.stl'; %Name of output STL

% USER-DEFINED MATERIAL PROPERTIES
E0 = 1; % Young's modulus of solid material
Emin = 1e-9; % Young's modulus of void-like material
nu = 0.3; % Poisson's ratio

% Cantilever beam constrains
% USER-DEFINED LOAD DOFs
[il,jl,kl] = meshgrid(nelx, 0, 0:nelz); % Coordinates
loadnid = kl*(nelx+1)*(nely+1)+il*(nely+1)+(nely+1-jl); % Node IDs
loaddof = 3*loadnid(:) - 1; % DOFs
% USER-DEFINED SUPPORT FIXED DOFs
[iif,jf,kf] = meshgrid(0,0:nely,0:nelz); % Coordinates
fixednid = kf*(nelx+1)*(nely+1)+iif*(nely+1)+(nely+1-jf); % Node IDs
fixeddof = [3*fixednid(:); 3*fixednid(:)-1; 3*fixednid(:)-2]; % DOFs

```



```

% PREPARE FINITE ELEMENT ANALYSIS
nele = nelx*nely*nelz;
ndof = 3*(nelx+1)*(nely+1)*(nelz+1);
F = sparse(load dof,1,-1,ndof,1);
U = zeros(ndof,1);
freedofs = setdiff(1:ndof,fixeddof);
[KE] = lk_H8(nu); % call Stiffness matrix

nodegrd = reshape(1:(nely+1)*(nelx+1),nely+1,nelx+1);
nodeids = reshape(nodegrd(1:end-1,1:end-1),nely*nely,1);
nodeidz = 0:(nely+1)*(nelx+1):(nelz-1)*(nely+1)*(nelx+1);
nodeids = repmat(nodeids,size(nodeidz))+repmat(nodeidz,size(nodeids));
edofVec = 3*nodeids(:)+1;
edofMat = repmat(edofVec,1,24)+ ...
    repmat([0 1 2 3*nely + [3 4 5 0 1 2] -3 -2 -1 ...
        3*(nely+1)*(nelx+1)+[0 1 2 3*nely + [3 4 5 0 1 2] -3 -2 -1]],nele,1);
iK = reshape(kron(edofMat,ones(24,1))',24*24*nele,1);
jK = reshape(kron(edofMat,ones(1,24))',24*24*nele,1);

% Main loop:
for iterNum = 1:maxloop
    % FE-analysis, calculate sensitivities
    sK = reshape(KE(:)*(Emin+struc(:)'+(E0-Emin)),24*24*nele,1);
    K = sparse(iK,jK,sK); K = (K+K')/2;

    %Linear solver
    %U(freedofs,:) = K(freedofs,freedofs)\F(freedofs,:);

    %Iterative solver for U and large problems
    tolit = 1e-8; maxit=8000;
    M = diag(diag(K(freedofs, freedofs)));
    U(freedofs,:)=pcg(K(freedofs, freedofs),F(freedofs,:),tolit,maxit,M);

    %Design update, objective function
    ce = reshape(sum((U(edofMat)*KE).*U(edofMat),2),[nelx,nely,nelz]);
    shapeSens = -(Emin+struc*(E0-Emin)).*ce;
    topSens = (0.0001+struc*(1-0.0001)).*ce;

    % Store data, print & plot information
    objective(iterNum) = -sum(shapeSens(:));
    volCurr = sum(struc(:))/(nelx*nely*nely);
    % output information on the console
    display([' It.: ' num2str(iterNum) ' Compl.: '
        ' Vol.: ' sprintf('%6.5f',volCurr)]);
    create_gif(struc, iterNum, gif_name); %start or call gif creation and save image
    % Check for convergence
    if iterNum > 5 && ( abs(volCurr-volReq) < 0.009 ) && ...
        all( abs(objective(end)-objective(end-5:end-1)) < 0.01*abs(objective(end)) )
        display_3D(struc); %print the result
        convert_STL(struc,stl_name); %create STL-cad file
        return; %terminate program if converge
    end
    % Set augmented Lagrangian parameters
    if iterNum == 1
        la = -0.01; La = 1000; alpha = 0.9;
    else

```

```

    la = la - 1/La * (volCurr - volReq); La = alpha * La;
end
% Include volume sensitivities
shapeSens = shapeSens - la + 1/La*(volCurr-volReq);
topSens = topSens + pi*(la - 1/La*(volCurr-volReq));
% Design update
[struct,lsf] = updateStep(lsf,shapeSens,topSens,stepLength,topWeight);
% Reinitialize level-set function
if ~mod(iterNum,numReinit)
    [lsf] = reinit(struct);
end
end
display_3D(struct);          %Print the results
convert_STL(struct,sti_name); %create STL-file
end

%%---- REINITIALIZATION OF LEVEL-SET FUNCTION ----
function [lsf] = reinit(struct)
structFull = (zeros(size(struct)+2));
structFull(2:end-1,2:end-1,2:end-1) = struct;
% Use "bwdist" (Image Processing Toolbox 2D), bwdistsc for 3D performance
lsf = (~structFull).*(bwdistsc(structFull)-0.5) - structFull.*(bwdistsc(structFull-1)-0.5);
end

%%----- DESIGN UPDATE -----
function [struct,lsf] = updateStep(lsf,shapeSens,topSens,stepLength,topWeight)

% Smooth the sensitivities (convn is n:th dimension function)
[shapeSens] = convn(padarray(shapeSens,[1,1],'replicate'),1/6*[0 1 0; 1 2 1; 0 1 0],'valid');
[topSens] = convn(padarray(topSens,[1,1],'replicate'),1/6*[0 1 0; 1 2 1; 0 1 0],'valid');

%Constrains for LSF to keep load bearing voxels solid
%Load bearing pixels must remain solid - cantilever:
shapeSens(end,end,end) = 0;
topSens(end,end,end) = 0;

% Design update via evolution
[struct,lsf] = evolve(-shapeSens,topSens.*(lsf(2:end-1,2:end-1,2:end-1)<0),lsf,stepLength,topWeight);
end

%%---- EVOLUTION OF LEVEL-SET FUNCTION ----
function [struct,lsf] = evolve(v,g,lsf,stepLength,w)
% Extend sensitivities using a zero border
vFull = zeros(size(v)+2); vFull(2:end-1,2:end-1,2:end-1) = v;
gFull = zeros(size(g)+2); gFull(2:end-1,2:end-1,2:end-1) = g;
% Choose time step for evolution based on CFL value
dt = 0.1/max(abs(v(:)));
% Evolve for total time stepLength * CFL value:
for i = 1:(10*stepLength)
    % Calculate derivatives on the grid
    dpx = circshift(lsf,[0,-1,-1])-lsf;
    dmx = lsf - circshift(lsf,[0,1,1]);

```

```

dpy = circshift(lsf,[-1,0,-1]) - lsf;
dny = lsf - circshift(lsf,[1,0,1]);
dpz = circshift(lsf,[-1,-1,0]) - lsf;
dmz = lsf - circshift(lsf,[1,1,0]);
% Update level set function using an upwind scheme
lsf = lsf - dt * min(vFull,0).* ...

sqrt( min(dmx,0).^2+max(dpx,0).^2+min(dny,0).^2+max(dpy,0).^2+min(dmz,0).^2+max(dpz,0).^2) ...
- dt * max(vFull,0) .*...

sqrt( max(dmx,0).^2+min(dpx,0).^2+max(dny,0).^2+min(dpy,0).^2+min(dmz,0).^2+max(dpz,0).^2)...
- w*dt*gFull;
end
% New structure obtained from lsf
strucFull = (lsf<0); struc = strucFull(2:end-1,2:end-1,2:end-1);
end

%%----- ELEMENT STIFFNESS MATRIX -----
function [KE] = lk_H8(nu)
A = [32 6 -8 6 -6 4 3 -6 -10 3 -3 -3 -4 -8;
-48 0 0 -24 24 0 0 0 12 -12 0 12 12 12];
k = 1/144*A*[1; nu];

K1 = [k(1) k(2) k(2) k(3) k(5) k(5);
k(2) k(1) k(2) k(4) k(6) k(7);
k(2) k(2) k(1) k(4) k(7) k(6);
k(3) k(4) k(4) k(1) k(8) k(8);
k(5) k(6) k(7) k(8) k(1) k(2);
k(5) k(7) k(6) k(8) k(2) k(1)];
K2 = [k(9) k(8) k(12) k(6) k(4) k(7);
k(8) k(9) k(12) k(5) k(3) k(5);
k(10) k(10) k(13) k(7) k(4) k(6);
k(6) k(5) k(11) k(9) k(2) k(10);
k(4) k(3) k(5) k(2) k(9) k(12);
k(11) k(4) k(6) k(12) k(10) k(13)];
K3 = [k(6) k(7) k(4) k(9) k(12) k(8);
k(7) k(6) k(4) k(10) k(13) k(10);
k(5) k(5) k(3) k(8) k(12) k(9);
k(9) k(10) k(2) k(6) k(11) k(5);
k(12) k(13) k(10) k(11) k(6) k(4);
k(2) k(12) k(9) k(4) k(5) k(3)];
K4 = [k(14) k(11) k(11) k(13) k(10) k(10);
k(11) k(14) k(11) k(12) k(9) k(8);
k(11) k(11) k(14) k(12) k(8) k(9);
k(13) k(12) k(12) k(14) k(7) k(7);
k(10) k(9) k(8) k(7) k(14) k(11);
k(10) k(8) k(9) k(7) k(11) k(14)];
K5 = [k(1) k(2) k(8) k(3) k(5) k(4);
k(2) k(1) k(8) k(4) k(6) k(11);
k(8) k(8) k(1) k(5) k(11) k(6);
k(3) k(4) k(5) k(1) k(8) k(2);
k(5) k(6) k(11) k(8) k(1) k(8);
k(4) k(11) k(6) k(2) k(8) k(1)];

```

```

K6 = [k(14) k(11) k(7) k(13) k(10) k(12);
      k(11) k(14) k(7) k(12) k(9) k(2);
      k(7) k(7) k(14) k(10) k(2) k(9);
      k(13) k(12) k(10) k(14) k(7) k(11);
      k(10) k(9) k(2) k(7) k(14) k(7);
      k(12) k(2) k(9) k(11) k(7) k(14)];
KE = 1/((nu+1)*(1-2*nu))*...
    [ K1 K2 K3 K4;
      K2' K5 K6 K3';
      K3' K6 K5' K2';
      K4 K3 K2 K1'];
end

% === DISPLAY 3D TOPOLOGY (ISO-VIEW) ===
function display_3D(rho)

N = ndims(rho); %read dimension from the Design matrix to decide a printer
if N==2
    colormap(gray); imagesc(rho); axis equal; axis tight; axis off; pause(1e-6); %
    plot on screen
    return
else
    [nelx,nely,nelz] = size(rho);
    hx = 1; hy = 1; hz = 1; % User-defined unit element size
    face = [1 2 3 4; 2 6 7 3; 4 3 7 8; 1 5 8 4; 1 2 6 5; 5 6 7 8];
    set(gcf,'Name','ISO display','NumberTitle','off');
    for k = 1:nelz
        z = (k-1)*hz;
        for i = 1:nelx
            x = (i-1)*hx;
            for j = 1:nely
                y = nely*hy - (j-1)*hy;
                if (rho(i,j,k) > 0.6) % User-defined display density threshold
                    vert = [x y z; x y-hx z; x+hx y-hx z; x+hx y z; x y z+hx; x y-hx
                    z+hx; x+hx y-hx z+hx;x+hx y z+hx];
                    vert(:,[2 3]) = vert(:,[3 2]); vert(:,2,:) = -vert(:,2,:);
                    patch('Faces',face,'Vertices',vert,'FaceColor',[0.2+0.8*(1-
                    rho(i,j,k)),0.2+0.8*(1-rho(i,j,k)),0.2+0.8*(1-rho(i,j,k))]);
                    hold on;
                end
            end
        end
    end
    axis equal; axis tight; axis off; box on; view([30,30]); pause(1e-6);
end
end

%% STL Printer Function
function convert_STL(xDesign,stl_name)

N = ndims(xDesign); %read dimension from the xDesign matrix to decide a printer
if N==2 %check 2D, since it doesn't work with cubes
    display('design space has only 2 dimentions and 3D is required');
    return
else

```

```

[nely,nelx,nelz] = size(xDesign); %get info of the size of the matrix
gridX = [1:nelx]; gridY = [1:nely]; gridZ = [1:nelz]; %definition of the axis for
the printer script

%printer needs true zero values to interpitate a hole. This loop seeks a less
%than design penalty factor value and replaces all below the value as zeros
for k = nelz:-1:1 %counts from max values to min values
    for i = nelx:-1:1
        for j = nely:-1:1
            if (xDesign (j,i,k) <= 0.6) %0.6 user defined penalisation factor e.g.
volfrac
                xDesign (j,i,k) = 0; %true zero is needed for stl printer to know a
hole
            end
        end
    end
end
%calling the STL printer function % you might need install stlTool plugins
%to matlab from 3rd party.
[faces,vertices] =
CONVERT_voxels_to_stl(stl_name,xDesign,gridY,gridX,gridZ,'ascii');
display('STL printed');
end
end

%% CREATE GIF function
function create_gif(xMatrix, loop, gif_name)

    %xMatrix is the design space
    %loop is the iteration number
    %gif_name = 'test_gif_0X15.gif'; %gives a name for the gif
    N = ndims(xMatrix); %read dimension from the xDesign matrix to deside a printer

    if N == 2 %2D
        minusX = imcomplement(xMatrix); %makes x inverse colours
        B = im2uint8(minusX); % converts the grayscale picture to UINT8 format
        colormap(gray); imagesc(minusX); axis equal; axis tight; axis off;pause(1e-
6); % plot on screen

    else % 3D
        display_3D(xMatrix); %printing the figure
    end

    frame = getframe(1); %capture the figure
    im = frame2im(frame);
    [B,map1] = rgb2ind(im,256);

    if loop == 1; %initialize gif
        imwrite(B,map1, gif_name, 'gif', 'LoopCount',inf,'DelayTime',1); %first
frame
        clf;
        %mkdir('GIF_folder'); %create gif folder in the file
    else %add 1 picture to the gif
        imwrite(B,map1,gif_name, 'gif','WriteMode','append','DelayTime',1); %+1
frame
        clf;

```

```

end
end

%%---- DISCLAIMER -----%
% This code is provided "as is", without any warranty of any kind. %
% Furthermore, the author shall not be held liable in any event caused by %
% the use of the program. %
%-----%

-----
This is a readme file for LSM3D applied by Pakkanen J. in 8.7.2016
at UCSD.
-----

The code is adaptation from 2009 LS-code written by Vivian. The code
currently has boundary constrains and loads that create a cantilever
beam. The original code has been extended from 2D presentation to 3D
problem. NOTE, Please use 3 dimensional input as Matlab interpolates
2x2x1 matrix automatically as 2D 2x2 matrix.

These reference codes are used in making of the 3D code:
2D SIMP 99 code via Bendsoe 2004
-Struct Multidisc Optim 21, 120-127, 2001
2D level set method via VIVIEN J. CHALLIS 2009
-Struct Multidisc Optim, 41:453-464, 2010
3D SIMP via Liu K. 2011
-Struct Multidisc Optim, 43:1-16, 2011
2D LSM 88-code via Otomori. 2015
-Struct Multidisc Optim, 50:1175-1196, 2014

The reference codes and literature references are given in the folder
Literature and_ref_codes. For detailed description of the code in
original 2D configuration, please refer to "2D LSM via Vivien J. Challis"
2009.
-----

Recommnd parameters: toptopt_LSM_3D(nelx,nely,volReq, stepLength,numReinit
topWeight)

topopt_LSM_3D(15,15,15,0.3,3,4,4) %Example 1
topopt_LSM_3D(30,30,6,0.3,3,4,4) %Example 2

Iterative solver for U will be more faster in higher meshes than direct
solver. For example, meshes containing more than 15x15x15 will be faster
with iterative solver than in direct solver.

Input parameter description:
nelx      = element number in x-direction
nely      = element number in y-direction
nelz      = element number in z-direction
volReq    = volume constraint
stepLength= Level set function update constraint relative to CFL
            time step.
numReinit = How often LSF is reinitialised to a signed distance function
topWeight = Parameter to enhance hole creation in evolve function when
            updating LSF.

```

Known issues: Axis are in wrong order.

Files needed for running the LSM:

1.topopt_LSM_3D.m	%Main executable program
2.bwdistsc.m	%n-dimension image processing tool
	%by Y. Mishchenko

Optional extensions to get STL-printer working:

3.CONVERT_meshformat.m	%For STL-printer (CAD output) by A. Aitkenhead
4.CONVERT_voxels_to_stl.m	%For STL-printer (CAD output) by A. Aitkenhead
5.WRITE_stl.m	%For STL-printer (CAD output) by A. Aitkenhead

2-5 are standard libraries written in Matlab, what can be downloaded
from the Mathworks community file-exchange from the corresponding authors.

Application 2D to 3D by Pakkanen J. 08.07.2016

University of California San Diego & Politecnico di Torino

e-mail: jukka.pakkanen@iki.fi
